WARWICK
THE UNIVERSITY OF WARWICK

**A Thesis Submitted for the Degree of PhD at the University of Warwick**

**Permanent WRAP URL:**

**http://wrap.warwick.ac.uk/184813**

**Copyright and reuse:**
This thesis is made available online and is protected by original copyright.
Please scroll down to view the document itself.
Please refer to the repository record for this item for information to help you to cite it.
Our policy information is available from the repository home page.

For more information, please contact the WRAP Team at: wrap@warwick.ac.uk

**warwick.ac.uk/lib-publications**

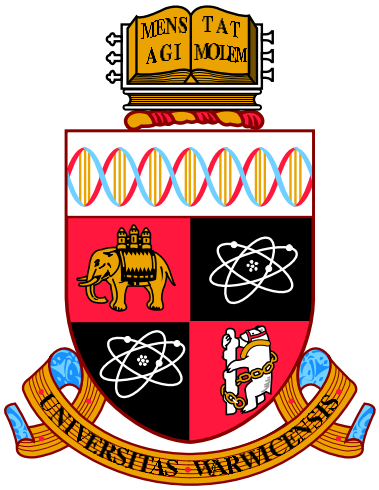


# Antimonide thin films: topological and thermoelectric properties

by

**Ibrahim Gamal Amin Mohamed Elhoussieny**

**Thesis**

Submitted to the University of Warwick

for the degree of

**Doctor of Philosophy in Physics**

**Department of Physics**

March 2023

THE UNIVERSITY OF WARWICK

# Contents

# List of Tables

# List of Figures

# Acknowledgments

I express deep gratitude to my supervisor (Dr Gavin Bell) for the great support I received throughout the whole duration of my PhD. Dr Gavin contributed to planning for the research project and provided me with the essential training to use our lab equipment. In addition, He gave me both technical support in performing different experiments and scientific support in the data analysis and interpreting the results. Moreover, I enjoyed his advice during the thesis writing period which improved my academic writing style. This thesis would not be in that form without his generous support.

The equipment used in this thesis was built and maintained by former and current "Surface Science" lab members. In chapter 3, the author describes his contribution to developing the vacuum systems used. Building the new system (Morbius) required contributions from fellow members: Dr Gavin Bell, Tom Rehaag, Christopher Benjamin and Aleksei Boldin; the technical team includes Dr Alan Burton and physics mechanical and electronic workshop members. In addition, Tom Rehaag cooperated during the growth of the Sb films series (Chapter 6). I also acknowledge Tom's technical support in setting up the flexibility experiment and troubleshooting LabView errors (Chapter 3), and the useful scientific discussion on different measurements and data analysis. The calibration of the gold tip of the Kelvin probe using an HOPG sample was done by two students from our group, Adam Sandy-Kyari and Freya Slaney-Parker. I also thank Dr Atif Rasheed for supporting the deposition of BiSb films (MP50-MP55) in Mantis chamber and giving me the appropriate training.

I am very grateful to the Egyptian Higher Education Ministry and the Egyptian Cultural and Educational Bureau in London for supporting my PhD full scholarship

(Ref: MM5/18). I also acknowledge the support I received from Ain Shams University in Cairo, Egypt, regarding my scholarship.

I acknowledge the support I received from the University of Warwick staff, including the induction training and following support to use the instruments and, sometimes, understand the experimental results. This includes Dr Marc Walker from the XPS facility; Stephen York and Steven Hindmarsh from research technology platform (RTP) microscopy; Dr David Walker from the XRD facility; Dr Jack Woolley and Dr Michael Staniforth from Warwick centre for ultrafast spectroscopy (WCUS).

The BiSb device lithography (Chapter 4) was done in the physics clean room in Warwick using the Agile micro-fabrication facility. I am grateful for the technical support I received from the team and the training from the former PhD student, Daniela Dogaru.

# Declarations

This thesis is submitted to the University of Warwick in support of my application for the degree of Doctor of Philosophy in Physics. This research was done under the supervision of Dr Gavin Bell from 2018 to 2023. It has been composed by myself and has not been submitted in any previous application for any degree. The work presented (including data generated and data analysis) was carried out by the author except in the cases outlined below:

**List of data provided and/or analysis carried out by collaborators:**

- The thermoelectric measurements of BiSb thin films, including the temperature-dependent conductivity, as mentioned in Chapter 4 (series MP50:55), were measured by the members of the Energy Science Nanotechnology and Imagination (E-Snail) Lab in the University of Virginia (USA) which is led by Dr Mona Zebarjadi. The measurements were performed by two lab members: Farjana Ferdous Tonni and Md Golam Rosul. I express my gratitude to all the lab members for their cooperation and scientific discussion. Farjana also provided the measurements details and plotted Figure 2.8 (b). The XRD data for samples MP50 and MP54 (Chapter 4) was acquired by Shuai Li from the same university.

- The thermoelectric measurements of ZnSb films grown on Kapton, as mentioned in Chapter 5 (series IZS53:58), was done by our collaborators in the Department of Materials, the University of Manchester (UK). The measurement was taken by Yu Liu and Dr Feridoon Azough, under the supervision of Professor Robert Freer.

- Dr Gavin performed an experiment to measure the conductivity of the ZnSb thin

films grown on Kapton samples after being twisted manually for different cycles (Chapter 5).

**List of non-original figure that was used in the thesis:**

- Figure 1.1 (The band structure illustration) is adapted without permission from reference [3]. The SVG file is made available under the Creative Commons CC0 1.0 Universal Public Domain Dedication (i.e. No copyrights); it could be used, modified and distributed without asking for permission.

- Figure 1.3 (surface band states) is reproduced with permission from Springer Nature [7] (Marius Grundmann, The Physics of Semiconductors book, Third Edition, Chapter 11 (surfaces), page number 396, 2016, Graduate Texts in Physics series, Springer Nature).

- Figure 1.7 (the Zone model illustration) is reprinted from [59] Thin Solid Films, Volume 317, Issues 1–2, P.B Barna, M Adamik, Fundamental structure forming phenomena of polycrystalline films and the structure zone models, Pages 27-33, Copyright (1998), with permission from Elsevier.

- Figure 2.4(i) (The AFM illustration in chapter 2) is printed with permission from article [75]: High-speed atomic force microscopy for materials science, Pyton et. al., International Materials Reviews, and ©Pyton copyright # [2016], reprinted by permission of Informa UK Limited, trading as Taylor & Taylor & Francis Group, http://www.tandfonline.com.

- Figure 2.9 (Thermoelectric measurements configuration by ZEM-3 system) is taken from the manual of Ulvac ZEM-3 system without a permission.

- Figure 3.3 (Morbius chamber's design) was modified from the manufacture data sheet without permission.

- Figure 6.8, (Sb band structure) in Chapter 6, is reprinted with permission from [4] [ Yi Liu and Roland E. Allen, Physical Review B, 52 (3), 1566, 1995] Copyright (1995) by the American Physical Society, DOI: https://doi.org/10.1103/PhysRevB.52.1566.

- Figure 2.9 (Thermoelectric measurements configuration by ZEM-3 system) is extracted from the manual without permission.

**Publications expected from the presented work to peer-review journals or conferences:**

- Elhoussieny, I.G., Rehaag, T.J. and Bell, G.R., 2023. Bulk and surface electrical properties of BiSb on flat and ion beam nano-patterned InP substrates. physica status solidi (b). (Accepted article)
- Elhoussieny, I.G., Rehaag, T.J. and Bell, G.R., 2023. ZnSb films on flexible substrates: stability, optical band gap, electrical properties and indium doping. Adv. Electron. Mater. (Accepted article)
- Thermoelectric properties of topological insulator BiSb thin films grown on flat and patterned InP substrates. (to be submitted)
- Thermoelectric properties of undoped and In-doped ZnSb films on flexible Kapton substrates. (to be submitted)
- Epitaxial Sb film on (InAs) substrate and textured Sb film on glass: structure, electrical and optical properties and work function. (to be submitted)

# Abstract

Antimony and antimony-based thin films attract great attention as topological and thermoelectric materials. In this study, Sb, BiSb and ZnSb thin films were deposited by different physical vapour deposition techniques on various substrates in high and ultra-high vacuums. The structure, composition and topography of the films were investigated using various microscopy and diffraction techniques. The optical and electrical properties of the films were measured using several complementary methods.

The effects of increasing the surface area of thin films of the topological insulator BiSb were studied. To achieve this, BiSb thin films were deposited on both normal flat InP single crystal substrates and nano-patterned ones prepared by ion bombardment. The crystalline texture of the BiSb films was different on flat versus nano-patterned substrates. The electrical conductivity was smaller on nano-patterned substrates, but the contribution of the surface conduction was larger.

Both undoped and In-doped ZnSb thin films were studied for potential application in flexible thermoelectric devices. Films were deposited on rigid glass substrates and flexible polyimide (Kapton) films. The electrical and optical properties of both types were similar. In addition, flexible films showed stability in both electrical and optical measurements before and after 10,000 cycles of bending.

Thermoelectric measurements of BiSb and ZnSb were performed by collaborators and showed promising power factors.

Finally, pure Sb films were grown on both InAs and glass substrates. The films on InAs were single crystal and epitaxial, while on glass a strong (003) texture was evident. On InAs, Sb films were affected by In segregation upon annealing (affecting the work function), while films on glass were stable. The direct band gap of the semimetallic films on glass was determined optically to be 228 meV. This value agrees with published tight-binding band structure calculations.

# Abbreviations

| | |
|---|---|
| 2D | Two dimensional |
| 3D | Three dimensional |
| AFM | Atomic force microscope |
| BFG | Beam flux gauge |
| CF | Conflat flange |
| CPD | Contact potential difference |
| DI | Deionized |
| DLaTGS | Deuterated L-alanine Doped Triglycine Sulfate |
| EDX | Energy dispersive X-ray |
| FEC | Fast entry chamber |
| FEG-SEM | Field emission gun scanning electron microscope |
| FFT | Fast Fourier transform |
| FTIR | Fourier transform infrared |
| FWHM | Full width at half maximum |
| GGA | Generalized gradient approximation |
| GIXRD | Grazing incidence X-ray diffraction |

| | |
|---|---|
| HOPG | Highly ordered pyrolytic graphite |
| HV | High vacuum |
| IPA | Isopropyl alcohol |
| IPES | Inverse-photoemission spectroscopy |
| KF | Klein flange |
| KP | Kelvin probe |
| LCAO | Linear combination of atomic orbitals |
| LPE | Lone pair electron |
| LP-PVD | Low pressure physical vapour deposition |
| MBE | Molecular beam epitaxy |
| MBJ | Modified Becke Johnson |
| NIR | Near infrared |
| PDF | Powder Diffraction File |
| PES | Photoemission spectroscopy |
| PF | Power factor |
| PGEC | Phonon glass and electron crystal |
| PVD | Physical vapour deposition |
| RGA | Residual gas analyser |
| RHEED | Reflection high energy electron diffraction |
| RMS | Root mean square |
| SEM | Scanning electron microscope |

| | |
|---|---|
| SR | Surface ratio |
| SSC | Surface science chamber |
| STM | Scanning tunnelling microscope |
| TC | Texture coefficient |
| TE | Thermoelectric |
| TI | Topological insulator |
| UHV | Ultra-high vacuum |
| UPS | Ultraviolet photoelectron spectroscopy |
| WH | Williamson-Hall |
| XPS | X-ray photoelectron spectroscopy |
| XRD | X-ray diffraction |

# Chapter 1

# Introduction

In this chapter, the basics and principles of the thesis topic are introduced. The chapter starts with discussing the electronic band structure of solids, with a mention of some factors affecting it such as impurities and dimensionality. Surface band states is mentioned to be different in topological insulators than in normal gapped materials. The exotic surface states in topological insulators make them appealing for thermoelectric applications. Thermoelectricity is then introduced in terms of parameters and their relations. To discuss the origin of thermoelectricity and its theory, the Landauer approach is explained to understand electron and phonon transport and derive expressions for their parameters. Afterwards, a brief summary is given about some techniques mentioned in the literature to optimise the thermoelectric parameters. Thin film applications are then introduced because of their convenience with thermoelectric devices. The growth mechanism is discussed, emphasising the role of growth conditions on the quality (order) of the film. Factors such as growth rate, substrate temperature and type, contaminations and additives are discussed as their impact on the growth mode. The crystalline order of films affects both phonons and electronic band structure, with consequences for thermoelectric performance. Finally, the thesis organisation is outlined.

## 1.1 Electronic band structure

All materials consist of atoms or molecules that are bound together with atomic bonds (e.g. ionic and covalent bonds). Each atom consists of a positive nucleus and negative electrons that are constrained to distinct energy levels when they are in free space [1]. When these atoms are brought together to form an ordered solid bulk (crystalline) material, the energy levels convert into bands of energy. These bands are formed from

different individual atomic orbitals; for N atoms, N orbitals overlap. This is called a linear combination of atomic orbitals (LCAO) or tight binding approximation [2]. Figure 1.1 illustrates the energy band formation of hypothetical carbon atoms [3]. The outer-most atomic s and p levels of N atoms hybridise and overlap when the interatomic distance between them becomes smaller. This form the energy bands from their constituent atomic levels which have tiny spacing. The gap between the conduction band minimum and valence band maximum is called the energy gap (i.e. band gap), denoted by $E_g$.

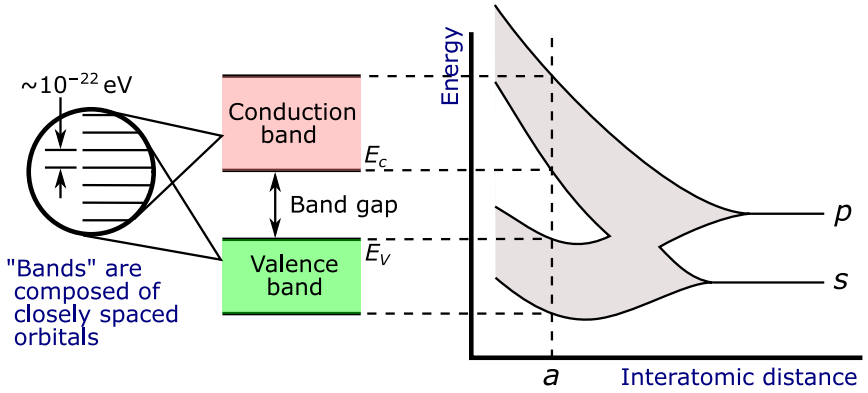


Figure 1.1: Demonstration of the origin of the bands in the condensed materials from the individual atomic levels (LCAO). The bands originated from the overlap of s and p levels of atoms (e.g. carbon) brought together to relax at an interatomic distance (a). The image is adapted from reference [3] without permission.

The shape of the band structure differs from one system to another based on various parameters (e.g. constituting elements and crystal structure). Studying the band structure is very important for researchers to understand the properties of the material, as many important physical properties rely on the band structure. For example, the material's ability to conduct electricity is used to classify materials, based on their band structure, especially the valence and conduction bands, $E_g$ and the position of the Fermi level ($E_f$). Figure 1.2 illustrates the band structure of crystalline materials: metal (a), semi-metal (b), semiconductor (c) and insulator (d). In metals, the Fermi level is placed within the "partially-filled" band, meaning that valence electrons can conduct electricity in the presence of an electric field. If the valence band is filled and separated from the conduction band by an energy gap where Fermi level is placed, electrons in the valence band will need enough energy to cross the gap, as in semiconductors. They act as insulators at absolute temperature but conduct when they are given enough energy ($\geq E_g$), which could be in the form of heat or light. Semimetals lie between metals and semicon-

ductors, where there is a very small overlap between the two bands. For example, Bi and Sb were found to have a negative indirect band gap of 40 meV and 180 meV respectively, when they were calculated using the tight-binding model [4]. The term negative band gap means that the valence band maximum energy is higher than the conduction band minimum. This appears in the carrier concentration of each category. Typically, metals have the highest carrier concentration value ($> 10^{22}$ cm$^{-3}$), while semimetals have smaller values than metals (from $10^{17}$ to $10^{22}$ cm$^{-3}$), but higher than typical undoped semiconductors ($< 10^{17}$ cm$^{-3}$) [2]. With doping, these values can increase by different orders of magnitude. If the band gap is very wide that electrons in the valence band could not be excited to the conduction band, the material is considered an insulator.

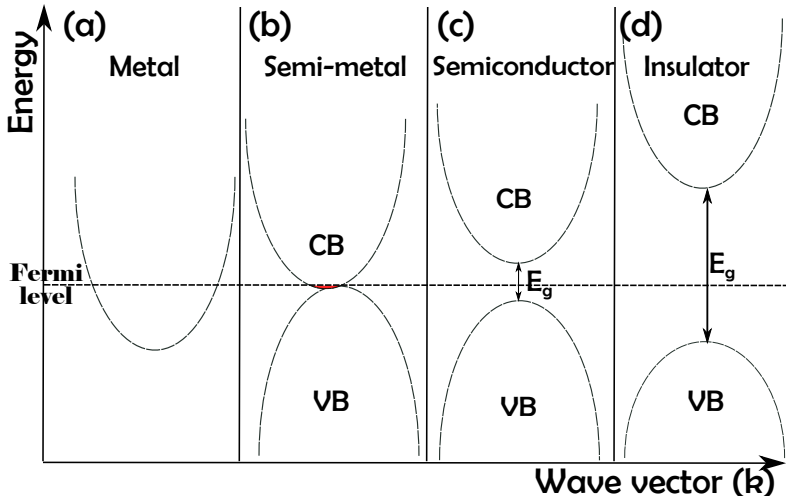


Figure 1.2: Schematic representation of the electronic bands in metals (a), semi-metals (b), semiconductors (c) and insulators (d).

Many factors control the band structure, especially in semiconductors, such as doping, dimensions and disorder. By doping, different energy states from the additive material could appear in the band gap of the host material [2]. Similarly, the presence of some defects (or disorders) in the material's crystal creates some gap states (e.g. tail states). This type of states is called localised states, different from the extended states in the valence and conduction bands; the electronic transition is limited in these states. The electrical and optical contributions from these localised gap states become dominant when the semiconductor gains energy less than the energy gap, but enough to activate their electrons [5, 6]. In addition, limiting the dimensions of the material (i.e. nanostructuring) can influence the shape of the band structure considerably. The band gap increases continuously with decreasing the size of the nanomaterial (e.g. radius of a

quantum dot), making them appealing for new applications [2].

In addition to the bulk band structure mentioned earlier, there is a separate surface band structure that could be significant in some cases. To clarify, the crystalline material has a periodic structure, where all atoms inside have the same surrounding. At the surface, this periodicity ends suddenly, leaving the atoms crystallographically oriented in one direction with dangling bonds, surface reconstruction (surface atoms become ordered in a new structure) may be present. Consequently, the electron wave function changes at the surface forming a band structure that could be different. The surface band states are also localised to the surface and decaying outside, and are mostly located in the bulk band gap [7]. The impact of the band states on the electrical properties differs from one material to another. For example, it becomes more dominating in thin films as it has a larger surface-to-bulk ratio. Materials with non-trivial topology of the band structure may have surface or interface states which are "protected", i.e. must always exist even in the presence of disorder or contamination on the surface [8].

## 1.2 Topological insulators

Topological insulators (TI) is a new class of materials that attracts much attention from the material science community since it was first observed experimentally in BiSb alloys [8–15]. This interest arises from the exotic properties that TI have, related to its electronic boundary states. Basically, if an electron moves in 2D under a very strong magnetic field, it experiences a force perpendicular to its direction of motion. That results in a confined circular motion that makes that sheet material insulator except for edges, where electrons cannot complete this circular motion. This different magnetically-induced topological order was discovered in the 1980s, known as the quantum Hall effect [10, 15]. Similarly, topological insulators have an insulating interior (sheet in 2D and bulk in 3D) and conducting boundaries (edge in 2D and surface in 3D), but without applying an external magnetic field. In TI, the role of the magnetic field is assumed to be replaced by the strong spin-orbit coupling that the material has; this usually occurs with heavy elements with narrow band gaps [10]. The band structure of a 3D TI is distinguished from normal materials, as demonstrated in Figure 1.3, from [7]. In the normal insulator (or semiconductor) shown in panel (a), the surface states are usually located in the bulk gap and not spin-polarised (electrons with spins up and down can populate). While, in TI, the surface states are spin polarised and cross the bulk gap at the so-called Dirac points or cones [7, 10]. In contrast to normal insulators, electrons in the topologically-protected surface states of TI do not face backscattering from defects

and non-magnetic impurities because of its spin-momentum locking [8]; this means that the electron has to change its spin to move in the opposite direction [15]. This allows doping the topological insulator material with the desired non-magnetic additives (e.g. to reduce the bulk's thermal conductivity) without affecting its surface conduction; this is favoured for some applications such as thermoelectric materials. In fact, most of the topological insulators are good thermoelectric materials, likely because of the low thermal conductivity attributed to their heavy elements, and the high electric conductivity of their narrow band gap [15].

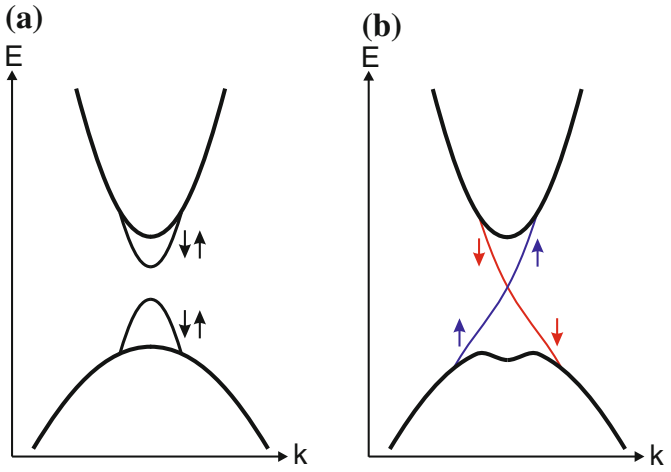


Figure 1.3: Schematic of the surface states location inside the band structure of a normal semiconductor or insulator material (a) and a topological insulator (b). The arrows refer to the spin direction of the occupying electrons. This figure is reproduced with permission from Springer Nature, reference [7].

Low-dimensionality is an approach that TI TE materials, particularly, benefit from; as it suppresses the undesired phonon conductivity to achieve phonon glass and electron crystal (PGEC) material [12, 16, 17]. But the surface states from both sides of very thin nanostructured films can overlap in real space and could form what is called a hybridisation gap in the surface states, which tremendously affects the thermoelectric properties [8].

## 1.3 Thermoelectricity

Thermoelectric (TE) materials can convert heat into electricity, without needing any intermediate heat engines. A TE module could be used to generate electricity from a temperature difference, working as a TE generator. It could be also used to cool

local hot areas (i.e. micro-refrigerators) when supplied by electrical current (Figure 1.4). The simplest form of the thermoelectric device is the thermocouple, in which two different metals are in contact; it produces a thermoelectric voltage which determines the temperature of a body [18]. The efficiency of a thermoelectric device depends on some material parameters such as the Seebeck coefficient ($S$), electrical conductivity ($\sigma$) and thermal conductivity ($k$). Seebeck coefficient is defined as the ratio of the generated thermal Seebeck voltage ($V$) to the temperature difference ($\triangle T$) applied between its ls, $S = V/\triangle T$ [18]. For a conductor of length ($l$) and cross-sectional area ($A$), when a voltage ($V$) is applied, the electrical current ($I$) is:

$$I = \frac{\sigma A V}{l}.$$

Similarly, when a steady temperature difference ($\triangle T$) is applied, heat with the rate ($Q$) flows across this conductor, depending on its thermal conductivity ($k$).

$$Q = -\frac{kA \triangle T}{l}.$$

In Figure 1.4, the TE generator (panel (a)) generates electricity when one side is consistently hotter than the other. In the n-leg, electrons migrate from the hot side to the cold side; the contrast occurs with the p-leg, which creates a potential difference between both sides. On the other hand, the refrigerator cools one side when inserting d.c. current in the module as shown in panel (b). The potential difference forces the electrons to move from the p-leg (i.e. lower Fermi level) to the n-leg (i.e. higher Fermi level) by absorbing the surrounding heat (i.e. refrigeration). The efficiency of a TE module is enhanced by optimising the module design and the material's TE performance (i.e. thermoelectric figure of merit and power factor) [19].

### 1.3.1 Thermoelectric figure of merit and power factor

Optimising the power factor and the thermoelectric figure of merit for thermoelectric materials attracts great attention among material scientists. The thermoelectric figure of merit ( $ZT$ ) is used to qualify the thermoelectric material's performance [20, 21]; good TE materials have high $ZT$.

$$ZT = \frac{S^2 \sigma T}{k}$$

To optimise the value of $ZT$, the power factor ($S^2\sigma$) needs to increase and $k$

needs to decrease. But this is challenging to control as the values of $S$, $\sigma$ and $k$ are correlated. For example, the total thermal conductivity consists of the electronic thermal conductivity ($k_e$) and the lattice thermal conductivity ($k_L$), that $k = k_e + k_L$; $k_e$ is proportional to $\sigma$, that $k_e = L\sigma T$, where $L$ is Lorentz number (this is called Wiedemann–Franz–Lorenz law) [22]. Moreover, $S$, $\sigma$ and $k$ depend on the materials system they share and its band structure. For example, $\sigma$ depends on the temperature and the thermal band gap ($E_g$), as does the maximum Seebeck coefficient $S_{max}$ at temperature $T_{max}$ (e.g. $S_{max} = E_g/2eT_{max}$) [23].

Besides $ZT$, the PF is used frequently to select the suitable TE materials, as there are many challenges in determining the thermal conductivity of the thin films, for example, the substrate contribution to the thermal conduction [24, 25]. The PF is roughly proportional to the TE device's maximum power [26]. In addition, its constituents (i.e. $\sigma$ and $S$) depend on the carrier concentration ($n$), that $k_L$ does not depend on. In general, if $n$ increases, $\sigma$ increases ($\sigma = \mu ne$) where $\mu$ is the carrier mobility; also the Fermi level becomes higher, which reduces $S$ (kinetically, defined as the difference between the average mobile carriers' energy and Fermi level) [27]. Therefore, there is a carrier concentration that gives maximum PF near that of the maximum $ZT$ [18].

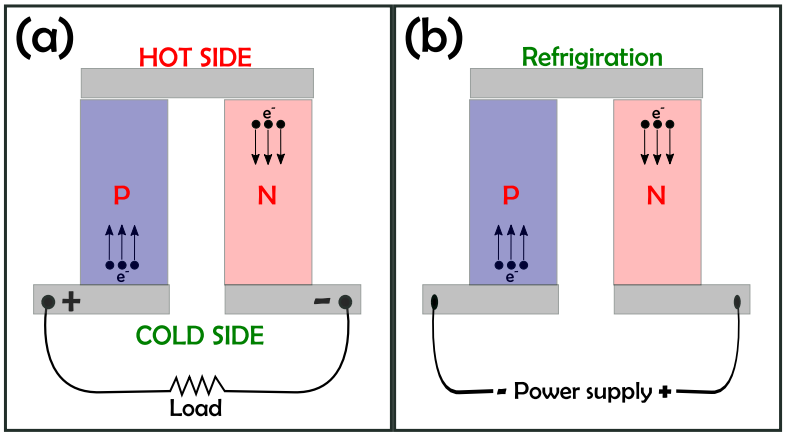


Figure 1.4: Thermoelectric devices, (a) thermoelectric generator; (b) Peltier cooler. The arrows show the electrons' migration directions; in panel (a), from the hot side to the cold in the n-type leg and vice versa for the p-type, producing a potential difference. In panel (b), the external bias forces the electrons to move from the negative to the positive side, which requires absorbing heat from the upper side (i.e. refrigeration).

### 1.3.2 Landauer approach

In the TE materials, electrons (as fermions) transport both heat and charge, and are governed by Fermi-Dirac statistics, while phonons (quantised lattice vibrations) are bosons that transport heat only, and are governed by Bose-Einstein statistics. Landauer transport theory was developed and extended to understand electron and phonon transport in bulk and nanomaterials [26, 28–30]. This unified theory is believed to be an intuitive, simple and accurate approach to understand the thermoelectric parameters, as it deals with both electric and heat transports using the same language [26, 29]. Here, the concept is summarised after Datta and Lundstorm's development of the theory [26, 29, 30]. If an electron moves in a conductor from a source point to a drain, it may travel in a ballistic (like a bullet) or a diffusive (random) manner, or somewhere in between. This depends on the ratio between the length of the conductor ($l$) and the mean free path ($\lambda$) [30].

Assume an electron moves in a ballistic channel with one barrier (e.g. defect) in the middle under a potential difference between the two terminal contacts. The electrochemical potential $\mu$ (i.e. different from $E_F$, Fermi level at 0K. Note: $\mu$ is the mobility elsewhere) will change in this resistor as shown in Figure 1.5(a). The negatively biased terminal has more electrons (higher $\mu$) than the positive side, which derives electrons to move from a highly occupied terminal to the less occupied one. The drop in $\mu$ occurs at terminals because of the change in electronic statistics before and after the interface (like a traffic jam), this is considered to be the source of the heat dissipation [30]. Conductors in real life are longer and wider (have many channels ($M$)), which could be represented as a mixture of parallel and series horizontal and vertical resistors (as illustrated in Figure 1.5 (b)), and Landauer approach is still applicable [30].

The electric current ($I_e$) arises from the difference in electron occupation statistics (i.e. Fermi-Dirac distribution,$f(E)$) between the terminals due to variations in their voltage or temperature [26, 29, 31].

$$I_e = -\frac{2q}{h} \int T(E)\, M(E)\ \triangle f \, \mathrm{d}E$$

$$f(E) = \frac{1}{\exp(\frac{E-\mu}{K_B T} + 1)}$$

where $\triangle f$ is the difference in electron occupation between the terminals, $q$ is the electronic charge, $h$ is Plank's constant and $K_B$ is Boltzmann constant. T(E) is the transmission coefficient that determines how ballistic or diffusive is the current (i.e. probability

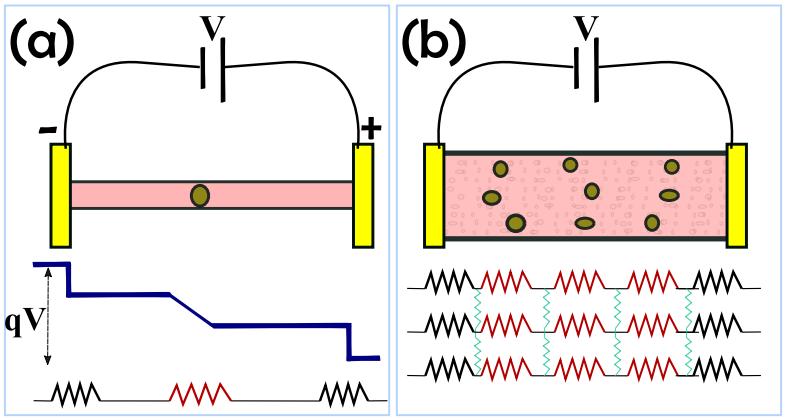


Figure 1.5: Schematic of the potential drop across a single ballistic (elastic) channel with a barrier in the middle (a), and a more complex diffusive (inelastic) resistor's equivalent (b); inspired by reference [30].

that the electron passes the conductor); its value varies from 0 (diffusive) to 1 (ballistic), could be represented as [29, 32]:

$$T(E) = \frac{\lambda(E)}{\lambda(E) + l}$$

$M(E)$ is the number of channels (modes), depending on the density of states and transport-projected velocity.

### Charge transport by electrons

In the case of 3D bulk systems, $\triangle f$ will be converted to the gradient $\bigtriangledown f$, the current density $J$ will replace $I$, and the product of $T(E)$and $M(E)$ could be replaced by the transport function $G(E)$ [26].

$$J = -q \int G(E) \ \bigtriangledown \ f \mathrm{d}E \tag{1.1}$$

This equation could be used with electrons conducting charges ($q$), or heat ($E-\mu$) per particle. The motive for the electronic transport (e.g. $\bigtriangledown T$ and/or $\bigtriangledown V$) is what creates the carriers' statistical imbalance between the terminal. To obtain the electrical parameters $\sigma$, $S$ and $k$, an Ohm-like equation is used in each case. For example, using equation 1.1 after applying a voltage gradient only and Ohm's law (i.e. $J = -\sigma \bigtriangledown V$)

gives the formula of $\sigma$ [26]:

$$\sigma = q^2 \int G(E) \, \frac{-\partial f}{\partial E} \, \mathrm{d}E \tag{1.2}$$

The derivative $\frac{-\partial f}{\partial E}$ is referred to as the window function (or selection function), which selects the contributing carriers to the transport. Similarly, using equation 1.1 when a temperature gradient is only applied gives the electric current due to a temperature gradient. The chemical potential is assumed constant in this case (short-circuit condition). This drives a material quantity ($\nu$), that $J = -\nu \bigtriangledown T$, similar to Ohm's law.

$$\nu = q \int G(E) \, (\frac{E-\mu}{T}) \, \frac{-\partial f}{\partial E} \, \mathrm{d}E \tag{1.3}$$

Note that the current here is induced only by the change in carriers' occupation between hot and cold sides. The term $(E-\mu)\frac{-\partial f}{\partial E}$ is the selection function for conduction under the temperature gradient condition only. In the case of having both temperature gradient and voltage gradient, the total current density will be an addition of both.

$$J = J_{\bigtriangledown V} + J_{\bigtriangledown T} = -\sigma \bigtriangledown V - \nu \bigtriangledown T.$$

The Seebeck coefficient is the voltage difference measured with open circuit condition (i.e. $J = 0$) when a temperature gradient is applied.

$$S = -\frac{\triangle V}{\triangle T} = \frac{\nu}{\sigma} \tag{1.4}$$

**Heat transport by electrons**

Heat conduction could be treated the same way as electronic charge conduction under Landauer formalism [26, 29]. Similar equations to equation 1.1 could be used for heat conduction that is done through both electrons and lattice vibration. The charge $q$ for each electron now should be converted to the heat carried by each $(E-\mu)$. The heat current density carried by electrons only ($J_Q$) is derived either by a temperature or a voltage gradient. By using an Ohm-like equation for heat current carried by electrons ($J_Q = -k_e \bigtriangledown T$), one can get $k_e$ by adding the temperature gradient component ($k_0$) and the voltage gradient component [26].

$$k_e = k_0 - S^2 \sigma T \tag{1.5}$$

$$k_0 = \int G(E) \, \frac{(E-\mu)^2}{T} \, \frac{-\partial f}{\partial E} \, \mathrm{d}E$$

.

**Heat transport by phonons**

The lattice thermal conductivity ($k_L$) could be calculated from the heat current density due to the temperature gradient only. Because the lattice vibration does not respond to voltage gradient but responds only to the temperature-induced Bose-Einstein's spatial gradient ($\bigtriangledown f_b$). Again, we use the Ohm-like equation for heat current carried by lattice vibration ($J_Q = -k_L \bigtriangledown T$) to obtain $k_L$.

$$k_L = \int G(E) \frac{(E)^2}{T} \frac{-\partial f_b}{\partial E} \, \mathrm{d}E \tag{1.6}$$

$$f_b = \frac{1}{\exp\left(\frac{E}{k_B T}\right) - 1},$$

where $f_b$ if Bose-Einstein distribution of phonons having energy $E$ [33]. The selection function for heat carrieng bosons here is $(E)^2 \frac{-\partial f_b}{\partial E}$ [26]. The difference between electrons and phonons regarding Landauer equations appears in two points [29]. First, electrons and phonons contribute to the transport in different order of magnitude energy scales; at a certain temperature, few electrons may contribute while most of the phonons flow [29]. Second, the mean free path of electrons ($\lambda_e$) and phonons ($\lambda_p$) have different energy dependence; at room temperature, $\lambda_e$ is nearly constant, but $\lambda_p$ depends on $E^{-2}$ [29]. This tells us that acoustic (low-energy) phonons have longer $\lambda_p$ than the electrons, but the optical (high-energy) ones have a relatively shorter mean free path.

### 1.3.3 Optimising the thermoelectric efficiency

One technique to enhance the value of the thermoelectric figure of merit is to optimise the electrical transport properties of the low thermal conductivity materials. Chang and Zhao [34] summarized the correlation between the thermoelectrics' low thermal conductivity and the anharmonicity in its lattice. The lattice vibrations transfer the heat from one side to another, usually represented by atoms connected by springs to their neighbours. The atoms' oscillation is considered harmonic in the ideal crystalline system. The anharmonicity breaks this symmetry (harmonic oscillation) and result in disordered vibration modes. Therefore, the rising phonon-phonon collisions causes the reduction of the phonon's lifetime $\kappa$, and consequently, leads to small lattice thermal conductivity[34]. They also outlined the three main strategies used to enhance the anharmonicity as fol-

lows:

1. Lone pair electron (LPE): two non-shared electrons cause a nonlinear electrostatic repulsion force with their neighbouring bonds leading to more anharmonicity and hence reducing the lattice vibration [35, 36]. This was reported for different nitrogen group elements (e.g. As, Sb, Bi) and with some of their compounds, having strong active LPEs [34, 37–39].

2. Resonant bonding: unlike the anharmonicity caused by the asymmetry in the atomic arrangement, some high-ordered structures like rocksalt IV-VI compounds (PbTe, PbSe, SnTe) reveal strong anharmonicity because of their resonant bonding [40]. In these compounds, the coordination number is six, so the electrons have to swap their positions among the six covalent bonds in a resonant manner [41].

3. Rattling model: it was first discovered in cage-like structured materials (clathrates and skutterudites) with one guest atom or cluster oscillating vigorously inside a large cage space because of its weak bonding with the host lattice [42–45]. There may be more than one strategy to increase the anharmonicity of a certain material like the rattling found in TlInTe and InTe is induced by LPEs [46, 47].

There are many research groups using these concepts to optimize $ZT$ in Sn chalcogenide compounds as an alternative for PbTe, the best-known but not environmental-friendly compound. For example, one group used the layered structure of bulk SnSe that result in weak Van der Waal's bonding and low sound velocity, leading to small thermal lattice conductivity; they could then optimize the carrier concentration by Br and Se doping [48]. Another group engineered the electronic structure of bulk SnTe by using two dopants for different purposes: (a) Ca was used to increase the band gap to suppress the bipolar thermal conduction, and (b) In was used to enhance the Seebeck coefficient by introducing resonant levels. This method succeeded to improve $ZT$ in a wide temperature range [49].

In ZnSb compounds, the inherent low thermal conductivity arises from the unusual ZnSb phononic structure [50]. There is weak electron bonding that, probably, permits more phonon-phonon interaction. This interaction may occur between acoustic and optic modes, which is otherwise prohibited. In which, various localised low-energy optic modes serve as rattling modes with thermal acoustic phonons. Moreover, higher temperatures promote phonon-phonon scattering (umklapp processes) [50].

Another technique to optimize the thermoelectric efficiency is to keep the high electrical transport properties and then lower the lattice thermal conductivity. This

strategy succeeded with some systems such as tin and lead chalcogenides but failed with other semiconductors as the introduced defects not only affect the phonon transport but also bound the electronic transport [34, 51–53]. The discovery of the topological insulators showed a promising solution for this problem as they have topologically-protected metallic surface states, that are immune to non-magnetic impurities.

## 1.4 Thin films

Reducing the dimensionality of the TE material (e.g. in thin films) improves the thermoelectric properties due to quantum confinement that improves the PF and $ZT$ [16, 17, 54]. Thin film application is also more suitable for integrating with small and flexible TE devices [19]. Additionally, in topological insulators, this enhances the surface-to-bulk ratio that emphasises the surface state contribution in the electrical conduction and reduces the bulk thermal conduction [12]. In the present study, thermoelectric thin films were prepared using different physical vapour deposition (PVD) techniques. Here, the thin film formation mechanism and the impact of the growth conditions (e.g. substrate temperature) on the prepared films are discussed. In chapter 2, the techniques are briefly discussed, while the specific details of each film's growth are mentioned in their corresponding experimental chapter.

### 1.4.1 Thin film growth mechanism

In PVD, the vapour of the film's material is condensed on a substrate to form a thin film. The process occurs in two stages. The first one is nucleation when a flux of adatoms hits the surface of the bare substrate. In this stage, each adatom diffuses randomly on the substrate surface affected by its potential and other barriers (e.g. from the substrate and other adatoms) [55, 56]. There are two competing interaction energies that determine the growth mode: the adhesion with the substrate ($W_{SD}$) and the cohesion with other deposited atoms ($W_{DD}$). If the adhesion's energy is higher, the first layer will be covered first then the following layer and so one ( called layer growth) [56]. But, if the cohesion energy is higher, the atoms will tend to form islands (called island growth). In between, there is the Stranski-Krastanov growth, when the cohesion and adhesion energies depend on other parameters such as the substrate strain field and wetting properties [56].

During the nucleation, adatoms accumulate forming clusters, which could grow by attachment of more adatoms continuously or less likely shrink by detachment, forming adatoms clouds around the clusters [55]. As these clusters (or grains) grow, the ratio

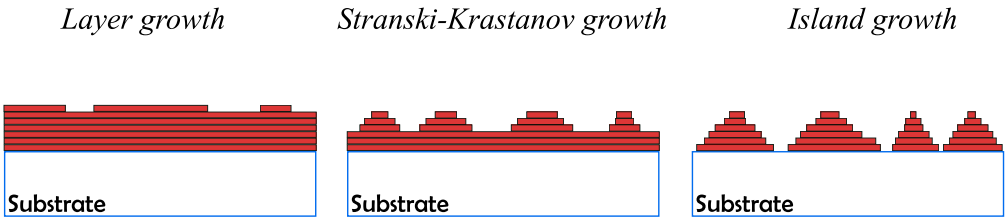


Figure 1.6: The three possible growth modes of thin films grown by a physical vapour deposition technique.

of attachments to detachments increases, lowering the cloud density. Consequently, the atoms migrate from the high-density clouds (around the smaller clusters) to the low-density cloud (around the bigger clusters) [55, 57]. As grains grow, they touch and restructure (i.e. coalescing) to minimise the total surface energy of the system. During this process and the following growth stages, the microstructure of the film evolves [55, 58]; it could be classified from high-ordered single crystal to textured (i.e. preferred orientation), polycrystalline (random grains) and amorphous (no grains).

Some factors control how much the film will be ordered such as the temperature of the substrate, the flux (i.e. the deposition rate) and the kinetic energy of the atoms (e.g. in sputtering) [55, 56, 59, 60]. In general, high substrate temperature increases the in-plane diffusivity of the adatoms allowing them to have a higher probability to rest in more stable clusters quickly before building new layers. In addition, it increases the recrystallisation rate which results in highly-ordered films. However, a very high temperature is not desired for epitaxial growth and some compounds have a narrow temperature window, below which, the disorder increases, and above it, 3D islands appear [13]. The low deposition rate also gives the in-plane diffusing atom more time to reorder. Otherwise, with a high deposition rate, more adatoms and small grains will behave as barriers to adatom mobility, increasing the number of small grains and defects. To form a high-quality single-crystal film, a higher temperature and very low deposition rate are required; this will give the natural lowest-energy crystallographic orientation. If a different film orientation is required, a single crystal substrate with specific properties (e.g. orientation and lattice parameter) could be used to encourage "epitaxial" growth, where the thin film has a well-defined crystallographic orientation to the substrate.

The single crystal has flat terraces and atomic steps on the top. During the epitaxial growth, adatoms can rearrange in different modes; it ranges from step flow, where fast diffusing adatoms attach to the step edges of the terraces, through layer-by-layer and mound formation, to self-affine or hit-and-stick growth (i.e. adatoms stick where

they land) [55, 60]. Again, the intra-layer diffusivity depends on the above-mentioned factors and diffusion barriers. For example, in the mound formation mode, adatoms are trapped in many small islands that build up high roughness [55]. Note that the effect of surface structure is more pronounced in small thicknesses, which demands controlling the growth conditions (e.g. by molecular beam epitaxy).

### 1.4.2 Polycrystalline films

To understand growing thicker polycrystalline thin films, one can treat it from the crystal point of view. It starts with nucleation, from the condensation of the adatoms on the substrate (i.e. primary nucleation) to the coalescence in a fluid manner (i.e. secondary nucleation) [59]. After that, crystal growth occurs, first, when different grains try to minimise their interface energy with the substrate by changing their orientation. Second, when they grow, different-oriented crystals compete together to change texture and morphology (i.e. competitive texture). The following thickening of the film (i.e. grain growth) includes boundary migration and periodic coalescence, where grains increase in size and reorient to lower the total energy. The "restructuration growth" texture related to this process is due to minimising the surface and interface energy [59]. In addition, coarsening (i.e. atoms diffuse from one island's surface to another or through their grain boundaries) could occur during grain growth, film thickening or annealing after deposition [58, 60]. Post-deposition annealing can increase the grains size considerably (exponentially in some cases), relax stresses and defects and, even, crystallise amorphous films [60, 61].

The growth structure and morphology depend on the ratio of the substrate temperature to the melting point of the film ($T_s/T_m$); it is usually classified into different zones (e.g. Figure 1.7 [59])

Doping the thin film with certain impurities (i.e. additives) can have a great impact on the growth mechanism [55, 59]. In the nucleation stage, impurities can block certain growth directions and direct the growth to develop a second phase [59, 62]. During the grain growth stage, it could be either adsorbed or segregated on the growing crystalline face, and actively impact the grain size; they could be inhibitors which diminish the grain size and weaken the texture or promoters which extend the crystalline grains [55, 59].

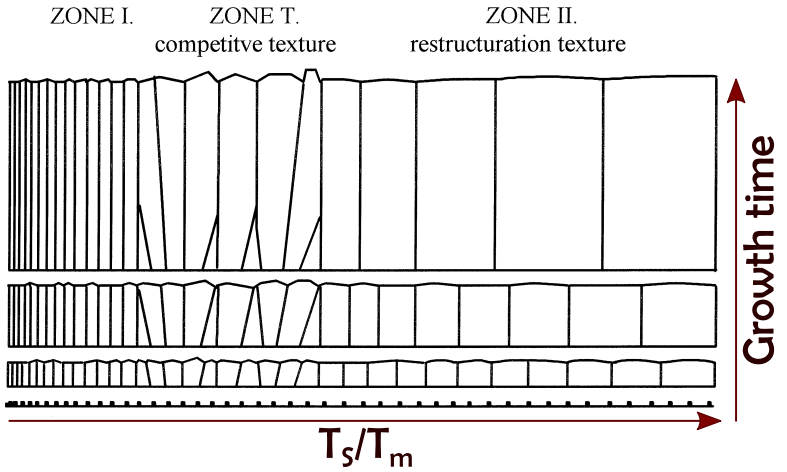


Figure 1.7: Illustration of different polycrystalline zone models as a function of the substrate temperature to the melting point of the film, Reprinted with permission from [59].

### 1.4.3 Substrates

The substrate choice plays an important role in the orientation of the film's grains, some can act as templates. The grains starts randomly oriented, some orientations are more favourable than others due to their low surface energy which makes them more stable. Therefore, higher energy surfaces tend to restructure to more stable configurations if there are no kinetic restrictions [58, 63]. For amorphous substrates (e.g. glass), grains tend to orient according to the crystallographic face with the lowest surface energy [59]. On the other hand, a single crystal substrate restricts the film growth in a specific orientation based on the substrate's in-plane configuration [58]. In the present study, different substrates were used (see Figure 1.8), from crystalline planar wafers (InAs and InP) to non-crystalline planar (i.e glass) substrates and non-planar substrates (Kapton and nano-patterned InP). Certainly, the substrate's surface contaminants affect the film's nucleation process by making additional barriers to the adatom migration and creating new nucleation centres [63]; this reduces the ordering and adhesivity of the film. Therefore, the surface of such substrates requires suitable preparation to remove contaminants and oxide layers via either chemical detergents or wet or dry etching (in the present study, argon ion sputtering). Additional deposition of a buffer layer (e.g. SnO treatment in chapter 5) may improve the quality of the film as well [64, 65]. The substrate preparation is detailed in the experimental chapters.

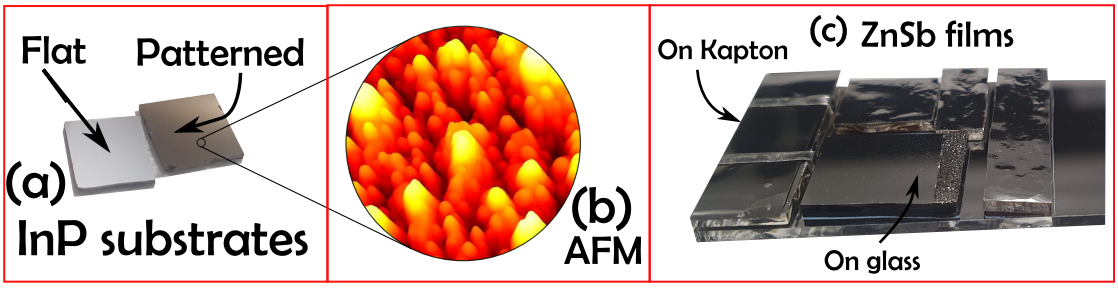


Figure 1.8: Different thin film samples were grown in this study on various substrates. (a) Flat and nano-patterned InP substrate; (b) is the corresponding AFM topograph, on a different scale. (c) ZnSb thin films grown in one growth on different substrates.

## 1.5 Thesis organisation and aim of the study

In this thesis, two thermoelectric thin film systems were studied (BiSb and ZnSb), plus, pure Sb thin films, as mapped in Figure 1.9. Chapter 2 provides the concept of the experimental techniques used in the thesis, including thin film preparation, structural, compositional, optical, electrical and thermoelectric properties and work function of the studied films. In chapter 3, the technical work related to the vacuum system building and the experimental development is reported. This includes the building of a new UHV system to grow the BiSb films, regular maintenance of the other systems, building different vacuum-compatible items and setting up an automated experiment to bend ZnSb films on flexible substrates regularly. Chapters 4 to 6 discuss the experimental work on BiSb, ZnSb and Sb thin films, respectively. Each chapter starts with a literature-based focused introduction followed by the samples' preparation details and the discussion of the experimental results. At the end of the chapter, the conclusion highlights the main output results.

BiSb is a topological insulator TE material, its thermoelectric performance was studied after increasing its surface area by depositing on ion-irradiated nano-patterned InP substrates. While ZnSb films were prepared on chemically-treated glass and flexible Kapton substrates. The electrical and optical properties of the flexible samples were compared to the glass ones and tested after being bent for thousands of cycles. The last chapter compares an Sb film grown epitaxially on an InAs substrate to one grown on a glass substrate. The discussion presents the structural and morphological differences and presents some electrical and optical data and work function measurements.

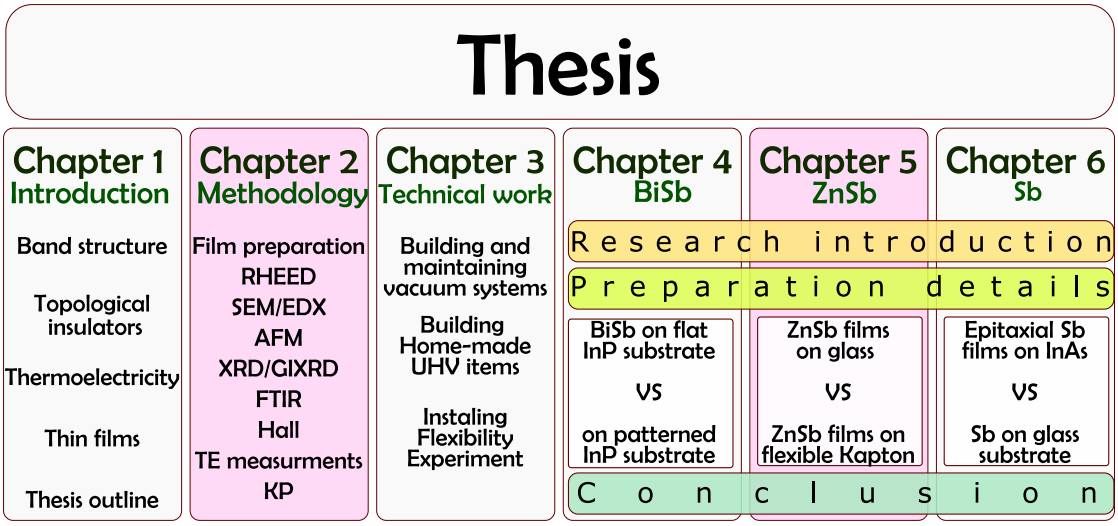


Figure 1.9: Thesis outline, highlighting the main ideas.

# Chapter 2

# Experimental Techniques

The experimental techniques used in this thesis are discussed in this chapter. In the first section, an overview of the preparation techniques is introduced. More information about their dedicated vacuum systems and their maintenance is discussed in Chapter 3. In the experimental chapters (4, 5 and 6), the specific details of the preparation conditions of each compound are provided. In the second section, the experimental analysis techniques used in this thesis are discussed. To grow our samples, different growth and characterise techniques were used, such as:

- Vacuum
- Physical vapour deposition (PVD) (Evaporation, molecular beam epitaxy (MBE), Sputtering)
- Lithography

The second part discusses the main techniques used in the analysis including:

- Reflection high energy electron diffraction (RHEED)
- Microscopy (The scanning electron microscope (SEM), energy dispersive X-ray (EDX) and atomic force microscope (AFM))
- X-ray diffraction (XRD) including grazing incidence (GIXRD)
- Optical measurements
- Hall and 4-point probe electrical measurements
- Thermoelectric measurements
- Kelvin probe (KP)

## 2.1 Preparation techniques

### 2.1.1 Vacuum

Regardless of the used technique, the deposition of good thin films requires a very clean environment. This means that we need no air inside the system (i.e. vacuum) because the air contains different elements that will contaminate the film's surface, contribute to the composition, or affect the performance of working instruments. There is no zero pressure, but instead, there are different levels ranging from the atmospheric pressure (≈1000 mbar) to extremely high vacuum ( $10^{-12}$ mbar). However, at a pressure of $10^{-9}$ mbar, a monolayer can form on the sample's surface within one hour if all particles adhere to it. At a poorer pressure (such as $10^{-6}$ mbar), this monolayer will form in just a few seconds [66]. In this thesis, the level of base vacuum used varies from the high vacuum (HV) ($10^{-7}$ mbar) for ZnSb films to ultra-high vacuum (UHV) ($10^{-9}$ mbar) for Sb and BiSb thin films. Here, the preparation techniques used to grow our final samples are discussed. The systems and procedures used to maintain these vacuum levels are described in Chapter 3 in detail.

### 2.1.2 PVD

In this study, three different PVD techniques were used to prepare thin films in the nanometre range, namely: thermal evaporation, magnetron sputtering and MBE. In general, the source material gets evaporated by a means of energy such as thermal heating, or ion bombardment. The thin film is obtained by depositing the vapour of the source material on a substrate inside a vacuum chamber [56, 67]. We used HV and UHV systems which require continuous maintenance as explained in detail in Chapter 3. In the thermal evaporation (or low-pressure PVD) technique, the source material is thermally heated until it reaches its evaporation temperature; its vapour is then deposited on the desired substrate to form a thin film. The source material is usually put in an open crucible made of either a high-resistance, high-melting point metal (e.g. tantalum boat) or ceramic crucible with high thermal conductivity and electrical insulation (e.g. molybdenum) which is wrapped by a spiral filament. The latter offers more collimation to the material's flux. ZnSb thin films were deposited in a low-pressure PVD (LP-PVD) system (Mercutio), and BiSb (i.e. MP5x samples) films were grown in the commercial Mantis thin films deposition system. Similarly, the MBE technique involves sublimating or evaporating a source material and depositing its vapour onto a substrate to form a thin film, but with a specific crystallographic orientation. Usually, this is achieved by

growing the thin films on a single crystal substrate (e.g. InAs(111)B). In a UHV, non-interacting molecular beams of the source material travel from the effusion cell with a longer free path until reaching the hot substrate. By controlling the source's flux and the substrate's temperature, extremely high-quality films could be obtained, which could be reproduced consistently [13, 67]. The essential high level of cleanliness and UHV makes it very expensive to run these systems, it is used mainly when very high quality is required in the industry (e.g. optoelectronics). This technique was used to grow Sb films on InAs (111)B substrates (Chapter 6) and BiSb films on InP (100) substrates (Chapter 4). On the other hand, the magnetron sputtering technique does not involve heating the source material thermally. Instead, a target material is bombarded with gas ions such as $Ar^+$ and the sputtered atoms are deposited onto a substrate to form the thin film. The deposition could be controlled by adjusting the pressure of the gas used and the sputtering power. This technique offers good-quality deposition in a shorter time than other techniques; we have used it to deposit a gold electrode layer by lithography for thermoelectric measurements (Chapter 4).

### 2.1.3 Lithography

When seeking a thin film of a certain configuration or a practical device, we often use some sort of masking. This masking could be done using a physical metal mask that can cover parts of the substrate as mentioned in Chapter 3. Another form of masking could be done using lithography which ensures high precision with the pattern dimensions and its fine features down to micron- and submicron-ranges [68]. In general, the method involves covering the sample with a chemical photo-sensitive material which either stays or leaves when being exposed to light and developed. This includes different stages[68]:

- Photoresist coating: includes spin-coating the photoresist to form a thin film with a uniform thickness on the sample. The photoresist has two types: positive photoresist, when exposed to UV light, becomes more soluble in the developer solution), and negative photoresist. Special precautions should be considered not to expose the undeveloped photoresist to white light; the whole process is done in a yellow-lighted partition inside the clean room (in Physics, Warwick).

- Soft baking: the film is heated at a low temperature that removes any solvents from the photoresist, enhances its adhesion and relaxes the film from residual stresses.

- Exposure: the photoresist is exposed to a pattern of light of a specific wavelength for a specific duration enough to alter the chemical structure of the used photoresist

compound. Figure 2.1(a) illustrates the exposure of a positive photoresist to UV light, changing the original photoresist structure (from red to pink). In this study, a micro-pattern generator ($\mu$PG 101) was used to focus a laser beam of a certain power using different suitable lenses (i.e. optical heads) and filters to control the speed and resolution of the exposure for the desired photoresist. The equipment uses the user's provided digital mask design to expose the sample after being aligned and fixed in position by a rough vacuum.

- Post-exposure bake: includes baking the photoresist after being exposed. This could be done for different reasons, for example, to complete the chemical reaction of the photoresist, or to achieve a uniform development rate for reflective substrates [68].

- Developing: the exposed photoresist is developed by rinsing in a developer solution (often alkaline NaOH- or KOH-compounds) for a specific duration to avoid destroying the whole photoresist layer. The selectivity of the developer is the ratio of the erosion rate between the developed-to-be photoresist and the remaining photoresist (mask). Figure 2.1 (b) illustrates the photoresist after being developed.

- Deposition: the target metal is deposited by the desired technique on the whole substrate including the photoresist mask (Figure 2.1 (c)). In our study, we deposited gold by Moorfield NanoPVD magnetron sputtering system.

- Liftoff: after depositing the desired material, the photoresist is then dissolved by a suitable solvent. This step wipes off any residual photoresist, along with any metal deposited on top of that photoresist, leaving the deposited material on the unmasked regions only (Figure 2.1 (d)).

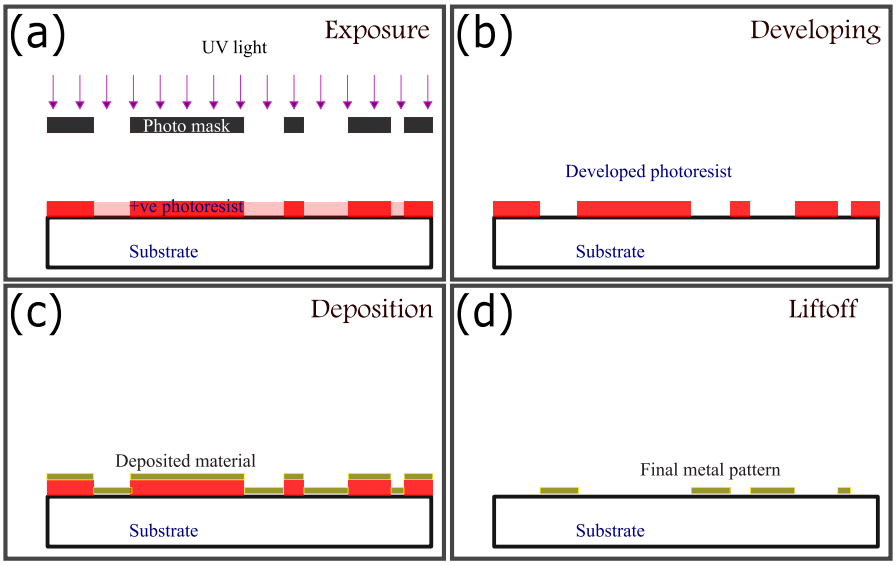


Figure 2.1: Illustration of the photo-lithography technique to obtain a patterned film using a positive photoresist. (a) exposure; (b) developing; (c) film deposition; (d) liftoff process.

## 2.2 Characterisation and measurements

### 2.2.1 RHEED

RHEED is a widely used surface characterisation technique in which a beam of high-energy electrons is directed to the surface of the sample at a grazing angle [69], (5-30 keV). The diffracted beam is then detected by a phosphor screen, which produces a diffraction pattern (see Figure 2.2 (a)). The analysis of this pattern can provide valuable information about the sample, such as the periodicity of the film's surface and its relationship to the substrate, the surface roughness, the growth nature, and the lattice parameters [69]. RHEED is especially useful because it is easy to use even during the film growth, and provides a huge wealth of information [69]. Here are some valuable information we were able to deduce from RHEED analysis, and how:

- Whether the sample is polycrystalline or single crystal (or a mixture) by observing the shapes of the diffraction pattern (Figure 2.2 (b-f)). We can also determine if there is surface reconstruction or not from the presence of fractional order streaks between the integer streaks (Figure 2.2 (c)).

- The rotational symmetry feature was determined by rotating the sample around the z-axis and then measuring the angle between two identical patterns. For example,

the surface has 4-fold rotational symmetry if the same characteristic pattern could be obtained by rotating the sample every 90 degrees.

- The inter-row separation ($a$) or in-plane displacement by measuring the separation between the pattern streaks ($s$) and knowing the distance between the sample and the screen (i.e. camera length, $L$) (See Figure 2.2 (a,b)). $a = \frac{2\pi L}{Ks}$, where $K$ is the electron wave number ($\frac{2\pi}{\lambda}$) [70]. Since the uncertainty in measuring $a$ is related to that of determining the $L$, where $\frac{\delta a}{a} = \frac{\delta L}{L}$. And, $L$ depends on the position of the sample inside the chamber, which may change (a few millimetres) when adjusting the direction of the electron beam on the sample. This can result in $1-2\%$ error in the determined lattice parameter [71]. Therefore, to minimise our uncertainty in $L$, it was evaluated while the sample was in position by knowing the substrate's in-plane displacement in one direction (see RHEED in Chapter 6).

- The quality of the surface and bulk of the samples from the presence of Kikuchi patterns. Crystalline samples with perfect bulk lattices and surfaces produce sharp Kikuchi lines (Figure 2.2 (b)) [70].

- The presence of 3D ordered islands on the surface (rough surface) is concluded when the streaks in the diffraction pattern change to an array of dots forming transmission patterns. This dominates when the electron beams scatter more from deeper levels than the surface, showing the reciprocal lattice that consists of an array of points (dotted lines in Figure 2.2 (e)) [70].

- The presence of some facets on the surface of the film (e.g. regular pyramids) is confirmed by observing the splitting of each streak to form an angled shape (Figure 2.2 (d)).

In this study, to understand the bulk and surface of the films, RHEED patterns are interpreted supported by XRD analysis (i.e. BiSb films) and/or by using CrystalMaker software for better visualisation of the surfaces (i.e. Sb films). For example, XRD can tell us the surface plane orientation of the film. CrystalMaker helps to visualize this plane and its rotational symmetry elements, and RHEED determines the film's in-plane displacement, which can be compared to corresponding bulk values to understand the strain in the film.

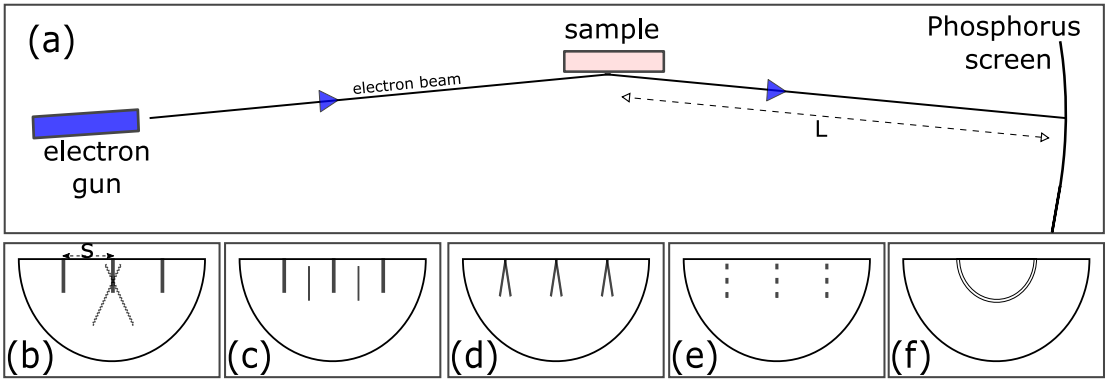


Figure 2.2: Demonstration of the RHEED setup, showing the accelerated electrons ejected from an electron gun and directed towards a rotatable sample, then reflected to a phosphorus screen (a). Different RHEED pattern features: (b) integer streaks with Kikuchi lines, (c) fractional-order streaks (2× surface reconstruction), (d) faceting, (e) transmission diffraction (3D islands), and (f) transmission powder diffraction rings. The parameters $s$ (streak separation) and $L$ (camera length) are used to deduce lattice parameters.

### 2.2.2 Microscopy (SEM/EDX and AFM)

#### SEM/EDX

SEM is one of the most common techniques used to image the topography of the samples' surface down to the nanometer range. In this technique, a beam of primary accelerated electrons collides with the surface of the investigated sample as presented in Figure 2.3. In the case of thin films, if they have enough energy, the primary electrons may penetrate the film totally and reach the substrate. Some of these electrons (10-50%) could be backscattered elastically with (60-80%) of their original energy ($>$ 50 meV ), called backscattered electrons (BSE) [72, 73]. Some others collide inelastically with the sample and transfer energy to the atom, freeing loosely bounded electrons, called secondary electrons (SE). SE electrons contain very valuable information about the topography of the sample as they only escape from the few-nanometre surface layers with small energies around 3-5 meV; this type is the most commonly used signal for visualising the textures and roughness in SEM imaging [72]. Besides, after displacing an original inner shell electron by primary incident electrons, an outer shell electron can fill its vacant position; this produces characteristic X-rays that could be detected using an EDX detector and used to identify the sample's composition. The SEM/EDX system uses different electromagnetic lenses, detectors and software to separate signals, filter undesired ones (e.g. Auger electrons or X-ray continuum) and calculate the chemical composition of the

studied samples [74]. In this study, the elemental composition of BiSb and ZnSb films was determined by Zeiss SUPRA 55-VP field emission gun scanning electron microscope (FEG-SEM) with Oxford Instruments energy-dispersive X-ray (EDX) spectrometer, using an accelerating voltage of 7 kV. This range of energy was enough to ionise all the studied elements and get sufficient counts for EDX quantification (Note: $L_\alpha$(Zn): 1 KeV, $L_\alpha$(Sb): 3.6 KeV and $M_\alpha$(Bi): 2.4 KeV) [Periodic Table of Elements and X-ray Energies, Bruker]. Certainly, if higher energy is used, the contribution from the bulk will be higher. For each sample, the composition was averaged from three regions along its diagonal to obtain better quantification and ensure the homogeneity of the samples. The final atomic compositions were acquired from AZtec software using the default quantification settings after allowing more time (1-3 min/ scan) to collect the many counts and minimise the statistical errors. Specimen charging is one of the major problems in SEM imaging as the accumulated negative charges from the primary electrons beam form a layer that reflects following scanning electrons (like an electron mirror) and prevents it from reaching the sample [73]. To discharge our samples, especially with insulating substrates, during the measurements, the samples were grounded by wire-connecting their surface to the stage, carefully to avoid scratching the surface. For very rough samples like patterned BiSb films, the composition was determined from flat samples put in the same growth for better estimations; the composition values were very close although the patterned samples have more substrate contribution as they have a smaller average thickness (see Chapter 4).

**AFM**

AFM is one of the powerful tools used to obtain high-resolution images of a sample's surface topography. AFM is based around a long cantilever with a small, sharp tip at the end (Figure 2.4(i)). When scanning the surface of the sample, the sample stage moves rapidly in one direction called the fast scan-axis (e.g. the x-direction) to complete a line, then moves one step in the slow scan axis (y-direction) to scan the next line in the x-direction. During this motion, the tip moves up and down in the z-direction due to the intermolecular force between the surface and the tip. To accurately detect this z-motion, a laser beam is reflected off the cantilever and received by a photodiode sensor. The position of the reflected laser beam changes accordingly, allowing the machine to create a 3D map of the scanned region [75]. The AFM is better at measuring vertical dimensions in the nanoscale than the SEM, so we used it as the main tool for measuring the samples' roughness and thickness. It is also distinguished by not requiring a vacuum

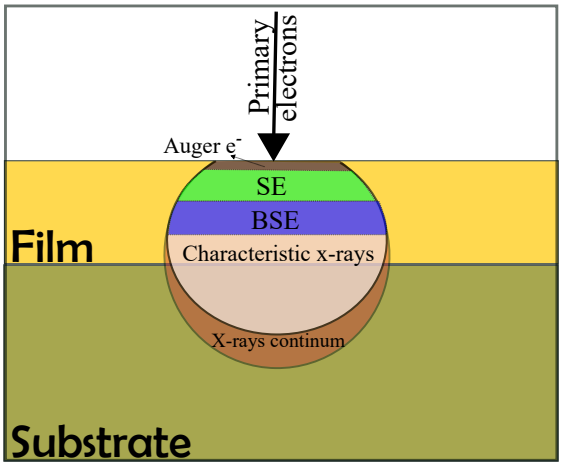


Figure 2.3: Illustration of the reaction of the accelerated primary electrons with a studied thin film sample in the SEM. The labels indicate, roughly, the area from which each particle/wave signal comes. We assume that a 7 kV beam penetrates a 100 nm thick film on a very thick substrate. Inspired by images in textbooks (e.g. [72]).

and not requiring sample preparation. It is also suitable for non-conducting samples, in contrast to SEM or scanning tunnelling microscopy (STM). However, it is slower in acquiring images, limited to smaller x-y scan sizes, and is not suitable for samples with significant variations in z-depth because the tip could be easily contaminated or damaged by the samples or the surrounding, which can produce image artefacts such as double-tip [75]. In this study, the sample surfaces were imaged using Bruker Dimension Icon AFM for better depth resolution in roughness and thickness measurements. The AFM was run in the default "Scanasyst" tapping mode, while acquired datasets were then processed using Gwyddion 2.59 package [76, 77]. In all our surface topography scans, a new tip was selected or a nearly new tip that gives high-quality artefact-free real topography. Figure 2.4(iii) shows the graphical user interface of Gwyddion software, (a) is the main tools and menus panel, (b) is the topograph image panel and (c) is the analysis output panel. The most used tools for the data set analysis are labelled in panel (a) as follows:

- Tool (1) is used to display a 3D view of the data, mainly used to visualise the surface of the BiSb patterned samples (Chapter 4).
- Tool (2) is the watershed tool, that was used to mark grains in the topographs to produce a histogram of the ZnSb film grain's equivalent disk radius (explained further in Chapter 3).
- Tool (3) is the polynomial background removal tool. This was used to make tilt

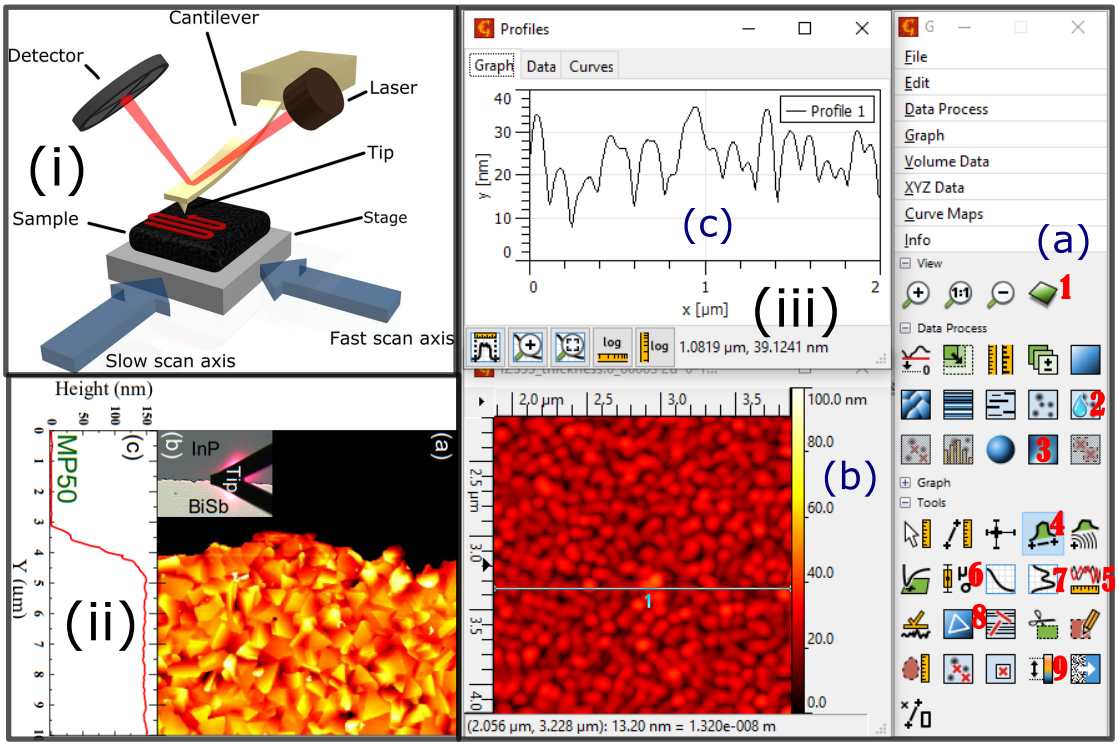


Figure 2.4: (i)Typical AFM instrument, reprinted with permission, from reference [75]. (ii) Thickness measurements of one sample (MP50). (iii) Gwyddion software interface: (a) tools panel, (b) image panel and (c) analysis output panel. Tool buttons used frequently in this work are highlighted by numbers.

and bow corrections from the data set. Care was needed while using this tool to reduce the negative bias in roughness measurements. This bias was estimated using the correlation length (tool (5)) to estimate the ratio ($\alpha$) between the autocorrelation length ($T$) and the image dimension (L), $\alpha = T/L$, and the relative bias $= -\alpha\times$(polynomial order $+1$) as described by Necas et al. [78, 79]. To minimise this bias, we need to increase the scan size (that might be difficult with very rough surfaces that cause a tip crash or contaminate the tip when it touches the surface) and minimise the removed background polynomial order. In most images, the bias did not exceed 10%.

- Tool (4) extracts the height profile of an arbitrarily drawn line such as shown in panel (iii) (b-c). This tool was used to study individual grains as well (e.g. Sb pyramids on InAs substrates, chapter 6).

- Tool (6) was used to determine statistical quantities such as root-mean-square

(RMS) roughness and the surface and projection areas that determine the surface ratio (SR) value, SR = surface area/projection area. This value is used in this thesis as a measure of the surface area increment when patterned by Ar-sputtering, SR $\geq 1$, approaches 1 for flat surfaces.

- Tool (7) is used to determine the mean height across different rows/columns, producing a mean height profile over a film-substrate-step to determine the thickness of the film, as shown in panel (ii) for one BiSb film. The step image (a) was taken as the AFM tip approached the edge of the film (b). In this case, we used tool (8) to level the flat substrate region (black) from three points, instead of using the background removal tool (3) which would consider the step as part of the background. Note that the thickness was determined for films grown on smooth flat surfaces such as glass or polished wafers (eg. InP) only. To produce the film-substrate step, part of the substrate was intentionally covered during the growth (e.g. by a form of mask). Sometimes the flux sneaks under the mask and forms a non-sharp edge that spreads over a long distance (e.g. 50 $\mu$m), which could not be scanned. Therefore, some films were gently scratched near the edge using a sharp tool (e.g. a razor blade or a tweezer with glass substrates) to remove the film and avoid scratching the smooth substrate. Several step images, like the one shown in panel (ii)(c), are obtained for each sample and the average step height is taken as the film thickness, weighted by the uncertainty in the profile average.

- Tool (9) was used to adjust the colour range of the output topograph and was used for consistent comparison between ZnSb films in Chapter 5.

### 2.2.3 X-ray diffraction

The XRD technique is widely used in materials science to study the structure and composition of materials. One of the advantages of XRD is its ease of use, the wealth of information it provides and the minimal sample preparation requirements. It is also a non-destructive technique, meaning that the sample is not damaged during the measurement. The XRD system, also known as a diffractometer, consists of an X-ray tube with optics such as collimators and filters that produce and direct X-rays of a specific wavelength ($\lambda$) (e.g. 1.5418 Å for Cu K$\alpha$) towards the sample being investigated [80]. The incident beam is then scattered by the different layers of the sample, and when Bragg's condition is satisfied [2, 81] (Figure 2.5(a)), the diffracted beam is detected by a moving detector at various angles. The resulting intensity-$2\theta$ graph consists of multiple

peaks for crystalline samples, but these peaks disappear and become a smooth distribution if the sample is non-crystalline. The position of these peaks ($2\theta$) is related to the distance between planes ($d_{hkl}$) in the scattering vector direction. If the sample has completely random grains, the relative intensities between peaks become a fingerprint characteristic of the material. By searching for the matching "cards" in databases (e.g. the PDF database [82]), one can identify the present phase(s) in the sample (search match). The XRD card has information about the structure of its phase with each peak assigned to its corresponding plane, for new materials this could be done by finding the relation between peak positions (indexing). If the relative intensities between peaks do not match the corresponding card or a family of peaks becomes dominant (e.g. $\{h00\}$), the sample probably has a preferred orientation [80, 83]. Other information about the sample can be obtained, such as macro-strain if the whole pattern is stretched, and micro-strain and average grain size from peak broadening using Scherrer equation [84, 85] or Williamson-Hall plot [86]. In our analysis, we used two XRD setup geometries, namely:

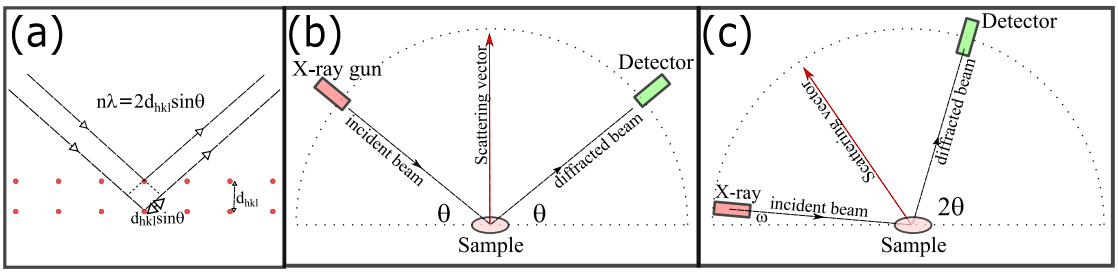


Figure 2.5: Illustration of the satisfaction of Bragg's law in XRD characterisation (a). Different instrumental geometries used in this thesis: (b) Bragg-Brentano geometry and (c) GIXRD. The scattering vector is normal to the surface only in Bragg-Brentano geometry. Illustrations are similar to reference [80].

(1) Bragg-Brentano geometry (or $\theta-2\theta$), and (2) GIXRD. Bragg-Brentano geometry (see Figure 2.5 (b)) is typically used with powder diffraction, slabs, and thick films, where the X-rays fall at an angle $\theta$ with the substrate plane and are collected from the other side at an angle of $2\theta$ with the incident beam direction; the scattering vector is normal to the substrate. With thin films, the X-ray beam penetrates the film and the substrate, which may dominate the diffraction pattern, especially at higher $\theta$ angles. This reduces the quality of the analysis considerably, as the overlap with the substrate peaks and background hinders various features. On the other hand, in GIXRD (see Figure 2.5 (c)), the incident X-ray beam is fixed at a small grazing angle ($\omega = 1°$ in this study) while the diffracted beam is collected at varying $2\theta$ with the incident beam. This geometry is

more convenient for phase identification in randomly oriented powders or polycrystalline thin films, but it fails to analyse the preferred orientation (e.g. texture coefficient) as the scattering vector is not normal to the sample's plane. We used the Panalytical Empyrean grazing incidence X-ray diffractometer (GIXRD) with polycrystalline ZnSb films operating at a 1° incident angle. The obtained data set was analysed using the HighScore Plus software, during which the background was removed, peaks were selected for phase identification (search match), and default Rietveld analysis (fitting) was performed for composition analysis (quantification) using the PDF4 database [82, 87]. Those films were fitted without considering the presence of a preferred orientation. The chemical compositions derived from EDX were used to constrain the phase compositions obtained from GIXRD in the following way. ZnSb and $Zn_4Sb_3$ were always included in the list of possible phases. Plausible additional phases (Sb, Zn, other $Zn_xSb_y$ , In2O3, etc.) were added and the fits were refined to give overall compositions close to EDX. While the GIXRD-derived compositions should not be considered fully quantitative, they agree within a few % with the EDX compositions, giving confidence that the phase compositions are reliable. Williamson-Hall (WH) analysis [80, 84, 86] was performed for near-stoichiometric ZnSb films using selected peaks (high intensity and low overlap) to obtain the average particle size ($D$) and local strain ($\epsilon$) in the films. WH analysis uses the following equation:

$$\beta_{hkl}\cos\theta = \frac{0.9\lambda}{D} + 4\epsilon\sin\theta,$$

where $\beta_{hkl}$ is the full width at half maximum (FWHM) of the peak with $hkl$ indices. The plot of $\beta_{hkl}\cos\theta$ against $4\sin\theta$ determines $D$ and $\epsilon$ from the intercept and slope, respectively. For BiSb films, the preferred orientation required using Bragg-Brentano geometry by the same diffractometer to calculate the texture coefficient TC($\gamma$) [88, 89].

$$TC(\gamma) = \frac{\frac{I_{hkl}}{I_{0hkl}}}{\frac{1}{N}[\sum_1^N \frac{I_{hkl}}{I_{0hkl}}]},$$

where $I_{hkl}$ and $I_{0hkl}$ are the intensity of the diffracted peaks in our experiment and the corresponding PDF card, respectively, and $N$ is the number of studied peaks.

### 2.2.4 Optical measurements

Semiconductors are typically insulators because all of their outermost electrons are bound in the filled valence band. When an electron gains energy, such as from light (photons),

it can be excited from the valence band to the conduction band if the photon's energy is greater than the band gap of the semiconductor. Determining the band gap of a semiconductor is very important because it determines how the material behaves with electromagnetic radiation and thus allows it to be used in appropriate applications such as solar cells and sensors. One method of determining the band gap is to expose the semiconductor to the light of different photon energies ($h\nu$) and detect when it absorbs these photons using the spectrophotometer. The absorption of energy indicates that the semiconductor has undergone some change, such as exciting an electron or breaking a covalent bond, depending on the energy range. The absorption depends on the material's absorption coefficient $\alpha$, which is defined by Beer-Lambert's law [90, 91]:

$$I(x) = I(0)\exp(-\alpha x),$$

where $I(0)$ and $I(x)$ are the initial intensity of the light and after travailing a distance $x$ inside the studied material. By acquiring the absorption spectrum $A(\lambda)$ of a film of thickness $t$ (see Figure 2.6 (a)), $\alpha(\lambda)$ could be calculated from:

$$\alpha(\lambda) = \frac{2.303 \times A(\lambda)}{t},$$

$$A(\lambda) = \log(\frac{I(0)}{I(t)})$$

The optical absorption coefficient of a semiconductor $\alpha(\lambda)$ depends on the energy of the absorbed light and the material's band structure. For a direct transition in a perfect crystalline semiconductor, $\alpha^2$ is directly proportional to $h\nu - E_g$ when the light energy exceeds the band gap energy $E_g$ [92]. The value of the $E_g$ can be calculated by extrapolating the linear least squares fit of $\alpha^2$ to zero on a "$\alpha^2$ against $E$" plot [91, 92] as illustrated in Figure 2.6 (b). This model does not apply to the disordered materials (e.g. amorphous) because of the existence of the tail states that need another approach [92]. Tauc plot [93] is one of the most convenient approaches to determine the gap in the non-crystalline semiconductors [6]. For polycrystalline materials, determining the band gap using the Tauc analysis approach was shown to be robust in terms of consistency, applicability and accuracy even when used by different research groups [94]. By plotting $(\alpha h\nu)^n$ against $h\nu$ and extrapolating the linear segment to the energy axis, one can determine the value of the band gap using the following equation [6, 93]:

$$(\alpha h\nu)^n = k(h\nu - E_g),$$

where $k$ and $n$ are constants, the value of $n$ is 2 or 0.5 for direct allowed or indirect allowed optical transitions, respectively, and 2/3 for direct forbidden and 1/3 for indirect forbidden transitions. If the sample has different compounds are multiple phases, this plot becomes more complex as the absorptions of different phases overlap. In this case, the obtained $\alpha(h\nu)$ will be a linear combination of the absorption coefficients $\nu_i$ of the constituents, that $\alpha(h\nu) = a.\alpha_1(h\nu) + b.\alpha_2(h\nu) + ...$ based on the Beer-Lambert law [90, 95], where a,b are constants. It becomes more difficult to separate each component [95] and identify the value of the optical band gaps and whether they are direct or indirect. Some efforts have been suggested to correctly determine the optical band gap using the Tauc equation manually or with an automated algorithm [95–97]. In our study, we used a manual graphical approach to identify the gaps from the intersection of the linear fit of the optical transition segment with the baseline (either $\alpha$=0 or the tail of low energy absorption as defined by a linear extrapolation) as explained by Makula et al. [95]. In Figure 2.6 (c), the direct Tauc plot is shown in black and the indirect Tauc plot is shown in red for a multiphase sample (IZS55). To identify whether the gaps are direct or indirect, firstly, Tauc plots were drawn for both transitions (i.e. $(\alpha h\nu)^2$ and $(\alpha h\nu)^{0.5}$ VS $h\nu$) and both gaps were identified. The solid lines represent the experimental data, while the dashed lines represent the linear fits or baselines (olive). Secondly, all indirect gaps obtained from a spectrum that strongly interfered with the direct transition's onset were not considered reliable as recommended by Suram et al. [96]. In this plot (c), as the indirect transition overlaps with the onset of the direct transition, it is omitted, and the gap is considered direct. This plot is considered to show the band gap of two phases at 0.66 eV and 1.03 eV.

The optical analysis in this thesis was done by acquiring the absorbance spectrum at room temperature. FTIR absorption spectrum was obtained using a Bruker Vertex 70V spectrometer under nitrogen in the near-infrared (NIR) region using a $CaF_2$ beam splitter and a DLaTGS detector. The scan range was selected from 2000 $cm^{-1}$ to 10000 $cm^{-1}$ with 1 $cm^{-1}$ resolution to scan the band gaps region of ZnSb films and avoid the undesired glass substrate absorbance region below 2000 $cm^{-1}$. The transparent substrate (glass or Kapton) was scanned first as a background for each sample to obtain the pure film spectrum. For films grown on Kapton, strong interference fringes were observed that overlapped with the film's NIR absorption spectrum, making it difficult to determine the band gap. We used a fast Fourier transform (FFT) filter in Origin software to quickly eliminate these interference fringes from the data without causing spectral artefacts as shown with the absorbance data of the ZnSb sample grown on Kapton (IZS55) in Figure 2.6 (d).

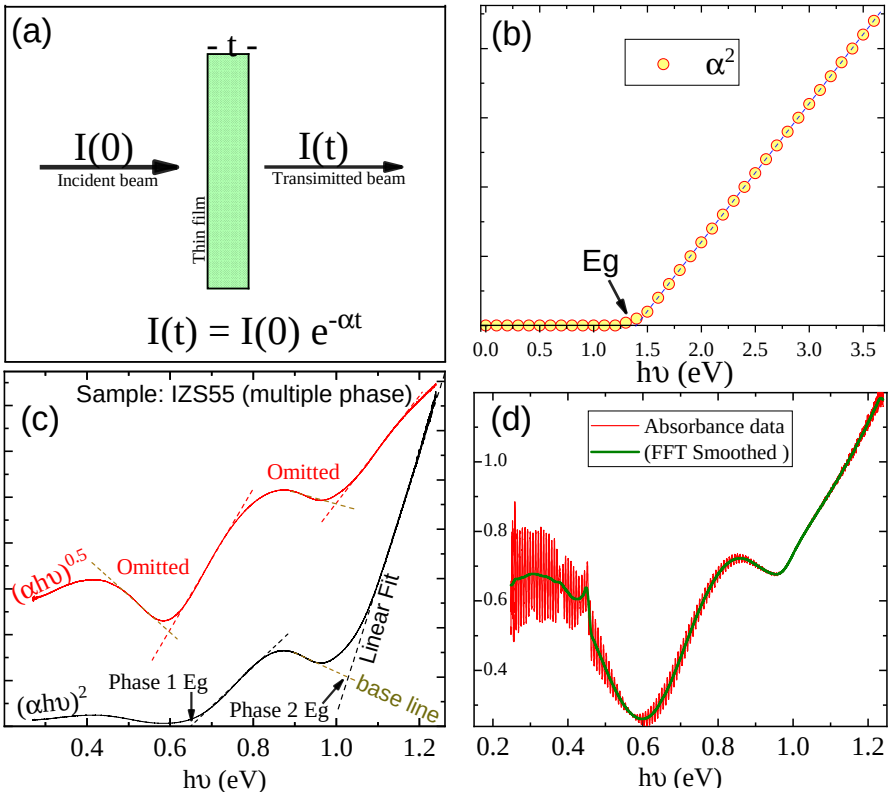


Figure 2.6: (a) Demonstration of the Beer-Lambert law for absorption. (b) Illustration of direct band gap determination in a perfect crystalline sample. (c) The direct (black) and indirect (red) Tauc plots of one multiphase sample (IZS55); the solid lines are the experimental data and the dashed lines are linear fits or baselines (olive) as presented. The indirect transitions are omitted when overlap with the direct transitions 'onset'. (d) The interference fringes associated with the absorbance spectrum of one film grown on Kapton (red), and the smoothed data using the fast FFT filter in Origin software.

### 2.2.5 Electrical measurements

Electrical measurements are crucial in the development and optimisation of semiconductor materials and devices. By accurately measuring the electrical properties of these materials, such as conductivity ($\sigma$), carrier concentration ($N_B$) and mobility ($\mu$), we can better understand their underlying physics to design more reliable and efficient devices. For a conductor material, if we apply a potential difference ($V$) across its terminals, a current ($I$) will pass through it inversely proportional to its resistance ($R$) ($V = IR$, Ohm's Law). The resistance of a uniform conductor depends on the dimensions of that conductor and the material's resistivity ($\rho$), that $R = \rho\frac{l}{A}$, where $l$ is the distance charges

travel and $A$ is the cross-sectional area. [1]. If a magnetic flux of density $B$ is applied

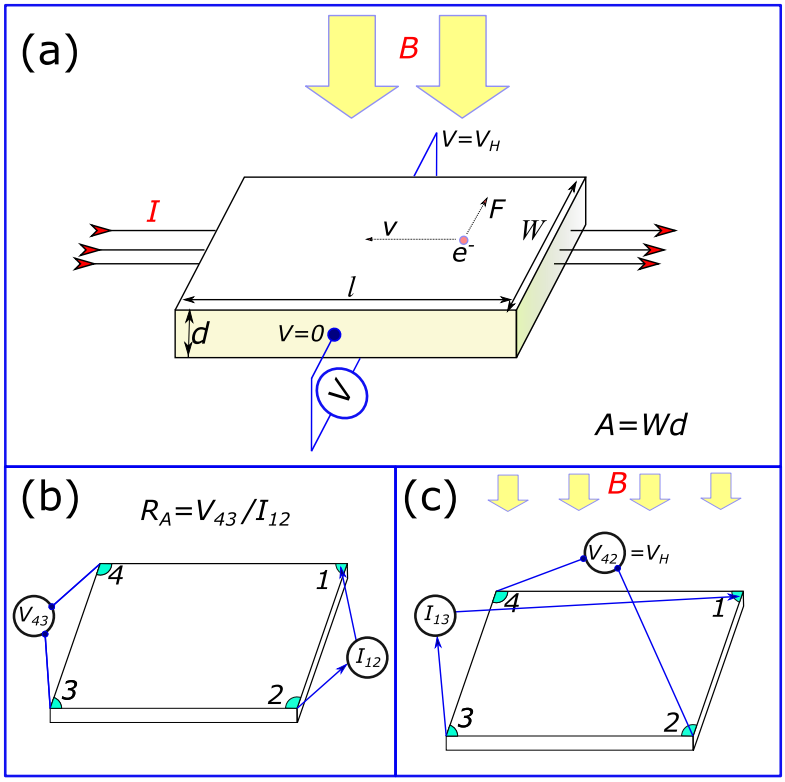


Figure 2.7: (a) Illustration of Hall effect when a current I passes through a conductor slab under magnetic filed $B$. (b) Resistance measurements for the Van der Pauw technique without applying a magnetic field. (c) Illustration of Hall voltage $V_H$ measurements under magnetic field. The image is inspired by [98].

normally to the direction of motion of some charges, each of charge ($q$) and velocity ($v$), a portion of them will be deflected to the sides by a normal magnetic force ($F_B = qv \times B$) as demonstrated in Figure 2.7 (a). This results in a small potential difference on the sides called Hall voltage ($V_H$), which depends on the number and mobility of the charge carriers and the magnetic flux applied, $|V_H| = IB/qN_Bd$, where $N_B$ is the bulk concentration, $I$ is the current passing through the film, and $q$ is the electronic charge ($1.6 \times 10^{-19}$ C). The term $N_Bd$ is the sheet concentration, $N_S$. Thus, by measuring $V_H$, $N_S$ could be determined:

$$N_S = \frac{IB}{q|V_H|}$$

The mobility $\mu$ could be calculated from the equation:

$$\mu = \frac{|V_H|}{R_S I B},$$

where $R_S$ is the sheet resistance of the sample. $R_S$ could be determined using Van der Pauw technique as follows [98–100]:

- A square sample is connected on its corners labelled 1-4 as shown in Figure 2.7(b).
- The resistance $R_A$ is determined by inserting a small current $I_{12}$ from 2 to 1, and measuring the voltage $V_{43}$. $R_A = V_{43}/I_{12}$. Similarly, $R_B$ could be determined using the equation $R_B = V_{14}/I_{23}$ by applying current $I_{23}$ from 3 to 2, and measuring $V_{14}$.
- The previous step could be repeated with positive and negative currents and by switching the current and voltage terminals to ensure consistency.
- $R_S$ is determined by solving Van der Pauw equation,

$$\exp\left(-\frac{\pi R_A}{R_S}\right) + \exp\left(-\frac{\pi R_B}{R_S}\right) = 1$$

- The resistivity could be then calculated from: $\rho = R_S d$, and $\sigma = 1/\rho$.
- The Hall voltage could be measured by applying a normal magnetic field and forcing a small constant current through two opposite corners (e.g. $I_{13}$ in Figure 2.7 (c)), $V_H$ is measured from the other terminals $V_{42}$. For better accuracy, the same measurement could be taken by swapping the contacts, reversing the current polarity, and applying an opposite magnetic field. The mobility and carrier concentration of the samples can then be calculated from the above equations.

In this study, electrical (Hall) measurements of the samples were performed using the ECOPIA Hall measurement system (HMS-3000) equipped with a 0.55 T magnet. The system uses the Van der Pauw technique by taking the series of above-mentioned measurements, solving the equation and returning the values of $N_S$, $N_B$, $\mu$, $\sigma$, etc. For n-type semiconductors, the majority of carriers are electrons, so a negative sign appears in the values of $N_S$ and $N_B$. Our squared samples were contacted using four gold spring pins at the corners of their surface to satisfy Pauw's condition of small contacts at the circumference. Ohmic contact was confirmed in all samples by measuring their I-V characteristics. We used electrically insulating or semi-insulating substrates to grow our samples on, to avoid any substrate contribution to the conduction. The measurements were taken in

the dark at room temperature (assumed as 300 K) and in liquid nitrogen (77 K). The repeatability of the measurements was confirmed by taking multiple measurements and re-measuring the samples after dismounting them, and sometimes after a long duration or gentle annealing.

Near the end of the project, a new four-point probe system was obtained (Ossila, model: T2001A) system. The equipment has 4 in-line pins that fall on the surface of the studied sample to easily measure its conductivity using a geometry correction factor based on the sample's shape and dimension. The system can operate around 0.2-200 mA with an accuracy of 2% for samples that have sheet resistance from 1 Ω to 100 kΩ per □, which all our samples fall within. We used this system to quickly monitor the conductivity of ZnSb films grown on Kapton after being twisted manually for up to 400 cycles (Chapter 5).

### 2.2.6 Thermoelectric measurements

Other electric and thermoelectric measurements, including temperature-dependent conductivity and Seebeck coefficient measurements, were performed by our collaborators at the University of Manchester (UK) and the University of Virginia (USA) as described in this section. The thermoelectric parameters of BiSb thin films (series MP50:55) were measured by wire bonding the gold electrodes pattern (deposited by lithography) to a dual-in-line package. This package was connected to a cryostat (JANIS) for low-temperature measurements (down to 10K). The electrical resistance was measured by the pour point probe method using the SR830 lock-in amplifier to enhance the signal-to-noise ratio. A current of 0.1 mA was introduced between the furthest electrodes (T1 and T2, in Figure 2.8(a)), and the voltage was measured from the inner electrodes (e.g. E1 and E3 for left); the resistance was averaged from both sides. For Seebeck measurements, the gold thermometers (T) on the samples were, firstly, calibrated by measuring their resistance at different temperatures. These thermometers were used, later, during Seebeck coefficient ($S$) measurements to determine the temperature gradient ($\triangle T$). When the heater is switched on with a constant current, a Seebeck voltage ($\triangle V$) could be measured across the sample between the two thermometers (T1 and T2); $S = \triangle V / \triangle T$. The Seebeck voltage was measured by Keithley 2182 nanovoltmeter, and the resistance of the heaters was measured by SR830 lock-in amplifiers to obtain $\triangle T$. Figure 2.8(b) shows the Seebeck voltage pulses when the heater is supplied by a different current and then switched off after the voltage plateaued.

For thermoelectric measurements of ZnSb thin films grown on Kapton, the elec-

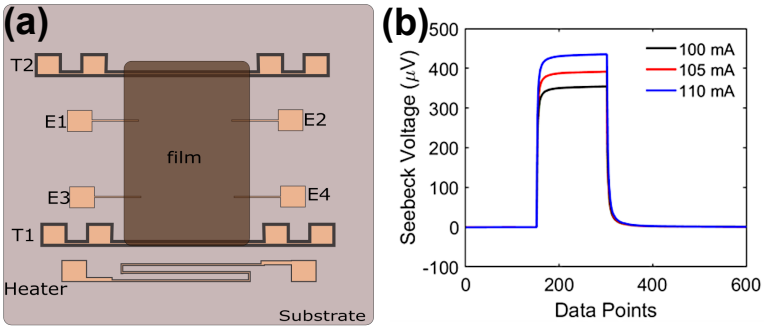


Figure 2.8: (a) Illustration of the gold electrodes configuration for thermoelectric measurements. (b) The Seebeck voltage signal when the heater was switched on and off with different current values, courtesy of Farjana Tonni.

trical conductivity and Seebeck coefficient were measured using a ULVAC ZEM3 system. Figure 2.9 illustrates the contact configuration for electrical conductivity and the Seebeck coefficient. This system also introduces a constant current from the terminals and measures the voltage drop in the middle of the sample to determine the conductivity. The sample is connected to the holder by washers and silver paste. The base temperature of the whole package is controlled inside the containing furnace. For Seebeck measurements, another heater in the bottom block creates a temperature gradient. Afterwards, the two middle thermocouples measure the temperature and voltage differences to estimate $S$.

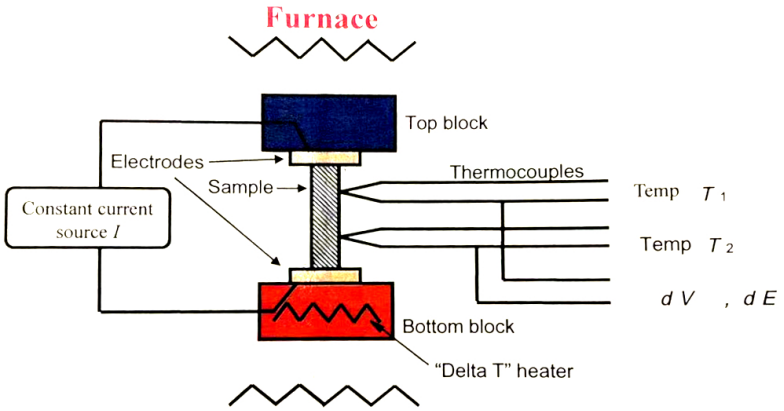


Figure 2.9: Thermoelectric measurements configuration by ZEM-3 system; the diagram is extracted from the manual.

### 2.2.7 Work Function

The work function ($\Phi$) is the minimum energy required to eject an electron from inside a metal (at Fermi level $E_F$) to a free space point just outside the metal's surface ($E_{VAC}$) at rest [101], see Figure 2.10 (a). In metals, it contains two components: the binding energy and energy required to overcome the surface dipole layers. The surface dipole is believed to arise from the "spill-out" of the electron wave functions into the vacuum, creating a negative electron layer, leaving behind a net positive charge layer from the metal's ions [101–103]. This surface dipole component is more significant in metals than semiconductors as it contains fewer free electrons [101], but it could be relatively higher in polar semiconductors like GaAs [104]. The work function is not constant for a certain material but depends on some parameters such as the crystallographic orientation and the surface adsorbates for the metals, and, the fabrication technique and the processing history of semiconductors. Besides materials-related factors, external environmental conditions can affect work function measurements such as air, contaminants and light.

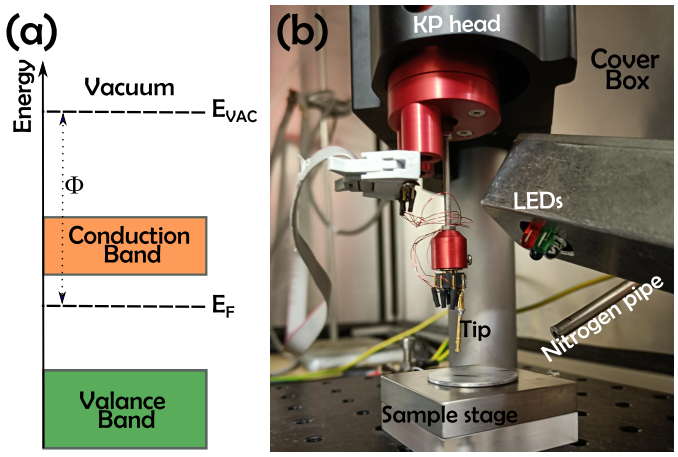


Figure 2.10: (a) Electronic energy levels of a typical semiconductor with work function ($\phi$). (b) KP equipment used to measure the CPD.

The work function could be determined by different methods such as photoemission spectroscopy (PES) and inverse-photoemission spectroscopy (IPES) techniques that can give quantitative direct measurements of different electronic band structure parameters including $E_F$, but it needs very sophisticated expensive UHV systems. Another indirect method is by measuring the contact potential difference (CPD) using the Kelvin probe method. The CPD is a potential difference that appears when two different metals contact each other as a result of an electron transfer from one to the other ($V_{CPD}$), to

align the Fermi level of both; this leaves the difference in the vacuum level of both. Kelvin probe method uses this principle to determine the work function of the studied material by the knowledge of the work function of a tip that is put very close to the surface of the studied sample. $V_{CPD} = (\Phi_{Sample} - \Phi_{Tip})/e$, where $e$ is the electronic charge. If a flat-head tip (i.e. plate) is vibrating parallel to the sample's surface, forming a vibrating capacitor, a resultant current ($i(t) = V_{CPD}\ \omega \triangle C \cos(\omega t)$) will appear between them, where $\triangle C$ is the change in capacity at angular frequency $\omega$. $V_{CPD}$ can be obtained by varying an offsetting voltage between the sample and the tip [105–107]. The advantage of this method is the high sensitivity to all the plate area, quick measurements and the ability to measure in dark, but the fundamental disadvantage is its dependence on the work function of the tip $\Phi_{Tip}$ [101, 105, 108]. Therefore, periodic calibration of the tip is required with a standard sample. Usually, material such as gold is used to calibrate the tip, but the problem is that its work function changes in the air. For example, atomically clean ordered gold under UHV has a work function of 5.0-5.1 eV, but this becomes 4.4-4.7 eV in ambient atmosphere [101]. Therefore, other easy-to-cleave material (e.g. highly ordered pyrolytic graphite (HOPG)) could be used as a standard sample to calibrate the probe. In our study, the work function of a semimetal (Sb) was determined using a Kelvin probe (KP010) system in dark under nitrogen flow to minimise air humidity (Figure 2.10 (b)). The work function of the gold tip was calibrated against a freshly prepared HOPG sample and found to be 4.67±0.08 eV.

# Chapter 3

# Chamber Building and Experimental Development

The deposition and surface science chambers used for this PhD study were either built new or modified from existing vacuum systems during the PhD project. This work was done by the author and fellow research group members. The vacuum systems are known by informal names: "Morbius" (UHV, built from scratch), "Madge" (UHV, modified), "Mercutio" (HV, modified), "Mini-Me" (HV, modified). In addition, a commercial Mantis Qube HV deposition chamber, "Moneypenny", was used. In this chapter, the technical work done and the main challenges faced are mentioned and how they were overcome. This includes the following points:

1. UHV and HV systems
    - Building UHV system 2 (Morbius)
    - Development and maintenance of other systems
    - Achieving HV and UHV
2. Homemade items built
    - Effusion cells
    - Retractable beam flux gauge
    - Masked sample plates
    - Mercutio transfer arm
3. Film flexibility test

Table 3.1: The Map of the vacuum systems used in the thesis and the author's contribution to the technical work done in each of them

| System (Nick name) | UHV system 1 (Madge) | UHV system 2 (Morbius) | HV system 3 (Mercutio) | Mantis system (Commercial system) | Test chamber (Mini-me) |
|---|---|---|---|---|---|
| Built in | 2001 | 2019 | - | .... | 2019 |
| Built by | Gavin Bell<br>Others | G. Bell (Designed)<br>I. Elhoussieny<br>T. Rehaag<br>C. Benjamin<br>Alan | Others | Mantis manufacture | G. Bell<br>I. Elhoussieny<br>T. Rehaag<br>C. Benjamin<br>Alan |
| Contribution in | Maintenance | Building and maintenance | Development and maintenance | - | Building and maintenance |
| Base pressure (mbar) | $5x10^{-10}$ | $5x10^{-10}$ | $10^{-8}$: $10^{-9}$ | $5x10^{-8}$ | $10^{-8}$ |
| Chambers | 3<br>FEC<br>MBE<br>SSC | 4<br>FEC<br>Storage<br>MBE + Pumping<br>PES | 2<br>LP-PVD<br>Main | 1 | 1<br>Test |
| Pumps attached | 3 Rotary<br>3 Turbo<br>2 Ion-pumps<br>2 TSPs | 4 Rotary<br>3 Turbo<br>3 Ion-pumps<br>2 TSPs | 2 Rotary<br>2 Turbo<br>1 Ion-pump<br>2 TSPs | 1 Rotary<br>1 Turbo | 1 Rotary<br>1 Turbo |
| Available growing elements | Sb<br>Mn<br>Sr<br>As | Sb<br>Bi<br>In<br>Mg | Sb<br>In<br>Zn<br>O | Au<br>Bi<br>Sb | Test |
| Thin film deposited in | Sb | BiSb | ZnSb | BiSb | - |
| In-situ techniques | RHEED<br>Ion Sputtering<br>STM | RHEED<br>Ion Sputtering<br>XPS<br>IPES | Ion Sputtering | Quartz Crystal Microbalance (QCM) | - |

## 3.1 UHV and HV systems

The deposition systems used have different chambers, pumps, cells and other attachments to perform different jobs. Table 3.1 shows the differences between those systems and the contribution of the author in each of them.

### 3.1.1 Building UHV system 2 (Morbius)

UHV system "Morbius" was built from scratch and developed during the PhD period. Figure 3.1 shows the developments in the system starting from 2018 with two bare chambers designed by Dr Gavin Bell and built by a professional UHV-systems manufacturer till 2022 when it is operating with all required growth and analysis capabilities. The layout of the system chambers and main techniques is illustrated in Figure 3.2, while the location of main items connected to the main chambers is illustrated in Figure 3.3. The samples are usually loaded from the fast entry chamber (FEC) and then stored in the storage chamber. For deposition, it is transferred to the MBE chamber and then

taken to the photoelectron spectroscopy chamber (PES) if the compositional analysis is required. The building process could be divided into different stages:

1. The two main chambers were raised on metal frames specially designed, connected and aligned, by the technical staff. Then, they were pumped out by connecting turbo-molecular pumps (shortened: turbo) with the rest of the flanges blanked by either windows or metal blanks after cleaning them as described in Sec. 3.1.3. The problem in this stage was leakage which required leak detection and replacing the leaky items until satisfied pressure was achieved.

2. The other chambers (FEC, storage and pumping) were connected with other pumps, gauges, transfer arms and manipulators after testing each of them individually (2019 image in Figure 3.1). The pressure reached the UHV region after degassing the transfer arms. Mechanical problems like supporting and securing heavy items, and mismatching between different elements (e.g. a spacer required between flanges or imperial bolts needed for special connections) were common in this stage. In addition, the long transfer arm's end between chambers was not present, which required collaboration with the technical team to build and install a new homemade one.

3. The effusion cells, ion guns and reflection high-energy electron diffraction (RHEED) gun were tested in the testing chamber (Mini-me) (with the homemade beam flux gauge (Sec. 3.2)) to select the best-performing pieces. These items were installed and degassed gently in Morbius after filling the effusion cells with the elements required. Externally, the water manifold was installed to cool down the cells and system, and the gas manifold was installed to provide the system with the required gases (e.g. Ar bottle was connected to the ion gun). The cells were degassed again at higher temperatures and calibrated. One problem arose during that period, the antimony cell's shutter became stuck during the calibration. The shutter was discovered to have a huge Sb bulb deposited on it that prevented it from opening. It happened because of the wrong temperature reading, as the C-type thermocouple was connected to the common K-type reader, which means that the actual temperature was about 2.4 times higher than the read one. The cell's shutter was then disassembled, cleaned, raised higher and mounted again to prevent this from happening again. The cell's flux was then calibrated against its current and voltage instead of temperature. The conversion curve from the wrong read to the actual temperature was plotted and left by the equipment to give a sense of how much the real temperature is.

4. In this stage, the Ar sputtering gun and RHEED gun were tested with a standard GaAs substrate, and the first sample was grown. Also, the x-ray photoelectron spectroscopy (XPS) and IPES equipment were mounted. The X-ray source was then degassed and the sample's position was optimised to collect higher signals. During this period, we were practising growing samples, analysing them with RHEED and XPS and looking for the optimised conditions.

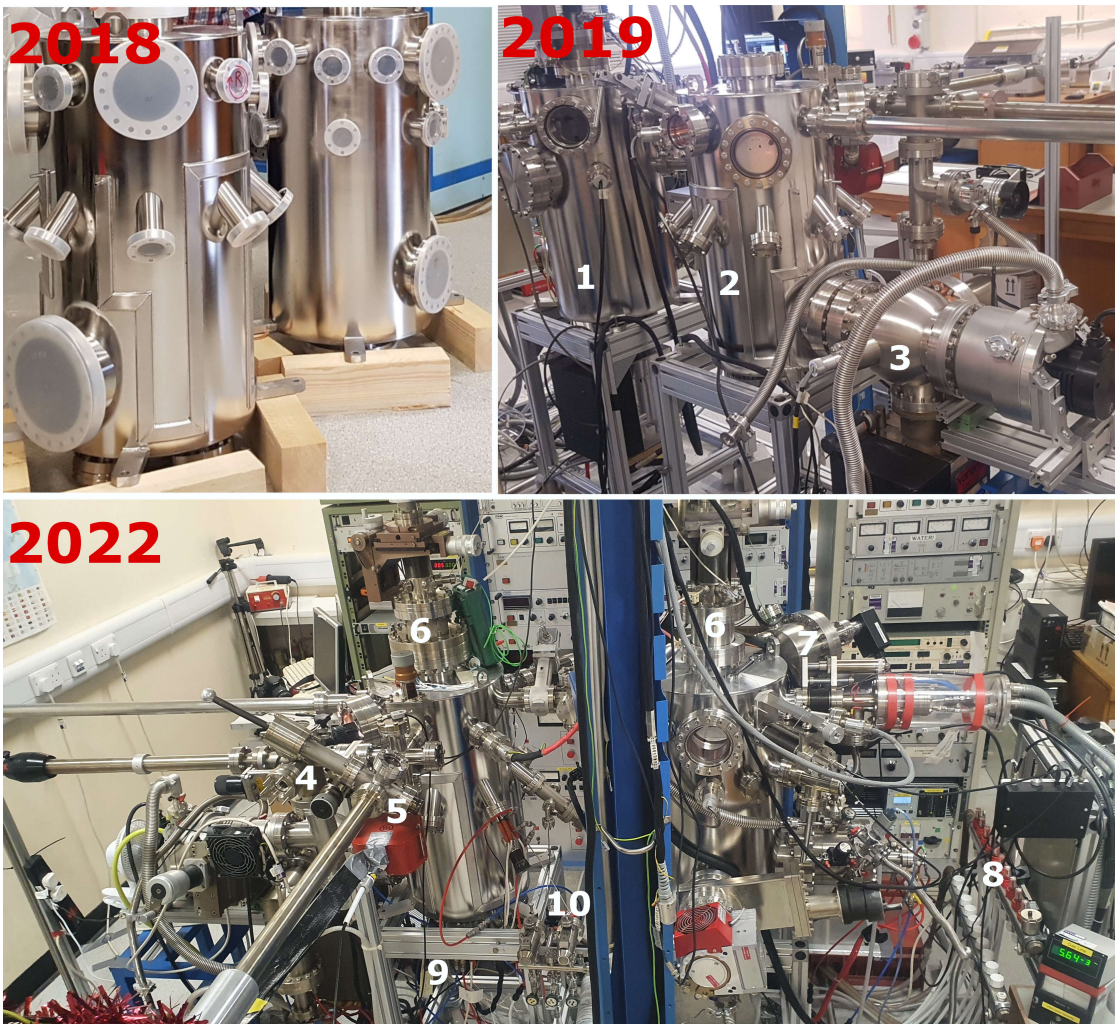


Figure 3.1: The timeline shows the development of the UHV system 2 (Morbius) from 2018 to 2022. The numbers refer to 1: PES chamber, 2: MBE chamber, 3: pumping chamber, 4: FEC chamber, 5: storage chamber, 6: manipulators, 7: XPS detector, 8: water manifold, 9: effusion cells, and 10: gas manifold.

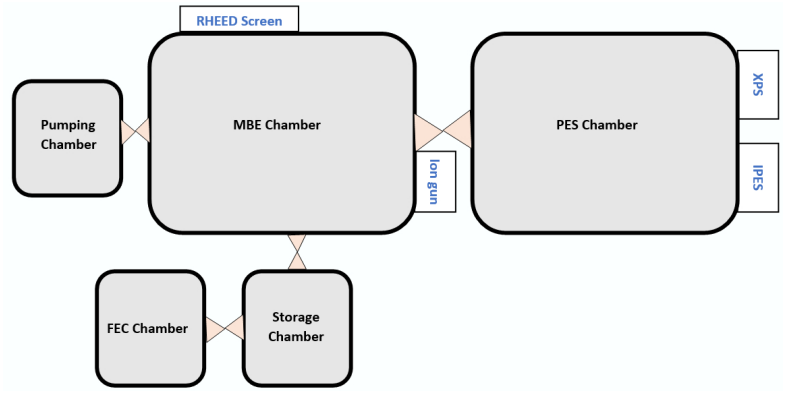


Figure 3.2: The layout of Morbius UHV system and the positions of the attached in-situ analysis equipment.

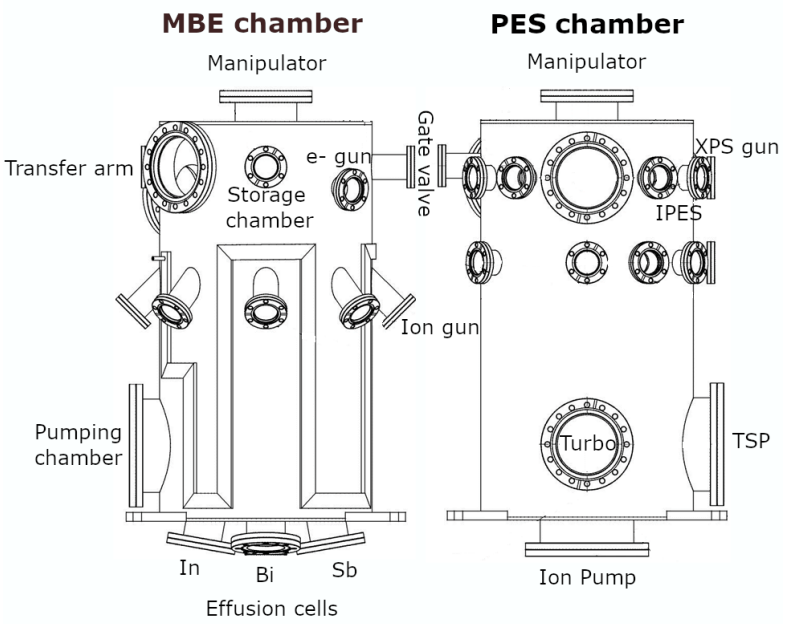


Figure 3.3: Side view of Morbius main chambers (MBE and PES) and where the main items were connected. The drawings were modified from the manufacturer's data sheets.

### 3.1.2 Other systems

As we grow different elements that have different properties, some of them may be incompatible with others. For example, zinc vapour has a long "memory effect" in HV systems, i.e. a strong Zn partial pressure is permanently established after Zn effusion, contaminating other elements and reducing the base pressure of the system. The prob-

lematic low sticking coefficient of Zn on different substrates during growth experiments was reported earlier and was overcome by raising the substrate's temperature above RT [109, 110], increasing the Zn flux [63] or by introducing nitrogen plasma [111]. Therefore, ZnSb is required to be deposited in another system (Mercutio) apart from other UHV MBE growth systems.

**UHV system 1 (Madge)**

Madge is a UHV MBE system that was used for growing Sb thin films during the Morbius-building period. It has three chambers: (1) FEC, (2) the MBE chamber with X-Y-Z-$\phi$ manipulator, (RHEED) and Sb, Mn and Sr effusion cells and (3) the surface science chamber (SSC) which is equipped with an ion gun and scanning tunnelling microscope (STM) (see Figure 3.5). In addition to the typical UHV maintenance, a range of maintenance operations was performed including:

- Repairing a leakage in the body of the SSC chamber using spray epoxy after leak checking.
- Fixing a broken manipulator's Ta wire heater filament in the MBE chamber (shown in the inset of Figure 3.5).
- Preparing STM tips. The STM stage was replaced once before as well.
- Degassing a coated window that was covered with Sb after one baking event as mentioned in Sec. 3.1.3.

After every venting event, we degas and calibrate all the used effusion cells to ensure they will give the same required flux in the growth and to estimate the thickness and composition of the grown films correctly. This includes a plot of the beam flux pressure against the filament current or the crucible temperature. The equivalent beam pressure $P$ is related to the absolute temperature $T$ by the Clausius-Clapeyron equation [112] as follows (original papers in German and French 1850,1843):

$$P = Ae^{-\frac{\triangle H}{RT}}$$

where A is constant, $\triangle H$ is the enthalpy of sublimation or evaporation, and $R$ is the molar gas constant. $P$ is the beam flux pressure minus the background pressure, ideally measured using a shielded ion gauge at the sample position. The plot of $\ln(P)$ versus

$1/T$ determines the enthalpy of Sb sublimation (See Figure 3.4).

$$\ln P = \ln A - \triangle H/RT$$

The value of the determined $\triangle H$ (170 kJ mol$^{-1}$) from our Sb cell calibration is in reasonable agreement with the reported value in the literature (195 kJ mol$^{-1}$) [113]. The discrepancy may arise from a difference between the measured cell temperature (a thermocouple at the base of the crucible) and the temperature of the top of the Sb charge, from which the material is sublimating.

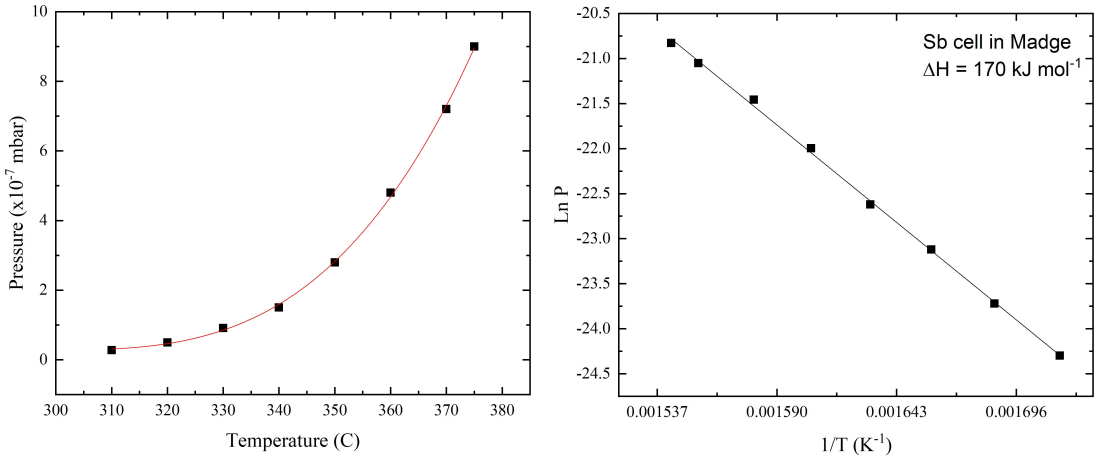


Figure 3.4: The calibration curves of Sb effusion cell on UHV system 1 (Madge).

### HV system 3 (Mercutio)

Mercutio (Figure 3.6) is an HV system, which was used to prepare ZnSb samples. Mercutio has two chambers; the side chamber has Zn, Sb and In effusion cells with a CF-100 Viton door on the top that is used to load the samples on a transfer arm. This arm is used to hold the sample and transfer it to the second (main) chamber which is always kept under a high vacuum with $Ar^+$ sputtering option. This chamber has a window on the top, through which an IR lamp could be used to degas samples before the deposition. As a side, this chamber was used to do ion-patterning for some InP substrates. The system required a great deal of technical development work such as:

- Indium and Antimony cells were built, and the transfer arm was developed as mentioned in Sec. 3.2.

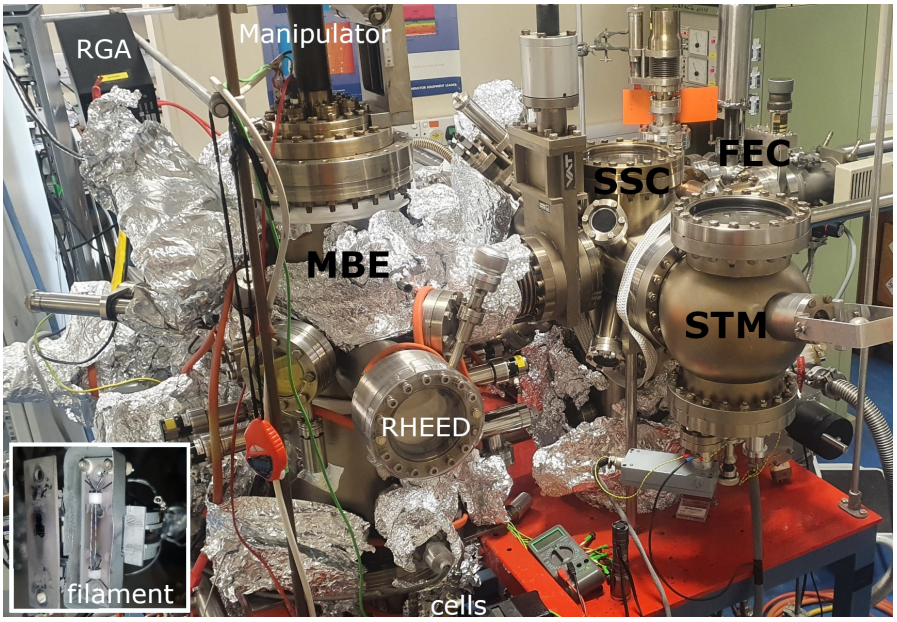


Figure 3.5: Image of UHV system 1 (Madge) with its three chambers FEC, SSC and MBE. The inset shows the manipulator's sample stage when its filament was once fixed.

- One experiment was done to know the temperature of the sample when being degassed and heated by irradiation using an infrared lamp. This was done by connecting a thermocouple to a sample plate that was put in the sample's degassing site. The temperature was then taken versus time in a high vacuum to mimic the real situation, and to avoid cooling by air convection (see the inset in Figure 3.6). The plate's temperature was found to reach 130°C after 10 minutes of switching the lamp on and 220°C after 20 min then remains constant.

- A similar experiment was performed to select the optimum $Ar^+$ sputtering conditions (Ar pressure and sample's position) by measuring the Ar ions current in a vacuum. The optimum location was marked on the transfer arm for the following experiments. For pressure optimisation, Figure 3.7 shows the Ar-ions current per $cm^2$ for different pressure values (a) with the AFM image of one typical sputtered InP substrate at the optimised conditions (b).

- Regular system baking and effusion cells degassing and refilling as samples are loaded from the side chamber where the cells are located.

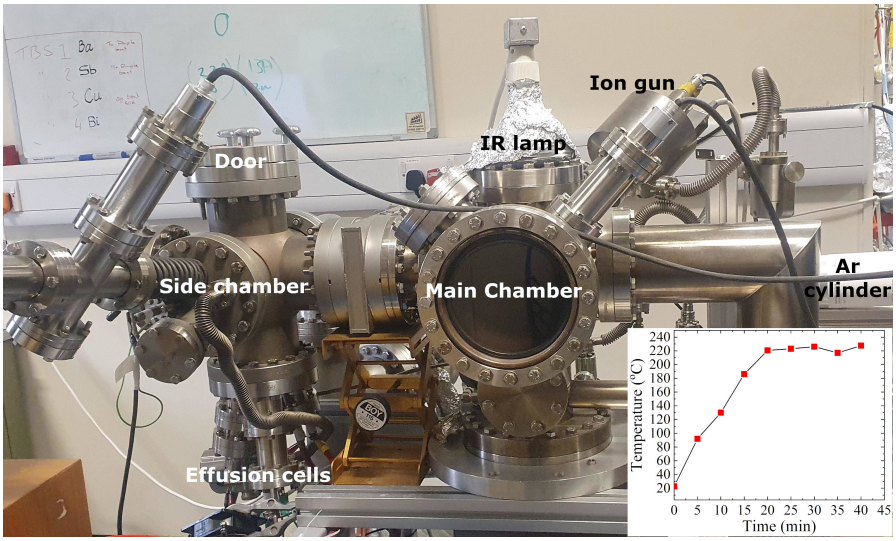


Figure 3.6: HV system 3 (Mercutio). The inset shows the temperature of a sample when irradiated by the IR lamp inside the chamber.

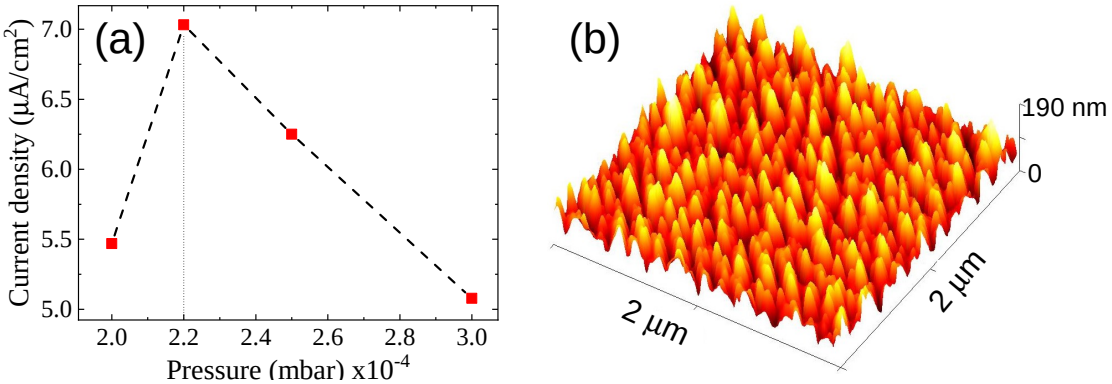


Figure 3.7: Panel (a) Ar ion current density dependence on its pressure inside Mercutio. Panel (b) AFM topograph of a typical Ar-sputtered InP substrate.

### 3.1.3 Achieving HV and UHV

#### Cleaning UHV components

HV and UHV systems include components that are made of compatible materials (e.g. stainless steel, copper, tantalum, tungsten and ceramics), which have low outgassing in the vacuum. This improves pressure stability in the UHV range. Many components included in our chamber builds had been stored for many years in ambient atmosphere and the prior history was often unknown. So before installing any of these, it went under

a deep cleaning protocol as follows:

1. Wiping with isopropyl alcohol (IPA) wetted tissues to remove any apparent stains. Sometimes, using acetone or scrapping with Brasso is required with heavy stained parts, but this needs special attention as some materials corrode with these chemicals such as Viton with acetone.

2. Use an ultrasonic bath of diluted Micro-90 (or commercial cleaning agent for use with ultrasonic cleaners like IPA or acetone) for some minutes. This is followed by rinsing with fresh IPA.

3. Blowing with nitrogen then baking in the oven in the air at around 150 $^{o}$C for more than 1 hour to thoroughly dry that part.

After cleaning any of the UHV parts, they are installed by inserting a new Cu gasket between two conflat (CF) flanges and then fixing it using bolts, washers and nuts of suitable size. This metal-to-metal seal is essential for minimizing any potential leakage for HV and above and allows baking. In low-vacuum regions such as rotary pump pipes, Klein flange (KF) sealing is used with rubber rings instead. Besides, some heavy equipment like chambers, turbomolecular and ion pumps needs supporting bars and frames to minimize any forces on the seal. This prevents future leaks and increases the lifetime of the flanges and the chamber welds supporting them.

**Pressure-related problems**

Maintaining the pressure is crucial in HV and UHV systems. Unfortunately, pressure instabilities are usually observed, and these require immediate response to sustain a healthy vacuum system. There are different possible reasons for the pressure increase:

1. Heating a sample or a filament inside the chamber will spontaneously increase the pressure for some time then it will return to its normal due to degassing the hot part. In this case, no action is required if the pressure does not increase considerably (orders of magnitude).

2. The presence of leakage from one of the UHV components, usually from delicate parts like flexible bellows or feed-throughs. The pressure may increase by some orders of magnitude which requires leak checking. If the pressure is in the range of $10^{-5} : 10^{-7}$ mbar, alcohol can be sprayed around different suspected areas until observing an abrupt rise in the pressure. But within $10^{-7} : 10^{-9}$ mbar, Helium leak

checking is used by connecting dedicated equipment that contains vacuum pumps and a He detector (mass spectrometer) and spraying the He gas around the items of the system. After identifying the leaky part, it could be either replaced by another one or repaired with a high vacuum sealant (epoxy or spray). This sealant fills the leaky holes and blocks any air from passing through after being cured (usually after a period of time or by gentle annealing).

3. The presence of water vapour and atmospheric gases after venting the system or being at a low vacuum for a long time results in a poor vacuum. Equally, contamination with high vapour material can cause continuous outgassing that reduces the overall vacuum. This contamination could be a result of depositing many materials inside the chamber. In those cases, the system needs to be baked as described in the following section.

4. Failure of a vacuum pump affects the total pressure of the system, especially if it is the backing mechanical pump. Rotary pumps, for example, need periodic maintenance such as exchanging the lubricating oil or baking the foreline trap. A turbo pump, with poor backing pressure, spends more load power which warms it up and leads it to be tripped out. That problem increases the system pressure to the low vacuum region, and more severely, may damage the ion pump, ion gauges, and any other operating filaments or cells.

Besides the above-mentioned points, any of the pressure gauges may be broken or gives wrong readings. We regularly solve these issues with different types of gauges. The Pirani gauge is a wire resistor that gets hotter with less air around (i.e. low pressure) and becomes more resistant, fixing it is as simple as welding a broken wire. The ion gauge head (Figure 3.8) has a more complex structure; it has a cylindrical cage ("grid"), two filaments and a simple hair-wire in the middle ("collector"). After years of usage, one of these elements gets broken. Replacement grids are available if a gauge head has been damaged, but the most common replacement is the filaments. Tungsten wire spirals (12 - 14 turns) wound by hand can be spot-welded onto the filament frame fairly easily.

### Baking-related problems

Baking the vacuum system is one of the most efficient ways to reduce the pressure value orders of magnitude and improve the cleanliness of the system. During this process, the system is put under high temperature for a long time, enough to degas previously absorbed elements or water vapour, while the system is under vacuum. We consider some

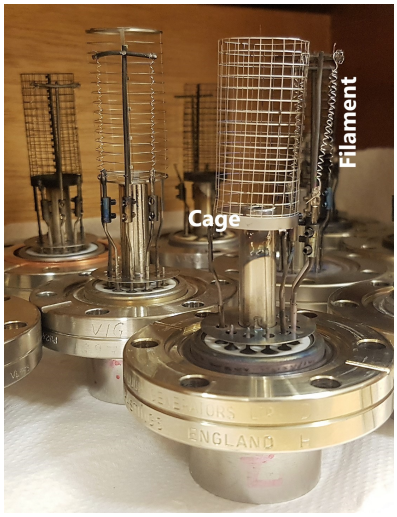


Figure 3.8: An ion gauge head.

precautions when baking a system to avoid any possible fire or damage to the system such as:

1. Before baking, all non-bakeable items must be disconnected such as electrical connections, water pipes and plastic and magnetized parts.

2. The heating tapes are tested and then wrapped evenly across the whole system, considering using low-temperature heater cables (40 W / m) with sensitive areas like transfer arms and STM.

3. Thermocouples are distributed over main spots to monitor the temperature and to be connected to thermo-controllers.

4. The system is then covered with aluminium foil to keep the uniform temperature distribution inside the chamber as shown in Figure 3.9.

5. The heating tapes are switched on carefully one by one while testing the bake-out controller.

6. During the baking, pressure and temperature values are reported along with gaseous contents detected by the residual gas analyser (RGA). Those values are to be compared before and after baking to evaluate the efficiency of the baking process. Figure 3.10 shows the RGA spectrum before and after one baking event of Madge. After baking, the partial pressure of detected gas molecules went down and the

$H_2O$ (at 18 amu) to $N_2$ (at 28 amu) ratio became smaller which represents effective baking.

Figure 3.9: UHV chamber Madge during bakeout. The system is wrapped with heating tapes, and covered by aluminium foil.

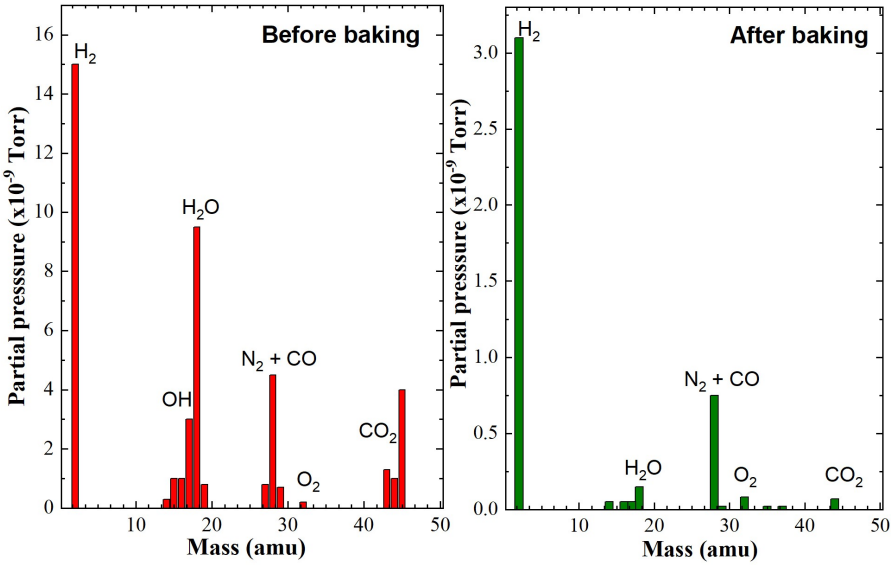


Figure 3.10: Mass spectrum of MBE chamber on Madge before and after baking. Bars are labelled by their corresponding gas molecules at different atomic masses. Note the difference in vertical scale between baked and unbaked.

Some unexpected troubles may appear after baking though. For instance, the

system may become too hot that the previously deposited elements on walls sublimate and cover everything inside the system including windows. When this once happened in Madge, an infrared lamp was used for one week to sublimate that coating from windows. Other problems could be a leak or damage to some components.

## 3.2 Homemade items

The construction and maintenance of our vacuum systems required a lot of UHV items to be installed. This does not only encourage the repairing of some broken items but also the building of some new homemade ones. Some of these items are (made mainly by the author):

1. Effusion cells
2. Retractable beam flux gauge
3. Masked sample plates
4. Mercutio transfer arm (developed)

**Homemade cells**

Homemade effusion cells for In and Sb were built for ZnSb-In film growth in Mercutio. Those cells required different components to be made of. Figure 3.11 shows the In cell, as an example, which was built from some items such as:

1. CF flange with four feed-throughs, two of them to connect the filament and two for the thermocouple.
2. Copper wires, thermocouple wires, supporting rods and threading, small-size bolts, washers, nuts, and electrical connectors.
3. Suitable-size crucible and different insulating ceramic pieces.
4. Spiral filament wire (Ta for example).

During building the cell, special attention was considered to separate and isolate the filament wires from the thermocouple ones from the ground using different ceramic pieces. For example, the thermocouple wires (5) are separated from each other by a cylindrical ceramic piece with two holes (6) and fixed under the crucible (7) to avoid any contact with the filament or the frame. It is important as well to connect each

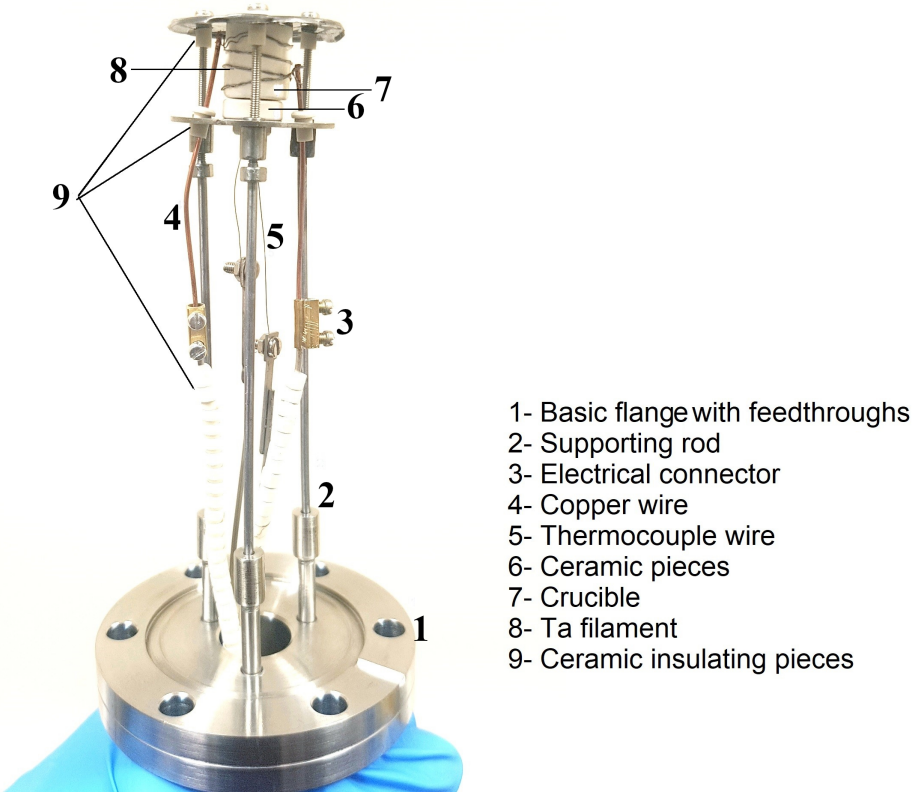


Figure 3.11: Homemade effusion cell used for indium.

thermocouple leg to the feedthrough made of the same alloy to get accurate temperature readings, (Nickel-Chromium / Nickel-Alumel) for K-type.

### Retractable beam flux gauge

The pressure inside HV and UHV systems is often measured by ion gauges. It contains a filament that emits thermionic electrons when it is heated up. These electrons get accelerated towards a positively charged cage and ionize the gas molecules in its surrounding. The gas-positive ions are then collected by a thin wire in the centre of the cage called the collector. This current is proportional to the number of ions, that is converted into pressure using an external electronic controller. Similar in its function to the ion gauge, the beam flux gauge (BFG) is used to measure the flux pressure of elements to be deposited. It needs additional parts to travel to the sample location for accurate flux measurements.

To measure the Bi and Sb flux inside Morbius, one BFG was built using ion gauge

components, supporting rods, a Ta shielding sheet and a Z-shifter as shown in Figure 3.12. The ion gauge head was mounted to the Z-shifter by solid supporting rods. Wires connecting each filament were selected to be of highly conductive material like copper to avoid any potential voltage drop across it that gives wrong pressure readings. A shielding foil was added to ensure that the pressure reading comes from the cells (at the bottom) and not from the background. It has another role in protecting the substrate (in the manipulator) above it from the cell fluxes during the pressure stabilization period.

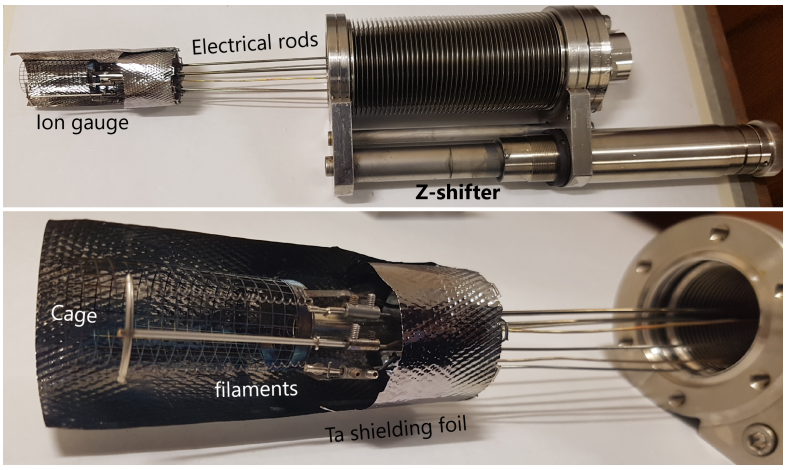


Figure 3.12: Homemade retractable beam flux gauge.

### Masked sample plates

The preparation of BiSb films for thermometric measurements required designing devices from three layers: an InP substrate, a BiSb thin film and gold electrodes. For consistent measurements, all the samples have to have the same layers' design and dimensions (e.g. the substrate should be 8mm by 8 mm to fit in the cryostat sample holder). The BiSb film, as a second layer, must be located in a specific place on the substrate to allow the third layer (gold electrodes) to be positioned correctly. This requires mask growth for both layers. We had two options to mask growing these films. The first one is to prepare it using a lithography technique which requires having a pre-deposited mask of photoresist material on the substrate. But this layer could be destroyed while preparing the substrate's surface either by degassing at a high temperature (around 350°C) or during the ion-sputtering process. The second option was to design a physical metal mask that covers the rest of the substrate during the BiSb growth. The second option was more convenient for the BiSb layer, plus it consumes less time and effort. The mask

was made of a tantalum sheet as it is UHV-compatible material and it can endure high temperatures as well. The design of the masks was developed as follows (see Figure 3.13):

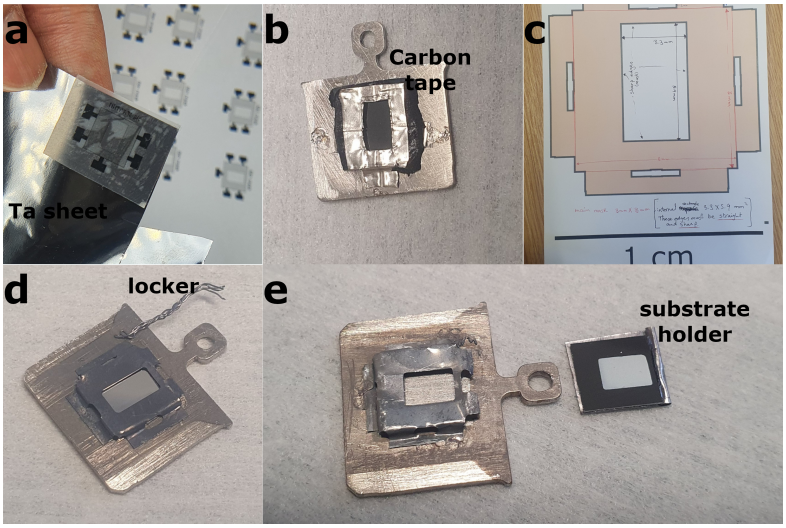


Figure 3.13: The development of the BiSb mask design. Panels (a) and (b) show the design of the first prototype. Panels (c) and (d) show the new design and CNC machine-cut mask with a locker to secure the sample. Panel (e) shows the final used plate after replacing the locker with a Ta piece to prevent the substrate from moving.

1. The first prototype was made by designing the mask using Inkscape software. It was then printed on white adhesive tape and taped on a piece of Ta sheet. It was then cut manually by a scissor and a razor blade and then was spot welded on a flat sample plate (a,b). The problem with that design is that the sample was loose, to fix it carbon tape was used. But this limited the degassing temperature so we had to remove it. The second problem is that the internal rectangular shape, where the film is supposed to be deposited, was not as sharp as required.

2. In the second trial, the design was modified, printed and sent to the mechanical workshop, where it was cut by CNC machine (c, d). The sample was also secured using winded Ta wires (as a locker). When this design was used, the sample was not totally fixed in place, especially when the sample was rotated during the growth. This was noticed from the large gradient at the film's edge.

3. The last design (e) has the modified film dimensions cut by the mechanical workshop. In addition, the locker was replaced by another Ta piece (as a cushion) to

fix the substrate firmly and fill the gap underneath. This masked plate design was used for the BiSb TE samples.

To deposit the gold layer, the lithography option was selected as the gold electrodes have very fine dimensions that do not suit the metal mask.

### Mercutio transfer arm

Heating the Zn cell in Mercutio builds a considerable amount of Zn vapour inside the growth (side) chamber (Figure 3.14). This vapour takes some time to be pumped out, during which it can contaminate the samples' surface with extra Zn particles and hence changes its composition. To overcome this problem, the samples used to be transferred to the main clean chamber and kept inside before and after the deposition. In addition, the transfer arm was developed by installing two circular metal disks on it to block the tube between the two chambers and minimize the amount of vapour that moves to the main chamber. After installation, the pressure inside the main chamber after the growth became about one-third of the side chamber's pressure with the gate open and disks between the chambers. Figure 3.14 shows Mercutio with the disks located in the tube between the chambers installed on the transfer arm.

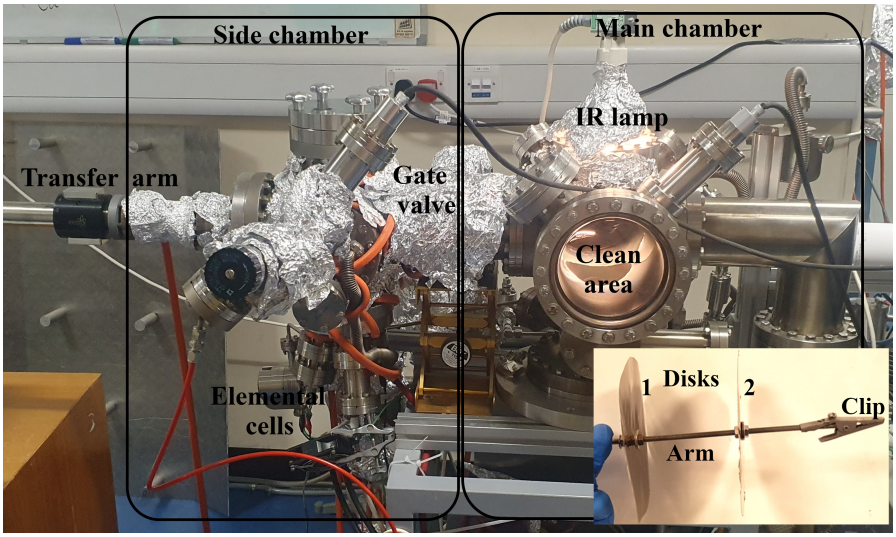


Figure 3.14: Mercutio chambers when the transfer arm is extended to keep the sample clean in the main chamber. The disks are positioned in the gate valve location. The inset shows the transfer arm with the two disks installed on it and a crocodile clip to hold the sample holder.

## 3.3 Film flexibility test

Different mechanical testing techniques have been developed to assess the resilience of the investigated flexible component under bending circumstances [114]. The most frequent and basic of these tests is the static bending test, which involves bending the flexible sample over a rod with a certain diameter [114, 115]. However, this approach is not enough for actual working environments, where frequent bending is crucial [116]. Despite not providing a constant radius of curvature, push-to-flex bending is one of the most used dynamic bending techniques [114, 117, 118]. In this thesis, some ZnSb thin films were grown on Kapton flexible substrates to study their robustness as a possible wearable device. The durability of such films was examined by testing their electrical and optical properties before and after bending the films many times (thousands of cycles). For

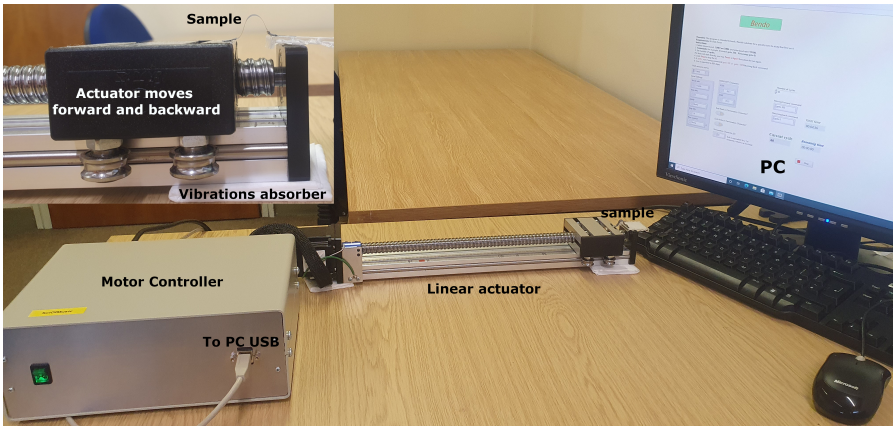


Figure 3.15: The film flexibility experiment consists of a linear actuator controlled by a control unit that is connected to a computer via a USB cable. The inset shows a zoomed-in test sample during the bending cycle.

that purpose, a push-to-flex bending experiment (Figure 3.15) was set up to bend the films repetitively using a linear actuator, a control unit and a LabView application. The control unit, which was already built for another purpose, contains a 24 V power supply and Arduino Due plugged into a stepper card type IHM02A1. The external control of the motion was done by an application created by the author using LabView software. Firstly, a "serial write and read" LabView example was used to make serial communication with the Arduino Due chip. Secondly, a loop of two commands was adjusted to give the forward and backward motion with the preferred travel distance (e.g. 400 steps $\approx$ 0.5 cm) and the appropriate time delay between cycles. Thirdly, the graphical user interface (GUI, Figure 3.16) was developed to include the instructions to run the program (Section

1) and to display the total and remaining time and the current cycle (Section 3), to make it easy for the user to follow the process. Finally, the application was tested with 300 cycles up to 20000 cycles; about 1 mm drift was observed. This might cause the actuator to collide with the end part, so a plastic safety piece was fixed (mildly by double-sided tape) to separate them more and avoid any collision. In addition, the whole device was lifted by a small stack of soft tissues to absorb vibrations from the desk and minimize noise.

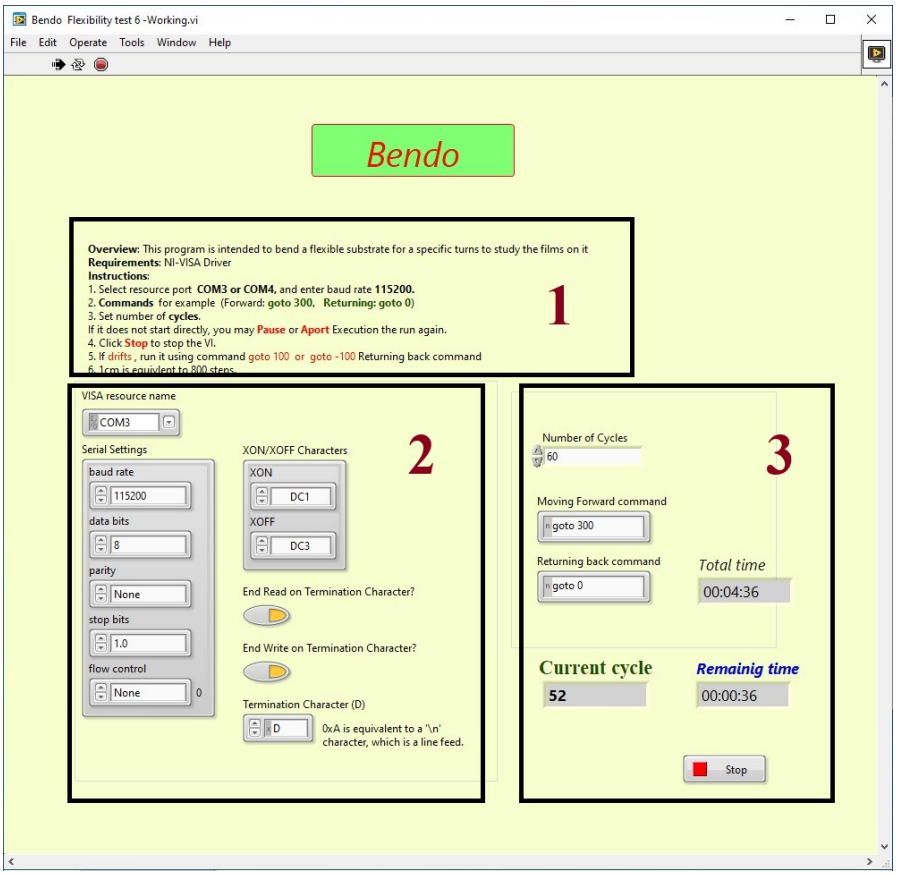


Figure 3.16: The GUI of the LabView application (used in flexing ZnSb films grown on Kapton) contains 3 sections. Section 1 contains the instructions to use the program. Section 2 reads the serial port communication parameters (from the LabView example). Section 3 is the control and monitoring section that reads the moving commands and the number of cycles, and shows the progress of the experiment.

# Chapter 4

# BiSb Thin Films

Topological insulators (TI) (eg. BiSb) have a narrow gap in their bulk. However, they have a metallic-like surface with topologically protected gapless states [119, 120]. Fundamental symmetries of these states (e.g. time-reversal symmetry) mean that they are unaffected by non-magnetic impurities [121]. This leads to suppressed backscattering and hence high surface conductance [122]. The ideal case of a topological insulator with a completely insulating interior does not exist because of the presence of residual bulk carriers which contribute to the conduction [11]. To minimise this contribution by means of increasing the surface-to-volume ratio, nano-structuring is often used [11]. This is important for investigating the topological-metal conductivity of BiSb films, as the contribution of surface states to the total conductivity of a material cannot be accurately determined by using bulk crystals [123]. This could be done by preparing ultra-thin membranes or nano-ribbons, but these have limited practicality for device manufacturing. For $Bi_{1-x}Sb_x$ (the electronic configuration and phase are discussed in appendix A), thin film nano-structuring can also extend the presence of surface states when ($0.22 < x < 0.35$) beyond the bulk TI regions due to the quantum size effect that creates an external band gap and clearly defines the boundary with the semi-metallic region [124]. Gunes et al. [125] concluded that compared to the bulk $Bi_{1-x}Sb_x$ sample, where ($0 \leqslant x \leqslant 0.22$), ball-milled nanostructured samples have broader semiconducting composition areas ($0 \leqslant x \leqslant 0.5$). Another approach is to increase the surface-to-bulk ratio by introducing many holes in bulk BiSb samples which can improve the thermoelectric figure of merit ($ZT$) because of two factors: (1) the contribution of the surface states to the conductance and (2) the suppression of phonon thermal conductivity [126]. Whether these holes are periodic or not, the phonons' thermal conductivity will be minimised by their strong capture in that random system [126]. Similar nano-structuring could be done

by depositing thin films (of an appropriate thickness, say 100 nm) on nanostructured (or patterned) substrates, where the morphological instability hinders the heat conduction, but the enlarged topologically protected surface states keep the electrical conduction high. Different groups have investigated nano-structuring the surface of some substrates, such as InP and GaSb by ion-beam sputtering at different angles and energies [127–130].

In this chapter, we compare the properties of $Bi_{77}Sb_{23}$ thin films grown on normal flat surface InP(001) substrates (denoted by F) and those grown on Ar-sputtered nano-patterned InP substrates (denoted by P). Firstly, we investigated the growth, structure, morphology and electrical Hall measurements of the films for samples grown in the MBE UHV system 2 (Morbius) in Sections 4.2 and 4.3. Secondly, we discussed the thermoelectric properties (i.e., conductance and Seebeck coefficient) of BiSb 3-layer devices grown in the Mantis PVD system and the lithography suite in Section 4.4. Table 4.1 summarises the samples investigated and the techniques used for their preparation and characterisation. To calculate the average thickness and some electrical parameters, certain considerations were discussed (see Section 4.1).

Table 4.1: List of BiSb samples discussed in this chapter and the techniques used for their characterisation.

| Sample | Substrate surface | Deposition system | Structure | Morphology | Thickness | Composition |
|---|---|---|---|---|---|---|
| **IBS11F** | Flat | UHV system 2 (**Morbius**) | XRD | AFM and SEM | AFM | EDX |
| **IBS11P** | patterned | | | | - | |
| **IBS12F** | Flat | | | | AFM | |
| **IBS12P** | patterned | | | | - | |
| **Test** | patterned | No deposition | - | AFM | | - |
| **MP50** | Flat | **Mantis** thin films deposition system and the lithography suite | - | AFM | AFM | EDX |
| **MP51** | patterned | | | | - | - |
| **MP52** | | | | | | |
| **MP53** | | | | | | |
| **MP54** | | | | | | |
| **MP55** | | | | | | |

## 4.1 Analysis

We assume that two films are grown simultaneously in the same experiment on square substrates of side $L$. One is deposited on a flat substrate (denoted by $f$), while the other is grown on a patterned surface (denoted by $p$). The same volume of material $V$ is

deposited on each substrate for a given growth cycle, where

$$V = A_f d_f = A_p d_p$$

and the $A_{f,p}$ and the $d_{f,p}$ are the films' surface areas and thicknesses respectively. This is illustrated in figure 4.1. The flat film's surface area is identical to the substrate area, i.e. $A_f = L^2$. Because the patterned surface has a 3D structure, its surface area is bigger than the equivalent flat one ($A_f$). We define the surface-to-projection ratio (SR) as:

$$\mathrm{SR} = \frac{A_p}{A_f} = \frac{d_f}{d_p} \geq 1$$

which could readily be determined by, for example, AFM. We assume that the geometry of the patterning does not involve much area of surface at steep angles relative to the average surface plane and is spatially uniform, but otherwise specify no details about the topography. If the thickness of a conformal film is comparable to the vertical scale of the patterning or surface roughness, the SR of the film's surface will be very close to the substrate's SR value. As the film thickness increases, the film surface may become smoother than the underlying pattern (depending on the growth mode) and in such a case SR could be considered as the average value between the film (top, SR measured after growth) and the substrate (bottom, SR measured before growth). In all cases, the average film thickness on the patterned substrate will be smaller than that on the flat substrate since $d_p = d_f/\mathrm{SR}$. We assume that the material resistivity $\rho$ and bulk carrier concentration $n$ are not affected by the non-planar growth. With sheet resistances $R_{f,p}$ and sheet carrier concentrations $N_{f,p}$, this means that $\rho = R_f d_f = R_p d_p$ and $n = N_f/d_f = N_p/d_p$

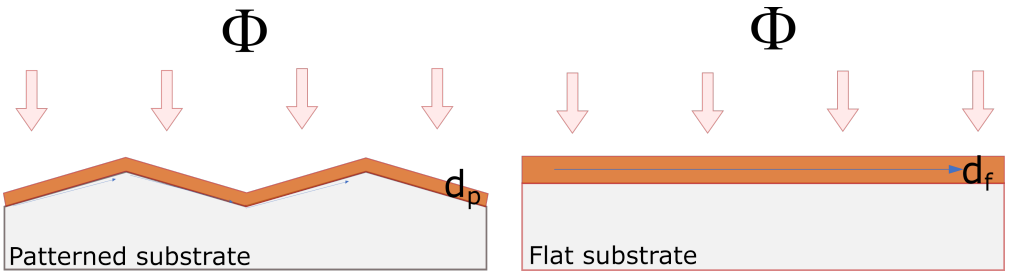


Figure 4.1: Illustration of films (orange) grown simultaneously on flat and patterned substrates (grey). Vertical arrows represent incoming growth flux and, in Hall measurement, magnetic flux; these are identical for both samples.

A van der Pauw measurement of sheet resistance [98–100] involves measuring a

conductor using four ohmic contacts on its surface. For a square sample, the contacts are best placed at the corners. By measuring with all combinations of contacts and both field orientations, errors due to differing contact resistances, thermoelectric offset voltages and shape discrepancies can be minimised. However, for a non-planar film with morphology as described above, several parameters will change compared to the flat film case. According to the assumptions given above, we expect that $R_p = \mathrm{SR}\, R_f$ and that $N_p = N_f \,/\, \mathrm{SR}$.

For Hall measurement, a perpendicular magnetic field is also applied. On a non-planar film, the carrier path may be more complicated than assumed in a standard Hall effect calculation since the field lines intersect the film at a range of non-perpendicular angles. A simple approach is to note that the same magnetic flux $\phi = B_f\, A_f = B_p\, A_p$ passes through the flat and patterned samples, so that the average flux density is reduced on the non-planar film owing to its increased effective area and $B_p = B_f \,/\, \mathrm{SR}$. The Hall voltages $V_{f,p}$ are given by

$$V_{f,p} = \frac{I B_{f,p}}{q\, n\, d_{f,p}}$$

where $q$ is the electronic charge. Under the above assumptions, $V_f = V_p = V_H$ since the factors of SR cancel in the effective field and effective thickness for the non-planar film. The mobilities $\mu$ are given by

$$\mu_{f,p} = \frac{|V_H|}{R_{f,p}\, I\, B_{f,p}} = \frac{1}{q\, n\, d_{f,p}\, R_{f,p}}$$

In this case,

$$\mu_p = \mathrm{SR} \times \mu_f \tag{4.1}$$

## 4.2 BiSb sample preparation

### 4.2.1 InP substrate nano-patterning

To increase SR, semi-insulating InP substrates were heavily bombarded by accelerated $Ar^+$ ions inside the HV system 3 (Mercutio). The substrates were degassed inside the chamber using an IR lamp for about 15 minutes to reach a temperature of around 200 °C (as described in Chapter 3). After degassing, the $Ar^+$ sputtering was started for 30 minutes at a pressure of $(2.5 \pm 0.5) \times 10^{-4}$ mbar at energy of $(2.6 \pm 0.2)$ keV. The position of the substrates was chosen to collect the maximum number of Ar ions, giving

a current of $(6.6 \pm 1.2)\mu$ A/cm$^2$. The spreading resistance was measured before and after the patterning process to ensure that the samples remained insulating. One patterned substrate was scanned using the AFM before and after annealing it for 1 hour at 300 °C and then at 400 °C and 500 °C, to study the effect of thermal annealing on the patterned surface and to determine the highest temperature the samples could endure without destroying the pattern. In the UHV system 2 (Morbius), all the flat and the patterned substrates were prepared by two cycles of gentle Ar sputtering (at the pressure of $5 \times 10^{-6}$ mbar and energy of 0.5 keV at 300 °C for 20 min) to remove any oxide layers. This was followed by 30 minutes of annealing at 400 °C to recrystallise the surface of the substrates without destroying the nano-patterning (see Section 4.3.3). This is surface cleaning which does not significantly affect surface morphology.

### 4.2.2 BiSb Film deposition

The BiSb films were prepared in the UHV system 2 (Morbius) with a base pressure less than $1 \times 10^{-9}$ mbar. Two separate effusion cells were supplied with 6N grade elemental Bi and Sb. The Sb and Bi flux pressures were adjusted to be $3 \times 10^{-8}$ mbar and $1.4 \times 10^{-7}$ mbar respectively to form a composition around $Bi_{0.8}Sb_{0.2}$. To achieve high-quality growth, the substrates were maintained at 320°C during the growth and the samples were rotated 360° manually to ensure uniform crystalline samples. Previous reports have shown that increasing the Sb ratio to 32% can degrade the quality of $Bi_{1-x}Sb_x$ films grown on Si(111)that was observed by the disappearance of the RHEED pattern [123, 131]. This can be mitigated by increasing the substrate temperature, as reported by Ueda et al. that temperatures of 200-250°C are required for the epitaxial growth of these films [124]. The surface cleaning also promoted high-quality growth by removing the InP surface oxide.

## 4.3 Characterisation

### 4.3.1 XRD

XRD was used to investigate the crystalline structure of BiSb films. The GIXRD geometry was used at the beginning, but we found that the diffraction patterns exhibit strong texture. Therefore, we switched to the Bragg-Brentano geometry ($\theta - 2\theta$) to evaluate the texture coefficient values. Figure 4.2 shows the presence of distinct XRD diffraction peaks of the investigated films, suggesting that the films are crystalline. The peak positions showed good agreement with the powder diffraction card (PDF 04-023-9518) of

$Bi_{0.8}Sb_{0.2}$ that have rhombohedral structure (space group: R-3m). However, the difference in relative intensities between our experimental data and the PDF card reflects the presence of a strong preferred orientation towards certain planes, such as (003) and (012). To determine the ratio between both, the texture coefficient TC($\gamma$) was calculated. The presence of other peaks in some samples shows that the films- especially those grown on patterned surfaces- contain a polycrystalline portion. This portion was calculated from the (104) peak only as it is the closest high-intensity peak to the (003) and (012) peaks. Note that the diffracted beam comes from the BiSb film and the InP substrate underneath. When $2\theta$ increases, the film's contribution decreases compared to the substrate.

The texture analysis shows that films grown on flat InP substrates have higher textural purity than those grown on patterned ones. Table 4.2 shows the texture coefficient of each of the investigated samples and their corresponding percentage. In general, BiSb films grown on flat InP substrates have $98-99\%$ of the (003) texture, while those grown on the nano-patterned ones have $88-92\%$ of the (012) texture with $6-10\%$ of (003) texture plus the polycrystalline portion that reaches 2%. Similar textural dependency on the surface of the substrate was found by Chi et al. [132], where stoichiometric BiSb crystals tended to orient in (003) or (012) planes or stay random when deposited on various seed layers. The transition between the two textures also could occur by controlling the preparation conditions. For example, epitaxial $Bi_{1-x}Sb_x$ films on Si(111) change from (003) to (012) when Sb concentrations exceed 8–9% at room temperature [131]. The Sb percentage in our samples exceeds this ratio (23%), that (012) oriented films were expected. Siegal et al. annealed the as-prepared $Bi_{0.8}Sb_{0.2}$ films up to 295 °C to increase the ratio of (003) to (012) grains and improve the crystallinity of the specimen to $\sim 99\%$ [133]. Our initial substrate temperature was slightly higher (320°C), which likely changes the (012) texture to the (003) texture in the flat samples. However, this high temperature was not enough to reorder the rough structure of the BiSb films that were grown on the patterned substrates. In other words, the substrate surface can stop a predicted texture transition from happening under certain circumstances.

**RHEED**

In an earlier experiment, the growth of BiSb films on InP substrates was studied using the in situ RHEED technique. Figure 4.3 shows RHEED patterns of one flat and one patterned InP substrates before and after the growth of the BiSb films. Panels (a,b) represent the 4-fold symmetry patterns along the [001] and [011] directions of the flat InP

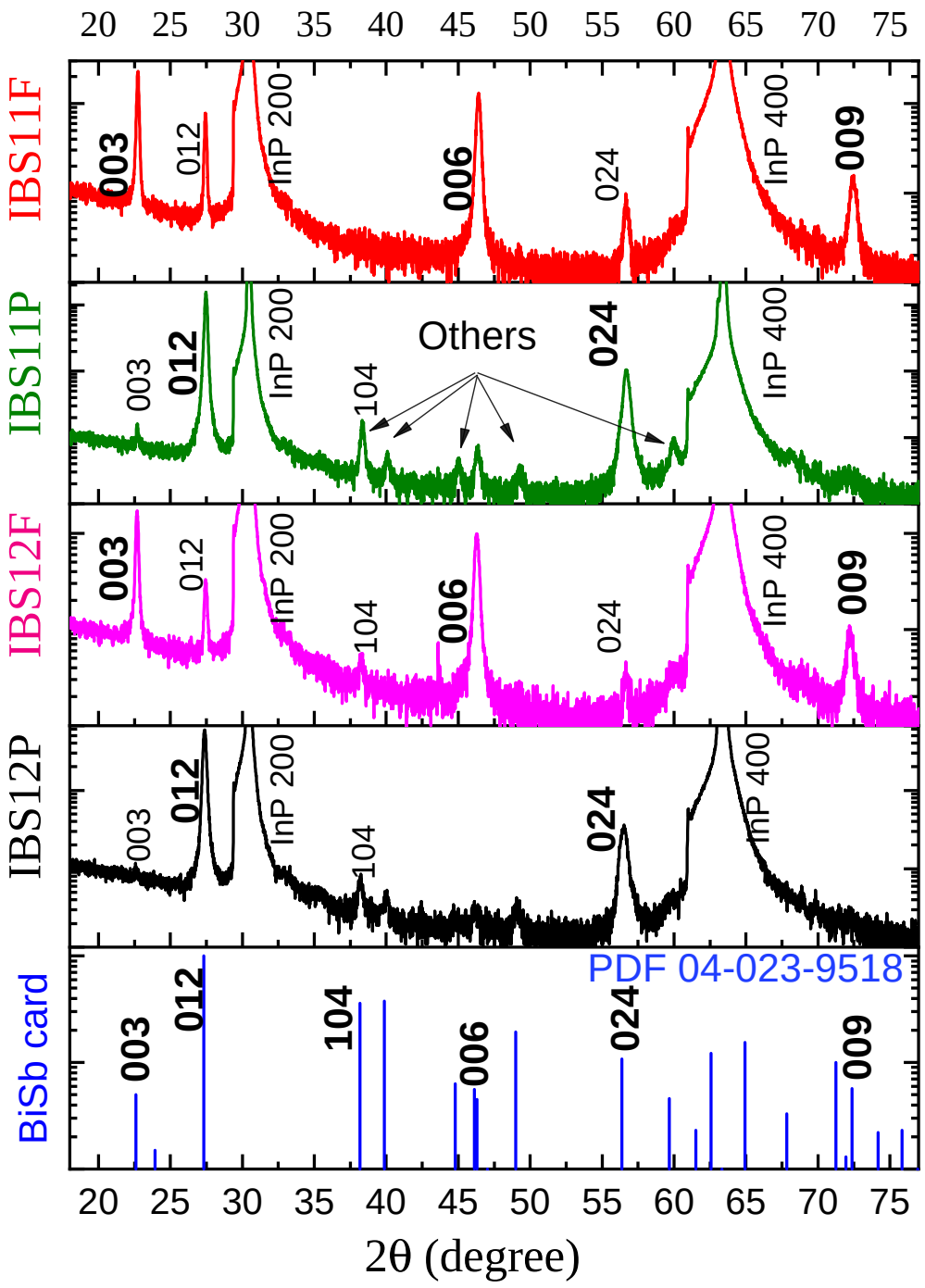


Figure 4.2: XRD diffraction pattern of the four studied BiSb samples the with $Bi_{0.8}Sb_{0.2}$ (PDF 04-023-9518) card [82]. The y-axis is a log scale scaled to maximise the BiSb peaks in all the panels. Selected peaks are labelled to show the preferred orientation in each film, the dominant direction peaks are bold.

(100) substrate. Kikuchi lines can be seen in the patterns with no intermediate surface diffraction streaks (contrast to bulk Kikuchi), which shows that the surface is highly ordered and has the same bulk symmetry with no surface reconstruction. Panel (c) shows the pattern of the patterned InP substrate, which has powder diffraction rings and some spots indicating the 3D nature of the surface. This means also that the patterning process has likely amorphised the surface of the substrate, but it was partially recrystallised by the annealing process. In the middle row, panels (d,e) show the BiSb film grown on a flat InP substrate. This film shows a dominant 6-fold rotational symmetry with no Kikuchi lines, different from the 4-fold symmetry seen in the substrate (epitaxial mismatch). The non-sharp streaks nature suggests the possibility of having a small amount of other textures. This has been confirmed through XRD analysis, which shows that the films whose substrates are flat are (003)-oriented. This plane contains two symmetry directions (i.e. 100 and $1\bar{1}0$) with a 30-degree angle between them. Moreover, the InP substrate 011 patterns (e.g. panel (b)) meet with either of the BiSb symmetry directions every 90 degrees. In addition, at one angle (Panel (f)), the streaks are split (with an angle $2\theta = 14°$), which indicates the presence of some facets 7°-tilted from the horizontal level.

The analysis of the RHEED patterns of the BiSb film grown on the patterned InP substrate was more complex: the film contains more than one crystallographic orientation that causes distinct patterns to appear at various angles. In the bottom row of Figure 4.3, the BiSb film grown on the patterned InP substrate is presented. In general, a 6-fold rotational symmetry feature (panels g and h) was observed overlapping with a 4-fold symmetry feature every 90 degrees. These are believed to belong to the (003) and (012) textures because the (003) plane has 6-fold rotational symmetry and the (012) plane has 4-fold-like rotational symmetry. Two of the opposite overlapped patterns showed a faceted feature (panel (i)) with an average angle of 19 degrees with the horizontal plane, which is higher than the tilt in the flat sample (angle of 7 degrees). This is logical, as the films on the patterned substrate are rougher than those grown on the flat one. In panels (g) and (h), the pattern is formed of spotty dots, not streaks, which is associated with transmission diffraction since the patterned samples have 3D surfaces. Panels (h) and (i) have clear powder diffraction rings that indicate the presence of a polycrystalline portion of the film on the surface. In summary, RHEED analysis confirms that the film grown on the patterned InP substrate has a higher ratio of different phases and a polycrystalline portion, and has a rougher surface. This is consistent with the conclusions deduced from the texture analysis of the XRD patterns.

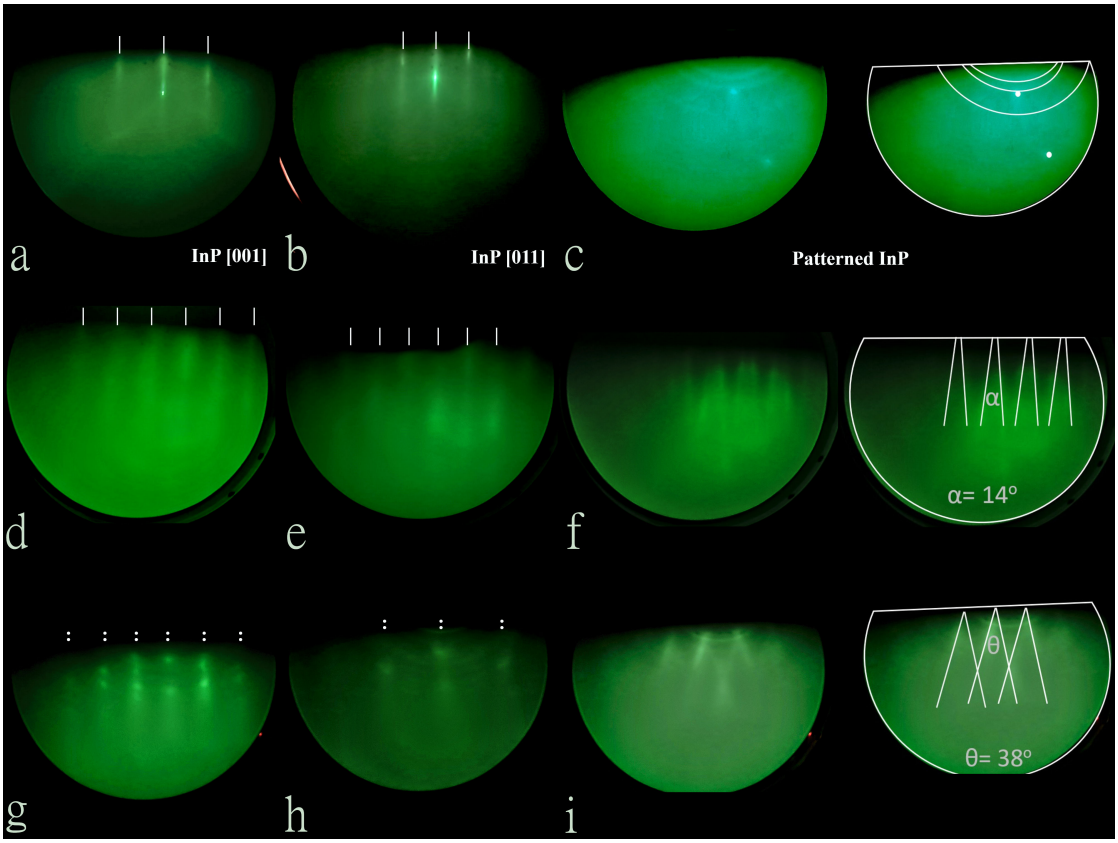


Figure 4.3: RHEED patterns of the InP substrates and the BiSb films grown on them. Panels (a) and (b) are of the flat InP (100) substrate. Panel (c) is the patterned InP substrate. Panels (d), (e) and (f) show the BiSb film grown on a flat InP substrate. Panels (g), (h) and (i) are of the BiSb film grown on a patterned InP substrate.

### 4.3.2 SEM and EDX

The prepared BiSb films were silver with a noticeable difference in "mirror finish" between the flat and patterned samples due to the change in their light-scattering properties (see Figure 1.8(a)). The SEM images show a clear difference in the topography between the two types and confirm the patterning of P-samples. Figure 4.4 shows the SEM images of the prepared films at $10^4$ magnification with 7 kV acceleration voltage for all samples. Flat samples (on the left side) have more uniform topography with larger particle sizes than those of the patterned substrates (on the right side). Similarly, thicker films at the top (i.e. IBS11F and IBS11P) have less rough surfaces with larger particles and uniform topography. EDX analysis reveals the homogeneity of all the studied samples. The composition of each sample was determined at three positions across its diagonal,

showing less than 1 at% difference in the composition. Table 4.3 shows the composition of the films determined by EDX for all four samples. Samples grown in the same growth have nearly the same composition, with less than 1 at% difference, reflecting the compositional uniformity of the grown films. Moreover, the composition in both growths was close, with an average of 22.6 at% Sb and a standard deviation of 1.4 at%.

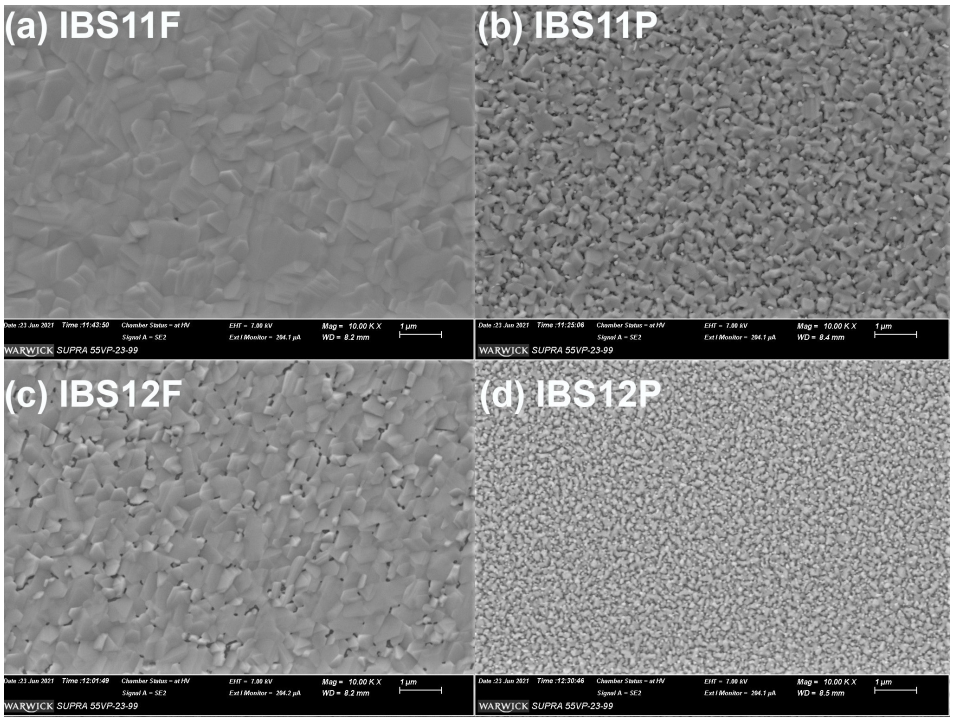


Figure 4.4: SEM images of BiSb samples grown on flat and nano-patterned InP substrates. Images were captured by SUPRA55VP SEM at 7kV accelerating voltage and $10^4$ magnification.

### 4.3.3 AFM

Patterning of the InP substrates was confirmed by the AFM, as shown in Figure 4.5. The roughness of the patterned substrates (i.e. IBS11P and IBS12P) was determined to be 36 nm and 30 nm respectively. Both substrates contain a dense array of irregular nano-ripples with a depth of around 100 nm. Previous work at Warwick showed that Ar ion bombardment of InP (100) above 1 keV produces irregular surfaces. In our samples, this is not a problem since the main purpose of the patterning is to increase the surface area, not necessarily periodically. This increase in area was evaluated by dividing the substrate surface by its projection (surface ratio, SR=$\frac{surface}{projection}$) using Gwyddion software

as explained in Chapter 2. It is worth noting that the substrate's surface area was nearly doubled by the patterning, with SR $= 2.1 \pm 0.1$ for both substrates. To keep this value and preserve the patterning, the temperature of the samples was kept around or below 400 °C before and during the film deposition. Our previous experiment showed that after 1 hour of annealing at 500 °C, the patterning has altered and the SR value fell from 1.7 to 1.2, as shown in Figure 4.7. Figure 4.7 illustrates the effect of annealing at different temperatures for 1 hour on the pattern of one typical InP substrate. For 1$\mu$m images, the surface area of the pattern remained around 1.7 $\mu m^2$ when annealed up to 400 °C. After one hour of annealing at 500°C, the pattern altered completely and the surface area dropped to 1.2 $\mu m^2$.

The thickness of the films was determined (in each growth from a separate flat piece) and reported with other AFM parameters (roughness and SR values) in Table 4.3. Figure 4.6 shows 3D images of the surfaces of BiSb films scanned by the AFM. Films that were grown on flat substrates (at the left) have three-fold symmetry features (i.e. triangles and 120-degree angles). In contrast, "P" films have rougher surfaces, especially the thinner film (IBS12P) which nearly has the same surface morphology as the substrate does. As the film thickness increases, the surface becomes smoother and has a smaller SR value (1.28 for IBS11P compared to 1.59 for IBS12P) and the features of the BiSb symmetry film become more dominant instead.

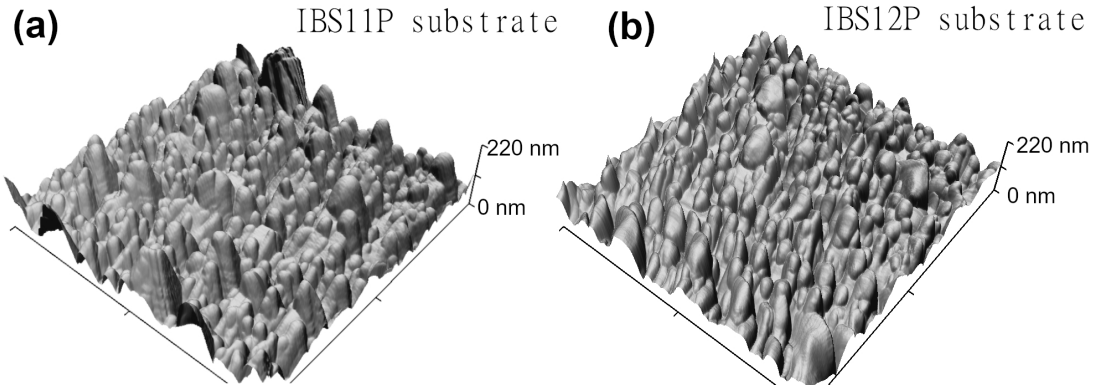


Figure 4.5: AFM topographs of the patterned InP substrates (1$\mu$m $\times$1$\mu$m). Panel (a): IBS11P substrate and (b): IBS12P substrate.

### 4.3.4 Hall measurements

The flat InP substrate is electrically insulating, and no current was detected when it was measured by our Hall system, down to 1nA (i.e. the resistance is greater than 1 $\times$

Table 4.2: The texture coefficient TC(hkl) in the investigated samples. The percentage (%) of the (003), (012) and "others" phases is calculated by normalising the texture coefficients.

| Sample | TC (003) | TC(012) | TC(others) | % (003) | % (012) | % others |
|---|---|---|---|---|---|---|
| IBS11 F | 1.96 | 0.04 | - | 98.06 | 1.94 | 0.00 |
| IBS11 P | 0.29 | 2.64 | 0.07 | 9.78 | 87.99 | 2.23 |
| IBS12 F | 2.97 | 0.03 | 0.01 | 98.95 | 0.84 | 0.21 |
| IBS12 P | 0.17 | 2.77 | 0.05 | 5.73 | 92.45 | 1.82 |

Table 4.3: The composition of the BiSb films as determined by EDX and the film structural parameters. SR values were determined using the Gwyddion software for the patterned substrates and all films. The thickness here is measured in each growth from a third flat sample using the AFM.

| **Sample** | **IBS11 F** | **IBS11 P** | **IBS12 F** | **IBS12 P** |
|---|---|---|---|---|
| Sb (at%) | 24.0 | 23.6 | 21.8 | 21.1 |
| Bi (at%) | 76.0 | 76.4 | 78.2 | 78.9 |
| Thickness (nm) | 121 | 121 | 70 | 70 |
| RMS roughness (nm) | 19 | 29 | 14 | 31 |
| SR(substrate) | - | 2.13 | - | 2.08 |
| SR(film) | 1.03 | 1.28 | 1.05 | 1.59 |
| SR(average) | - | 1.71 | - | 1.84 |

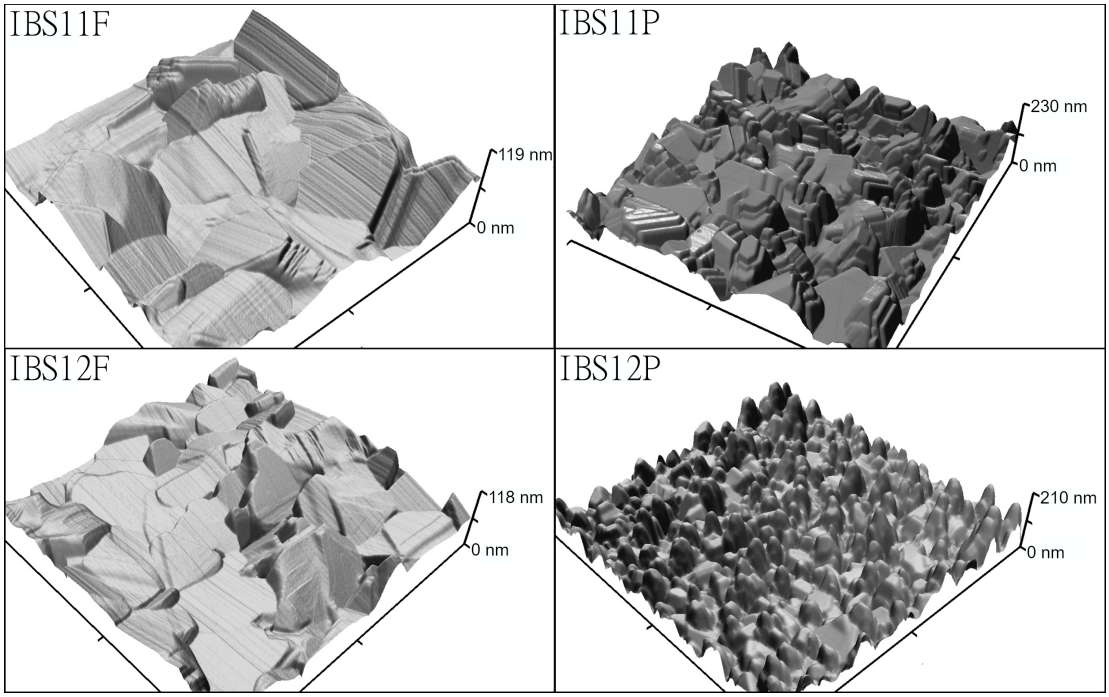


Figure 4.6: AFM images of the surfaces of BiSb films (2$\mu$m $\times$2$\mu$m) of the investigated samples.

$10^{10}\Omega$). After the patterning process, the spreading resistance was very high but became measurable ($\approx 3\times10^{7}\Omega$), meaning the possibility of having an extremely thin conductive In-rich layer on the surface. But this does not affect the electrical measurements because the resistance of the BiSb films is four orders of magnitude lower.

To explain the electrical parameters, the BiSb films could be treated as bulk semiconductors with a metallic surface. In this case, the total conductivity of BiSb could be expressed as [134, 135]:

$$\sigma = \sigma_s(\frac{d_s}{d}) + \sigma_{Bo}\ \exp(-\frac{E_g}{2k_BT}),$$

where $\sigma_s$ is the surface conductivity, $d_s$ is the effective surface thickness, $\sigma_{Bo}$ is a constant, $E_g$ is the electrical band gap and $k_B$ is the Boltzmann constant. The first term in the equation represents the surface contribution to the conductivity, while the second term represents the bulk conductivity. Accordingly, the surface conduction becomes dominant in two cases: (1) if the film thickness is low, which increases the first term. It may increase the effective $E_g$ at very low $d$ due to quantum confinement that reduces the bulk conductivity. (2) if the temperature (T) is very low, the second term of the equation

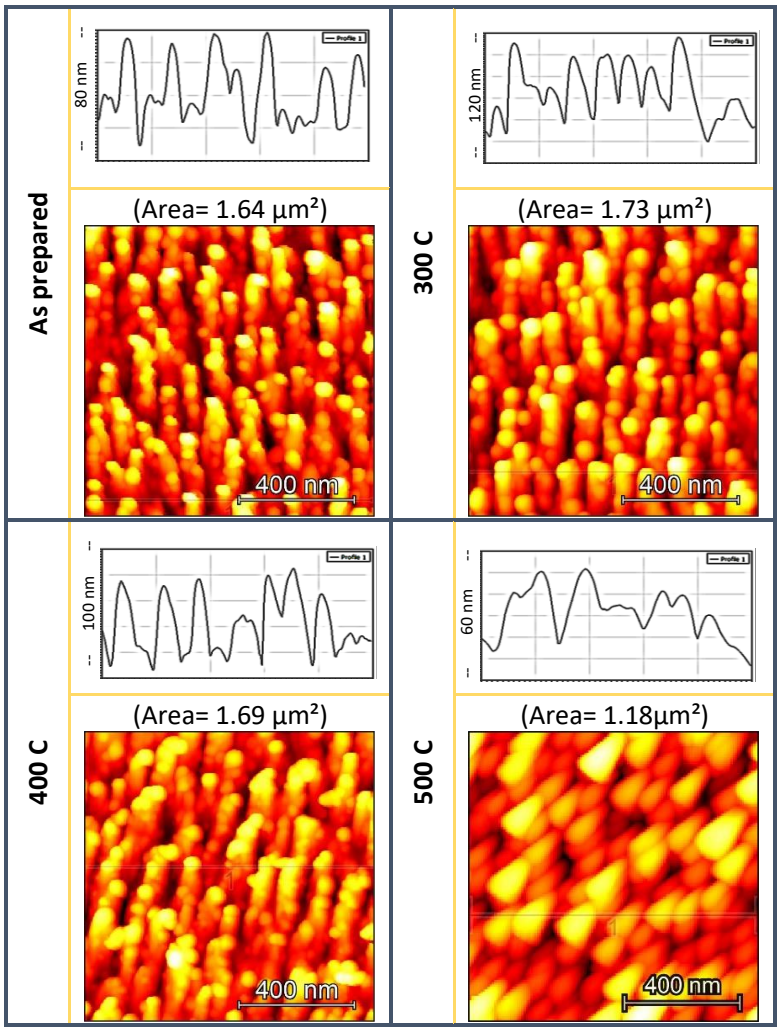


Figure 4.7: 1$\mu$m×1$\mu$m AFM topographs of a patterned InP substrate as-prepared, after 1 hour of annealing at 300 °C followed by another hour at 400 °C and at 500 °C. Representative line profiles are included for each topograph.

will be reduced, and the surface conduction dominates. To separate both conductivity components and determine the equation parameters, the electrical conductivity of films of different thicknesses over a wide range of temperatures could be used [124, 131, 135]. In this Section, we analyze the electrical parameters derived from Hall measurements (using the Van der Pauw technique) at room temperature (300 K) and under liquid nitrogen as described in Chapter 2. While the temperature-dependent conductivity data is discussed in Section 4.4.3. Therefore, conductivity $\sigma$, here, is the 'total' conductivity, as do the other derived electronic parameters (e.g. $\mu$ and $N_s$).

In general, the type of InP substrate (flat or patterned) and the thickness of the film significantly impact the electrical parameters, owing to the different structures and thicknesses. Table 4.4 shows the corrected parameters (thickness, carrier concentration, mobility and conductivity) of the prepared films, calculated based on the equations in Section 4.1. The negative sign of the bulk carrier concentration values ($N_B$) shows majority n-type conduction.

At room temperature, different-thickness F-films have close $N_B$ values around $7.8 \times 10^{19}$ $cm^{-3}$, likewise, P-films of different thickness have values around $2.8 \times 10^{19}$ $cm^{-3}$. This indicates two points: (1) both films behave as semiconductors, where the bulk conduction is dominant over the surface conduction because at high temperatures the bulk semiconducting interior gets enough carriers activated to dominate. (2) F-films (i.e. 003 BiSb) have more carriers than P-films [mostly (012)]. To compare, BiSb films with less Sb percentage (0.12 to 0.16) were reported to have smaller carrier concentrations but higher mobility than ours. For example, Ueda et al. reported that the carrier concentration of (003)-oriented $Bi_{84}Sb_{16}$ was $2 \times 10^{19}$ $cm^{-3}$ and the mobility was 500 $cm^2/Vs$ at room temperature [136]. In another article, the carrier concentration of ball-milled $Bi_{88}Sb_{12}$ increased from $1 \times 10^{18}$ $cm^{-3}$ at 50 K to $1 \times 10^{19}$ $cm^{-3}$ at 300 K, while the mobility decreased from $15 \times 10^3$ $cm^2/Vs$ to $2.3 \times 10^3$ $cm^2/Vs$ [137].

This thickness-independent carrier concentration was not observed at 77 K. In this temperature range, the $N_B$ values are higher for thinner films, suggesting a strong contribution from the metallic surface states. In addition, $N_S$ values are close for different thicknesses, around $2 \times 10^{14}$ $cm^{-2}$ for F-films and $4 \times 10^{13}$ $cm^{-2}$ for P-films. This suggests that the metallic surface conduction is dominant and the bulk contribution is minimal at this low temperature.

The conductivity for the flat samples and the thick patterned sample ($\geq$ 70 nm, at 300 K) exceeds $10^3$ $\Omega^{-1}cm^{-1}$ near the values of MBE grown (003) oriented $Bi_{1-x}Sb_x$ films on GaAs(111) [124]. For (012) oriented ball-milled $Bi_{77}Sb_{23}$ samples, the conductivity was measured as $2.65 \times 10^3$ $\Omega^{-1}$ $cm^{-1}$ [125].

The conductivity values increase with the "corrected" thickness for all samples because thinner films have larger confinement (high $E_g$) for carriers' movement which reduces its mobility. As with low dimensionality, spatial confinement displaces the band gap edges and converts semimetals like Bi to semiconductors [138, 139].

Samples IBS11P and IBS12F are good examples to understand the effect of the patterning only, as both have an equivalent (corrected) thickness of 70 nm, but the first has 1.7 times more surface area. On one hand, both samples have similar conductivity values (around 1525 $\Omega^{-1}$ $cm^{-1}$ at 300K and 550 $\Omega^{-1}$ $cm^{-1}$ at 77K). Therefore, the lower

conductivity observed in the patterned samples might be compensated by depositing corrected thickness equivalent to the flat ones. But on the other hand, the patterned sample (IBS11P, (012) BiSb) has a smaller number of carriers with higher mobility. This could have resulted from two opposite conduction mechanisms. The first one is that the patterned samples have more protected surface states, where the mobility in these states is higher than that of bulk states. Consequently, more conduction occurs from the surface states, with fewer carriers of high mobility. In contrast, the flat sample has more ordered (003) semiconducting bulk which has higher conductivity than its surface states, so a high number of bulk carriers contributes to the conduction, but with lower mobility than those of the surface states. Walker et al. found that when BiSb thin films are orientated in the (012) direction instead of the (003) direction, the temperature-dependent conductivity of the films decreases, most likely, as a result of changes in the surface states and the quantum confinement [131].

Table 4.4: Electrical Hall measurements of the prepared samples using the corrected values for the patterned films.

| Sample | T(K) | d(nm) | $N_B(10^{19}\mathbf{cm}^{-3})$ | $\mu(\mathbf{cm}^2/\mathbf{VS})$ | $N_S(10^{14}\mathbf{cm}^{-2})$ | $\sigma(\Omega^{-1}\mathbf{cm}^{-1})$ |
|---|---|---|---|---|---|---|
| IBS11F | 300 | 121 | -8.0 | 217 | -9.7 | 2792 |
| IBS11P | 300 | 71 | -2.7 | 349 | -1.9 | 1501 |
| IBS12F | 300 | 70 | -7.5 | 130 | -5.2 | 1552 |
| IBS12P | 300 | 38 | -2.8 | 22 | -1.1 | 100 |
| IBS11F | 77 | 121 | -1.6 | 305 | -1.9 | 763 |
| IBS11P | 77 | 71 | -0.53 | 682 | -0.37 | 577 |
| IBS12F | 77 | 70 | -3.2 | 102 | -2.2 | 524 |
| IBS12P | 77 | 38 | -1.1 | 35 | -0.42 | 63 |

## 4.4 Thermoelectric measurements

### 4.4.1 Device optimisation

The stages of surface cleaning, film growth and patterning are much more complicated for the thermoelectric devices than for the films grown for physical characterisation. The full procedure is therefore described here, along with an outline of how the processes were optimised. The thermoelectric properties of the BiSb samples were measured using the Virginia team's system as mentioned in Chapter 2. Six samples were prepared on flat and patterned InP substrates in Mantis system as listed in Table 4.1. These samples were prepared via three major steps. Firstly, five patterned InP ( 8 mm × 8 mm) substrates

were sputtered in HV system 3 (Mercutio) in similar conditions as those mentioned in Section 4.2, but for different time durations (5-30 min). They were all kept under nitrogen to minimise surface oxidation. Prior to BiSb growth, they were etched into a diluted solution of 5% HCl in IPA (i.e. volume-wise, concentrated HCl to IPA) and then kept in the IPA. The flat substrate of sample MP50 was left for 60 seconds in the solution to remove any contaminants and the oxide layer, more than other patterned substrates which were rinsed for only 20 seconds in the solution to preserve the patterning. Initially, trials to etch the patterned substrates using 1:1 HCl-to-IPA for only 30 seconds obliterated the patterned surface. Therefore, more diluted solutions were investigated and the 5%HCl in IPA solution was selected because it did not affect the SR value after rinsing a typical InP patterned substrate in it for up to 5 minutes. Secondly, all the substrates were dried using a nitrogen gun, then were masked and loaded quickly in Mantis chamber to avoid surface re-oxidation. Afterwards, the substrates were degassed at 250 °C at $10^{-7}$mbar and then left at this temperature with rotation to achieve a uniform-composition BiSb deposition. Bi and Sb thermal boats were heated to obtain a low growth rate (0.5 nm/min), resembling the growth conditions used in the UHV system 2 (Morbius) to have high-quality crystalline samples. After the deposition, all the samples (InP substrates with BiSb films on) were rinsed in an acetone ultrasonic bath for 90 seconds, to get rid of any extra BiSb dust. Thirdly, a layer of gold (i.e. contact electrodes) was deposited using the lithography technique:

- A 2D design of the electrode mask was created using KLayout software (see Figure 4.8 (a)).
- In the clean room, the samples were cleaned with acetone and IPA then were dried with nitrogen and degassed at 110 °C for over 10 min.
- The samples were spin-coated with a positive photoresist (ECI3007) layer at the speed of 4000 rpm; then softly baked at 90°C for 90 s.
- The digital mask design was used to expose the samples with 80 % power of 10 mW laser using Heidelberg $\mu$PG-101 micro pattern generator; the samples were then baked at 110 °C for 90 s.
- They were developed in AZ326 MIF developer solution for 60 s, then rinsed in water and dried with nitrogen.
- Before gold deposition, the samples were degassed at 70 °C for 13 min, then were loaded to the sputterer's chamber (Moorfield Nano PVD-S10A sputtering system)

and left for 60 min at $1\times10^{-5}$ m bar for extra drying.

- A layer of gold was deposited on the masked samples by sputtering a gold target (50% power) with $Ar^+$ with 3 $cm^3$/min flow (at 3.5 $\times10^{-3}$ m bar) for 7 min.
- The lift-off process was done by rinsing each sample in an ultrasonic bath of acetone to remove the residual gold and photoresist materials. A plastic beaker was always used to avoid shattering the brittle InP substrates; it usually occurs whenever glass beakers are used.
- The samples were dried out using a nitrogen gun, and examined, some were imaged, using Nikon Eclipse LV150NA to confirm that electrodes were installed properly, Figure 4.8 (b-d). Panel (b) is the flat sample (MP50); (c) is MP50 using 4 magnified images, labelled: electrical electrodes (E), thermometers (T) with one heater. Panel (d) presents one patterned sample (MP54).

Figure 4.8, panels (e-i) illustrate some of the failed trials during the optimisation period; (e) the electrode was lifted during the lift-off process, this was avoided by rinsing the samples in an acetone ultrasonic bath before the deposition to remove any residual BiSb dust on the surface and allow good adhesion for the gold layer. Panel (f) demonstrates an unclean substrate surface caused by photoresist non-uniformity; panel (g) demonstrates a broken heater, likely originated from unsuitable photoresist exposure, developing or a lift-off duration. In Panel (h), a thermometer pad (right image) was partially removed in the lift-off process, as the photoresist layer becomes thinner near the substrate edges, although it looked normal prior to the developing process (left image). Therefore, BiSb film and electrodes had to be repositioned accordingly. In panel (i), the gold heater touches the BiSb film because the film's edges were not straight; the BiSb metal mask was required to be cut by the CNC machine as described in Chapter 3.

### 4.4.2 Characterisation

The AFM was used to study the surface morphology of the patterned substrates and the deposited BiSb films, besides determining the thickness of the flat sample MP50 and the gold layer. The patterning was confirmed in all the patterned samples, as presented in Figure 4.9. Panel (a) is a plot correlating the RMS roughness and the SR value to the sputtering time of the patterned samples. Both parameters increased monotonically for the first 10 min of sputtering, then reached a plateau with a roughness of 40 nm and a surface ratio of 1.8. This suggests that over 10 minutes of sputtering does not enlarge the

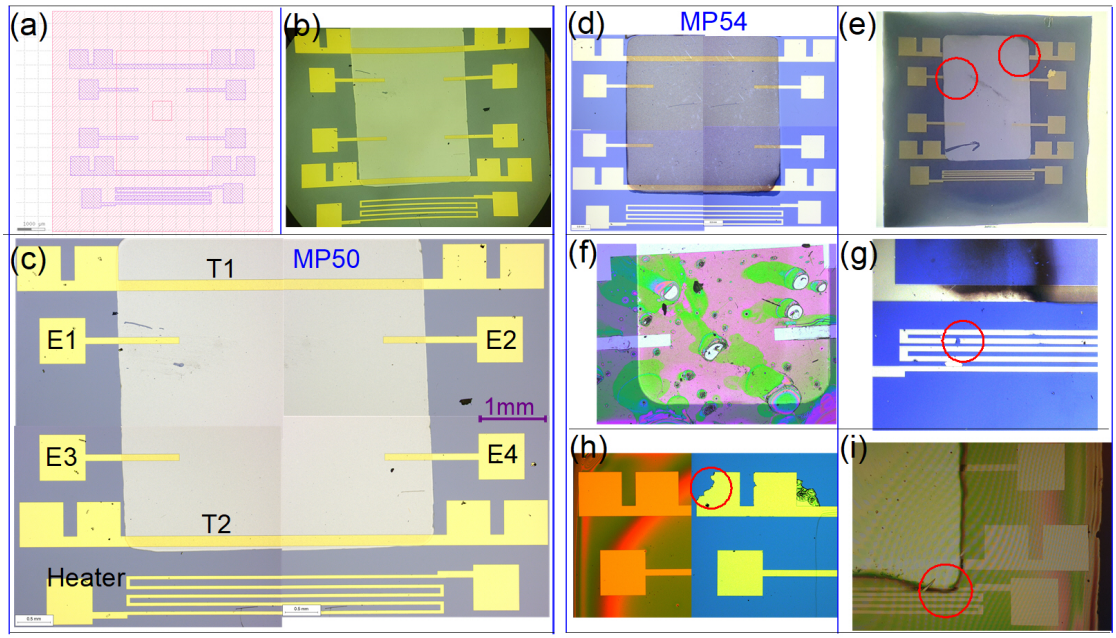


Figure 4.8: The BiSb thermoelectric device optimisation. (a) The design of the photoresist mask. (b) The final BiSb device used (MP50) contains three layers, an InP flat substrate, a BiSb film and gold electrodes. (c) Magnified images of MP50 gold pattern, comprising four electrodes (E), two thermometers (T) and a heater. (d) Images of the MP54 sample (BiSb film on a nano-patterned substrate). Panels (e-i) demonstrate some challenges faced during device optimisation. The electrode pads (E1-E4) are 0.7 mm wide, see scale bar in panel (c).

surface area of the patterned sample, although it may have affected the entropy of the surface. Panels (b-l) demonstrate 3D images of the patterned substrates next to their corresponding BiSb films (MP50-MP55). Overall, the nano-patterning was observed in all the $Ar^{+}$-sputtered InP substrates' morphologies. The surface morphology of the BiSb films is, somehow, correlated to their substrates. Table 4.5 lists the RMS roughness, SR values and the corrected thickness of the prepared films. EDX composition was determined from the flat sample and averaged from 5 scans in two different pieces, with a difference of 1%, confirming the compositional uniformity. The thickness of the sample was measured by scanning the AFM tip over a step, as appears in Figure 4.10; it was then averaged from 4 scans at different locations on the MP50 sample (147±3 nm). Similarly, the gold layer thickness was measured to be (120±5 nm).

As these samples were prepared in another chamber (i.e. Mantis PVD system), the structure of one flat (MP50) and one patterned (MP54) sample, in the device form,

were investigated using XRD, Bragg-Brentano geometry. MP50 and MP54 exhibit a texture dependency on the substrate type, similar to that observed in Section 4.3.1 for the samples grown inside the MBE UHV system 2 (Morbius). Figure 4.11 shows the XRD patterns of these samples as compared to the $Bi_{0.8}Sb_{0.2}$ (PDF 04-023-9518) card [82]. The flat sample MP50 has BiSb (003) and (006) peaks, confirming the (003) orientation with some minor (012) phase. In contrast, the patterned sample (MP54) has the dominant (012) phase, with some (003) and polycrystalline portions. The origin of the '*'-labelled peak is unknown, it may be split from the InP (200) peak because of sputtering-induced strain. However, this was not observed in the sample prepared in the UHV system 2 (Morbius) (Figure 4.2), possibly because the gentle sputtering and annealing in Morbius relieved this stressed layer; but this requires further analysis. Other peaks in the X-ray diffraction pattern belong to the InP substrate and the gold electrodes. The Au (111) peak at $2\theta = 38.18$ overlaps with the BiSb (104) peak at $2\theta = 38.17°$. However, we believe that the BiSb (104) peak is not significant because it is absent in earlier samples (IBS-labelled) prepared in the MBE system 2 (see Figure 4.2). In conclusion, samples prepared using the LP-PVD method in Mantis system have the same structure as those prepared using the UHV MBE system 2 (Morbius).

Table 4.5: The EDX composition and AFM parameters of the MP50-55 series. The thickness of the flat sample is determined from the AFM line profile (see Figure 4.10). The SR values are extracted from topographs in Figure 4.9.

| Sample | MP50 | MP51 | MP52 | MP53 | MP54 | MP55 |
|---|---|---|---|---|---|---|
| Sb (at%) | 23.4 | - | - | - | - | - |
| Bi (at%) | 76.6 | - | - | - | - | - |
| Thickness (nm) | 147.0 | - | - | - | - | - |
| Ar+ Sputtering time (min) | 0 | 5 | 10 | 15 | 25 | 30 |
| RMS roughness (nm) | 9.7 | 24.0 | 38.0 | 35.0 | 45.0 | 40.0 |
| SR (substrate) | - | 1.22 | 2.15 | 2.12 | 2.44 | 2.08 |
| SR (film) | - | 1.10 | 1.49 | 1.27 | 1.38 | 1.48 |
| SR (avarage) | - | 1.16 | 1.82 | 1.69 | 1.91 | 1.78 |
| Average thickness (nm) | 147.0 | 126.7 | 80.9 | 86.8 | 77.2 | 82.5 |

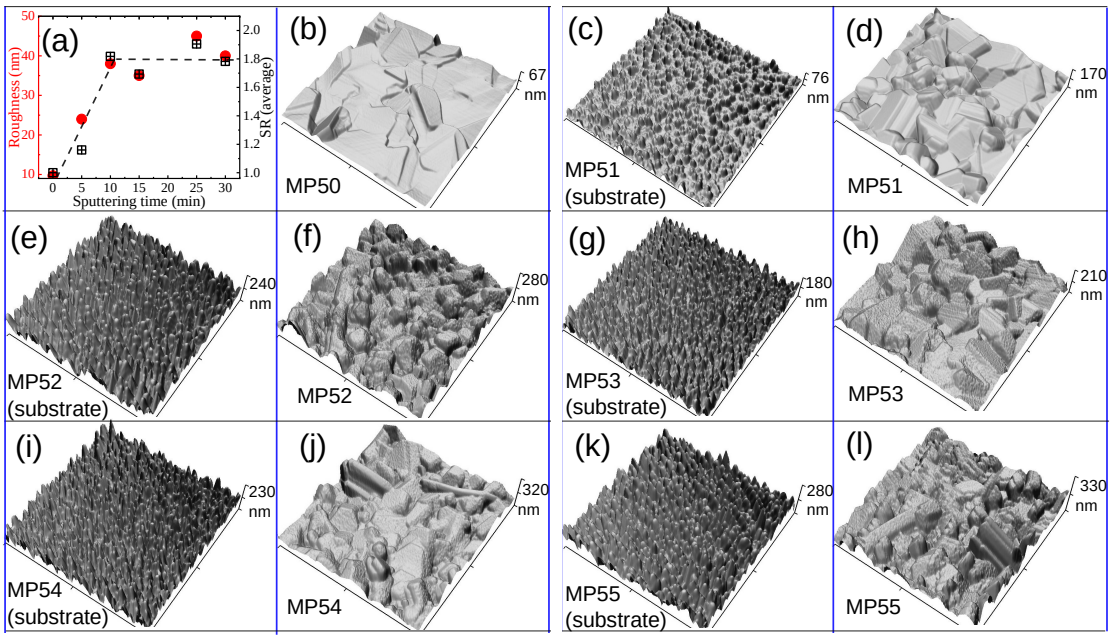


Figure 4.9: Panel (a) shows the roughness and average SR values as a function of the $Ar^+$ sputtering time. The dashed line is included as a guide to the eye. Panels (b-i) are AFM 3D topographs of BiSb films on the flat (MP50) and the patterned (MP51-55) samples next to their corresponding patterned InP substrates. The scan dimension is $2\mu$m $\times 2\mu$m for each topograph.

### 4.4.3 Thermoelectric measurements

#### Temperature dependent conductivity

The sheet conductance of the topological insulators ($G_{sh}$) comes from two channels, the bulk conductance ($G$) and the surface states conductance ($G_{ss}$), such that $G_{sh} = G_{ss}+G$. The temperature dependences of $G$ and $G_{ss}$ differ. For a semiconducting interior, $G = G_o e^{(-\triangle E/K_B T)}$, where $G_o$ is constant and $\triangle E$ is the thermal activation energy for electrical conduction. $\triangle E$ used to be considered as $E_g/2$ [140], which is valid in cases such as single crystal semiconductors with no gap states measured at high temperature, but not with low-temperature measurements in disordered material [5]. In contrast, $G_{ss}$ behaves differently as it is metal-like conduction that decreases with temperature. To investigate the conduction mechanism in our samples, we measured the conductance of the flat sample (MP50) and the patterned sample (MP54) from 300 K down to 10 K. At 300 K, the conductance of the flat film ($G_{sh}$= 0.1 S) was around five times higher than the patterned film's conductance ($G_{sh}$= 0.018 S). This could have resulted from three

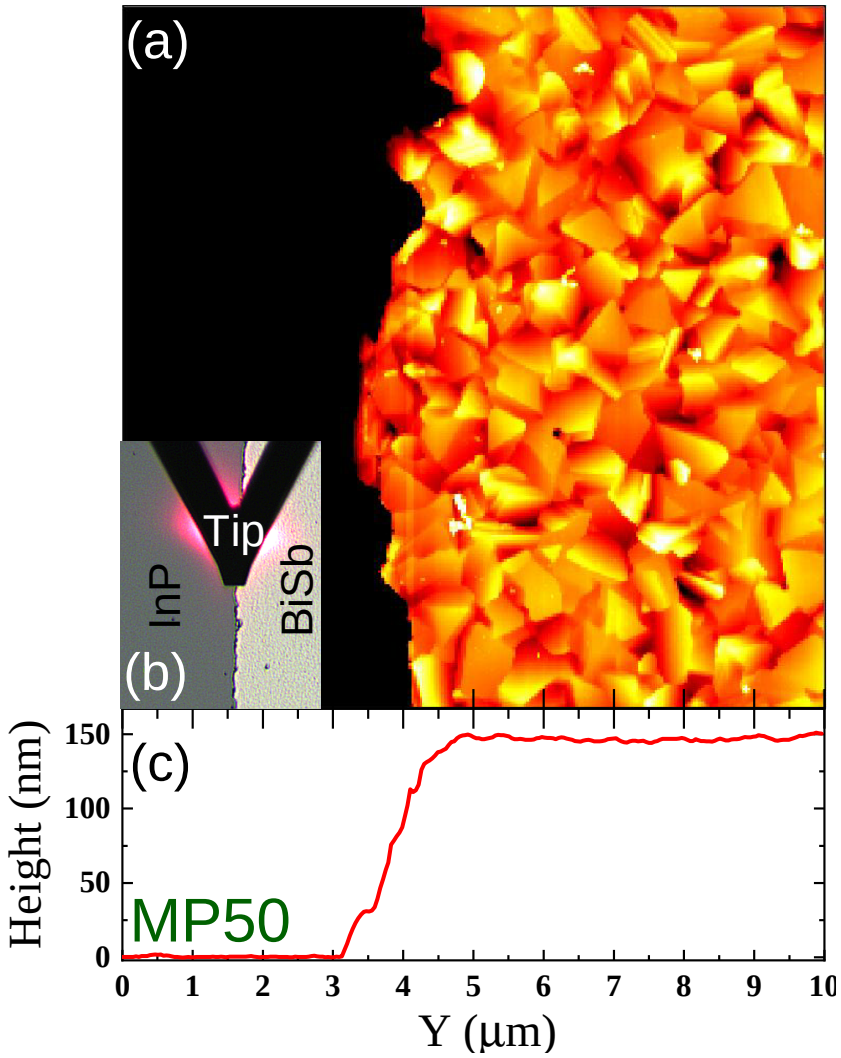


Figure 4.10: Thickness measurements of BiSb on InP substrate (MP50): (a) AFM topograph at the edge; (b) zoomed-out-image of the position of the AFM tip during the measurements; (c) the corresponding mean height profile at the edge [from panel (a)].

factors: (1) the patterned sample has thinner BiSb film with a non-uniform thickness; (2) the carriers in the patterned film may face scattering with the rough InP/BiSb interface, and (3) the film is less textured and nature of BiSb (012) texture differs from that of (003). The calculated band structure of $Bi_3Sb$, close to the composition used in this work, is highly anisotropic [141] and it is very likely that thin films oriented in (003) and (012) directions will have different effective bulk conductivities.

When the samples are cooled, the bulk conductance decreases and the metallic

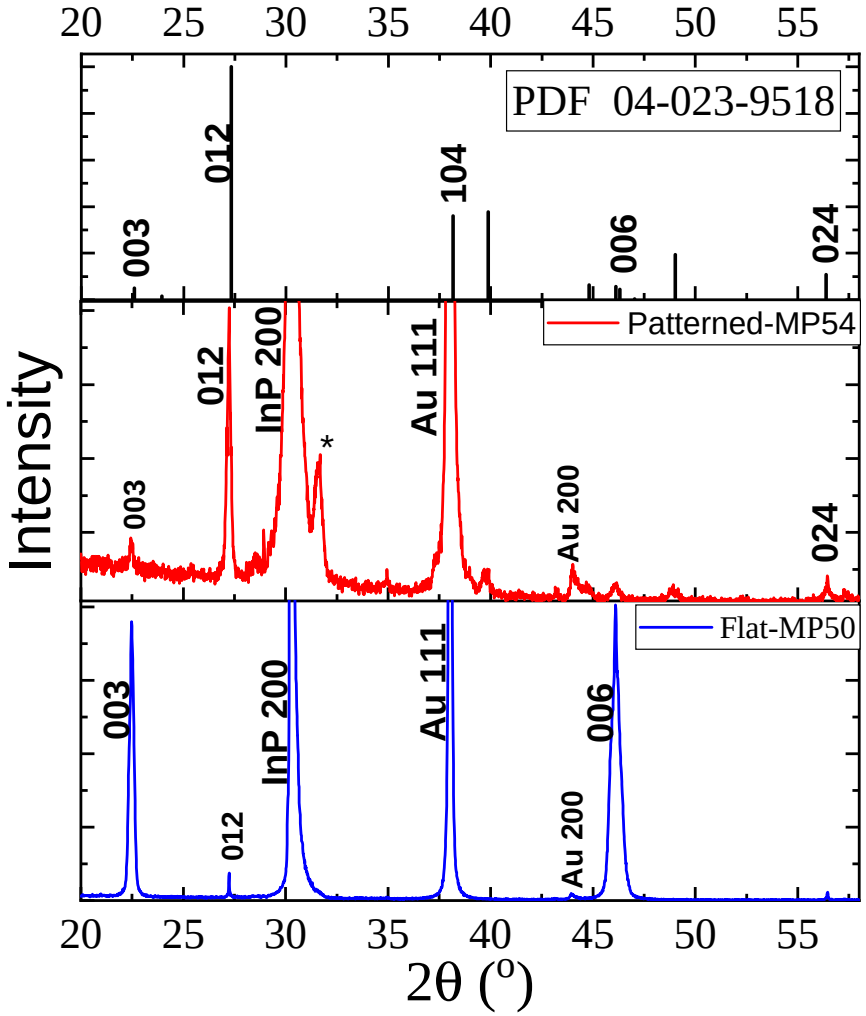


Figure 4.11: XRD patterns of the flat (MP50) and the patterned (MP54) samples with their gold electrodes on. The top panel is $Bi_{0.8}Sb_{0.2}$ (PDF 04-023-9518) card [82]; all indexed peaks belong to that card except specified. The intensity axis is linear and scaled to maximise the BiSb peaks.

conduction increases at different rates. Figure 4.12 illustrates the conductance of both films, normalised to its value at 300 K. In general, the conductance of both films decreases with cooling, suggesting the dominance of the bulk semiconducting behaviour. In other words, the bulk conductance decreasing rate with cooling is higher than the metallic conductance increasing rate. In fact, the patterned sample MP54 exhibited a minimum conductance value at 20 K, which was not observed in the flat one (see inset). At this minimum, the rise in metallic conductance equates to the decline in bulk conductance.

This proves two points: (1) the presence of the metallic states in the sample; (2) the contribution of surface states in the conduction is higher in the patterned sample than the flat one due to the increased surface-to-bulk ratio in the earlier. To analyse the bulk and surface conduction further, the temperature-dependent conductance of both samples was fitted according to different plausible assumptions. First, we assume that the BiSb film is semiconducting with zero or negligible surface states contribution ($G_{ss} = 0$ model). In this case, $G_{sh} = G_o e^{(-\triangle E/K_B T)}$ and $\ln(G_{sh}) = \ln(G_o) - \triangle E/K_B T$. The plot of ln $(G_{sh})$ VS $1/T$ gives the $\triangle E$ value as shown in Figure 4.13 (a). This model fails to interpret the whole data although it fits the high-temperature range, where the surface states contribution is smaller. Obviously, it might represent the conduction in the flat sample for a longer temperature range (300 K to 105 K) than the patterned sample (down to 170 K). That resulted from the greater surface area in the patterned samples that emphasise the surface states contribution. In addition, the value of $\triangle E$ in the patterned sample (16.5 meV) is higher than the $\triangle E$ value of the flat sample (11.2 meV). This could be correlated to higher quantum confinement in the thinner and rougher film of the patterned sample. In fact, by decreasing the thickness of the films, the surface-to-volume ratio increases and the bulk band gap is enhanced [123]. For example, the band gap increases from 10 meV for bulk $Bi_{0.9}Sb_{0.1}$ [142] to 38 meV for 24-nm-thick films [123]. Assuming it equals $2\triangle E$, our band gap values are 33 meV for the patterned sample and 22.4 meV for the flat one, comparable to the 23 meV value reported for 90-nm $Bi_{78}Sb_{22}$ films grown on flat GaAs(111), using the same model [124].

The second model suggests that there is a contribution from the surface states in the conduction $G_{ss}$, and that contribution could be constant (constant $G_{ss}$ model) as applied by Fan et al. [135] or temperature dependent as applied by Muschinske [143]. Both could be simplified as a linear function: $G_{ss}(T) = c_1 + c_2 \times T$, where $c_1$ and $c_2$ are constants. This expression was deduced from the experimental plot of Gss VS temperature in Bi and BiSb thin films by Muschinske [143]. In their study, $G_{ss}(T)$ of Bi could be represented as one straight line with a negative slope, but for BiSb, it could be represented by two lines in different regions, one with a negative slope above 140 K and one with a zero slope (i.e. constant G$ss$) under 140 K.

Fan et al. [135] deduced the values of $G_{ss}$ from the fitting parameters of the normalised resistivity values. Similarly, $(\frac{G_{sh}}{G_{sh}(300)})$ could be expressed as:

$$G_{sh} = c_1 + c_2 T + G_o e^{(-\triangle E/K_B T)}$$

Or

$$\frac{G_{sh}}{G_{sh}(300)} = \frac{c_1}{G_{sh}(300)} + \frac{c_2 T}{G_{sh}(300)} + \frac{G_o}{G_{sh}(300)} e^{(-\triangle E/K_B T)}$$

We tried to fit the normalised conductance ($\frac{G_{sh}}{G_{sh}(300)}$) considering only one region and two regions. In both cases, the fitting function returned with positive temperature dependence (i.e. positive $c_2$ value) that contradicts with the nature of the metallic conduction, if it is purely metallic. When $c_2 \leqslant zero$ was applied as a boundary condition, the fitting function returned negligible or zero value for $c_2$ in both regions. This could be expressed as constant $G_{ss}$, these fittings are shown as solid lines in Figure 4.13 (b). The model fits quite nicely with the flat sample and the patterned sample in the high-temperature region only as the contribution of the surface states becomes more significant below 140 K. This deviation may be also attributed to the bulk gap states' contribution. Since the patterned sample is less pure and contains a polycrystalline phase that supposedly creates localised states in the bulk band gap, the contribution from these states becomes more obvious in the low-temperature region. This could be solved by assuming a second bulk conduction function, with a smaller activation energy (e.g. $\triangle E_2$) which dominates in the lower temperature range. But in this case, the numerous parameters in the fitting equation may predict parameters with high uncertainty. Back to the fitting parameters, the activation energy is higher in the patterned sample (28.8 meV) than the flat one (18.4 meV) which makes sense in this case as well. Nevertheless, the values of $G_{ss}$ are 28.7 mS for the flat sample and 7.05 mS for the patterned one. This is against what might be expected that $G_{ss}$ of the patterned sample is higher since it has more surface area. This could be argued that (1) the patterned film is (012) oriented and (2) it has a more rough surface that makes an impact on the surface states; the surface-to-total conductance ratio that matters in this case. In fact, understanding the topological properties of materials and how these properties relate to the electronic structure of the material depends on the symmetry features that a crystal may have [144]. For example, the bulk energy bands of BiSb have additional topological structure due to the presence of mirror symmetry in its crystal lattice [144].

Assuming having single $\triangle E$ and the constant $G_{ss}$, the ratio of the surface conductance $G_{ss}$ to the total $G_{sh}$ could be presented as shown in the inset figure. One can notice that the contribution of the surface conductance is higher in the patterned film and exceeds 50% below 224 K, sooner than 128 K for the flat sample. In conclusion, the films behave as semiconducting with surface states that are best described by having a constant $G_{ss}$, reflecting that it is not purely metallic. The patterning enhanced the surface contribution, but the total conductance remained less than without patterning.

They might become alike by using the concept of the corrected electrical parameters that was presented in Section 4.3.4; but this needs samples (with equivalent corrected thickness) to compare.

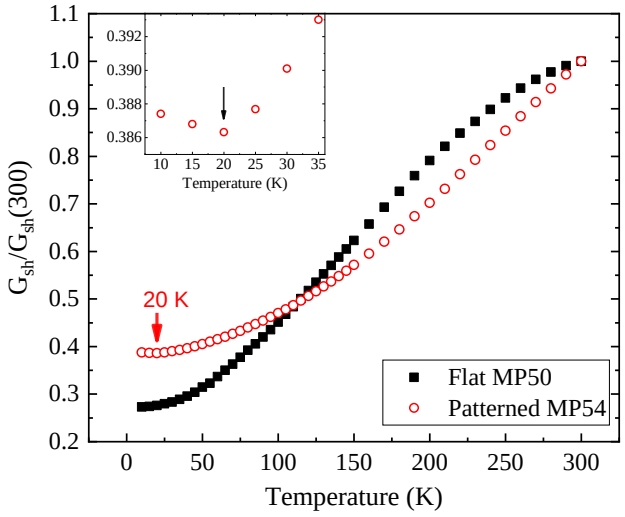


Figure 4.12: The temperature dependence of the total sheet conductance in the flat, MP50 and the patterned, MP54 samples normalized to the value at 300 K. The inset shows the minimum conductance value in the patterned sample.

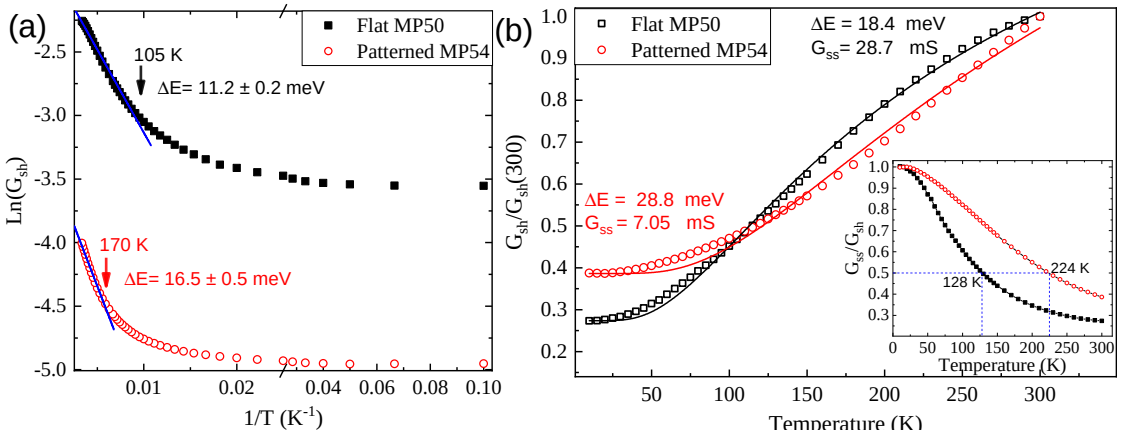


Figure 4.13: (a) ln G VS 1/T (blue lines are fitting with $G_{ss} = 0$ model). (b) Fitting of normalised $G_{sh}$ VS temperature with constant $G_{ss}$ model.

### Thermoelectric measurements

To better understand the effect of the patterning on the thermoelectric performance, the resistance and Seebeck coefficient of the samples were determined. Since the patterning increases SR and creates a rough surface, the thickness of the patterned samples becomes non-uniform with a reduced average value as listed in Table 4.5. In this section, we compare the resistance ($R$), Seebeck coefficient ($S$) and ($S^2/R$) values for all flat and patterned samples, instead of using the conductivity and power factor. In general, patterning the samples affected the thermoelectric performance significantly. Figure 4.14 shows the dependence of the resistance and the Seebeck coefficient on both the temperature and the $Ar^+$ sputtering time. In panel (a), the resistance of all samples decreases with temperature, reflecting the dominant semiconducting behaviour of all flat and patterned samples as discussed previously. Apart from the 15-minute sputtered samples (MP53), the resistance increased with the sputtering time because of the smaller average thickness, phase difference and increasing non-uniformity. The reason for the low resistance of sample MP53 is unknown. For the Seebeck coefficient [in panel (b)], all samples show the negative sign with $S$ values, confirming the n-type semiconducting behaviour in the grown films. The value of $|S|$ increases with temperature in all the patterned samples, but peaks in the flat sample at 250 K. There is no trend between the values of $S$ and the sputtering time, but mostly, the patterning reduces the $S$ values. To compare, the values of $S$ at 300 K varies from 22 $\mu$V/K to 130 $\mu$V/K near the value of 90 $\mu$V/K for (012) ball-milled $Bi_{77}Sb_{23}$ samples [125].

The resultant power-factor-equivalent term ($S^2/R$) is plotted in Figure 4.15(a) VS temperature of the prepared films. The maximum value for the flat sample is at 250 K, while the randomness of the $S$ values with the sputtering time appears in the ($S^2/R$) values as well. In other words, patterning the InP substrate results in uncontrollable reduced variation in the values of ($S^2/R$). The power factor of the flat sample (MP50) is plotted versus temperature in Figure 4.15(b). At a temperature of 250 K, the power factor reaches a maximum value of 6 mW/mK$^2$. This is higher than the maximum power factor of 4.6 mW/mK$^2$ reported for (003)-oriented $Bi_{0.8}Sb_{0.2}$ co-sputtered films with a thickness of 100 nm [133]. It is also higher than the maximum power factor of 5.3 mW/mK$^2$ for a $Bi_{0.91}Sb_{0.09}$ thin film grown on CdTe(111), which also peaked at 250 K [145].

As an estimation for the figure of merit value (ZT) of the flat sample, we used the temperature-dependent thermal conductivity values of the polycrystalline 150-nm $Bi_{80}Sb_{20}$ thin film published by Volklein et al. [146]. Estimated ZT values peak to reach

0.67 at 250 K, this peaking trend was observed in different-composition different-thickness BiSb thin films at 200-250 K [146]. This ZT is greater than both the $Bi_{88}Sb_{12}$ hot-pressed samples (0.28-0.3 around 250 K ) [137] and the melt-spun n-type $Bi_{85}Sb_{15}$ bulk samples with micron-sized grains, which have a ZT of around 0.6 at 125 K [147]. The estimation of ZT for patterned films is difficult, even when using the average thickness concept to estimate the conductivity and power factor values, the thermal conductivity of the patterned samples is unpredictable. However, the thermal conductivity of $Bi_{75}Sb_{25}$ (012) oriented ball-milled samples is 2.51 W/mK at room temperature [125], not far from the polycrystalline value we used in our estimation (3 W/mK, at room temperature) [146]. But, for the patterned samples, other important factors are believed to hinder heat conduction as they are thinner, less textured and probably smaller grained which will have more grain boundaries, meaning potentially more phonon scattering (i.e. lower thermal conductivity). Therefore, a dataset of thermal conductivity is needed to accurately evaluate the ZT values.

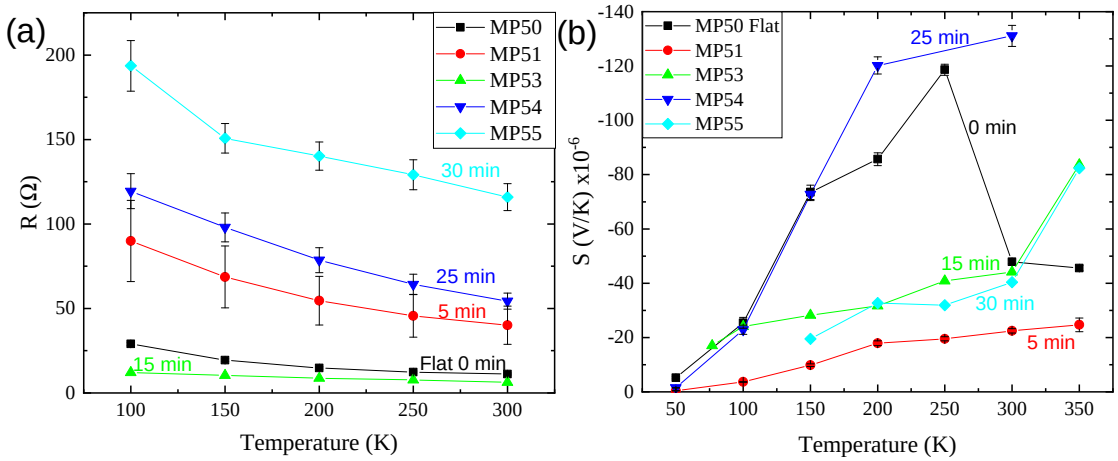


Figure 4.14: The effect of nano-patterning the substrates on the thermoelectric parameters of BiSb thin films: (a) The resistance as a function of temperature; (b) the Seebeck coefficient as a function of temperature. Each plot is labelled with the corresponding substrate sputtering time (in the same colour).

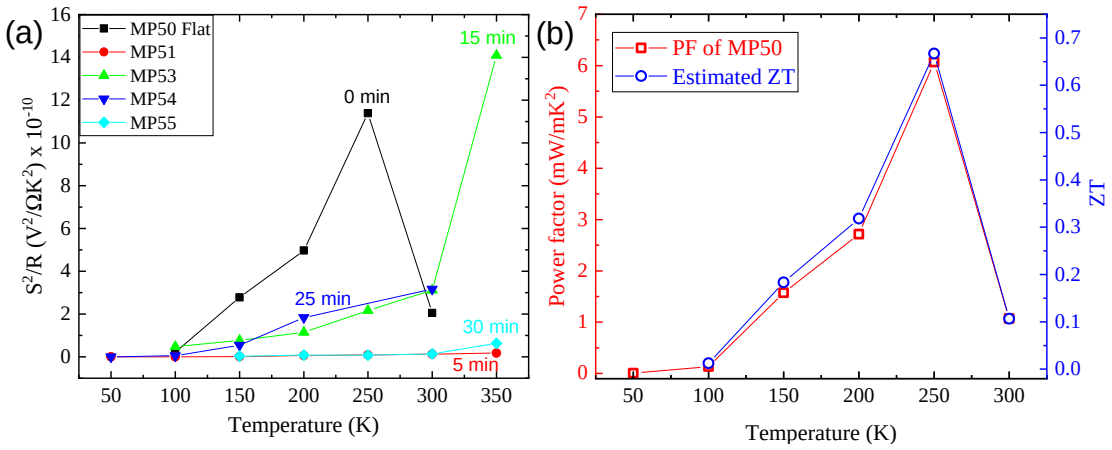


Figure 4.15: (a) The dependence of power factor equivalent term ($S^2/R$) on the substrates patterning in the BiSb samples. (b) The power factor as a function of the temperature of the flat BiSb sample (MP50); ZT is estimated using thermal conductivities from [146].

## 4.5 Conclusion

In this study, $Bi_{77}Sb_{23}$ thin films were deposited on flat and patterned InP substrates. The films' morphology, structure, and electrical and thermoelectric properties were investigated. It has been found that films grown on flat InP substrates have highly textured (003) orientated films, while those grown on patterned substrates are mostly (012) phase with a minority of other (003) and polycrystalline phases. This was confirmed for both MBE and PVD growth.

The patterned samples have a smaller non-uniform thickness, which lowered their conductance and average conductivity compared to the corresponding flat samples. However, the conductivity of the two types of samples could be considered equal if they had the same corrected (average) thickness.

All the flat and patterned films exhibited behaviour characteristics of n-type semiconductors, although surface states' contribution was detected. The ratio of surface state contribution was consistently higher in the patterned samples, but the total conductance was higher in the flat samples, owing to the different thickness, structures and morphology. The Seebeck coefficient increased with temperature for all of the patterned samples, but peaked at 250 K for the flat samples, with a high power factor value (6 $mW/mK^2$). At the same temperature, the figure of merit was estimated to reach a high value $ZT$=0.67 for the flat (003) oriented sample. To fully assess the impact of the nano-patterning on $ZT$, thermal conductivity measurement is required for the samples.

# Chapter 5

# ZnSb Thin Films

Zinc antimonide is one of the most promising TE materials because of its excellent material properties [148, 149], the abundance of Zn and Sb, its cheap price and non-toxicity. The electronic configuration and phases are discussed in appendix A. The materials' high figure of merit ZT reaches around 1.3 at 670 K for $Zn_4Sb_3$ compounds [150, 151]. One of the major problems with this material is its thermal stability, as operation at a high temperature can lead to considerable changes in the material properties, eg. the grain size of ZnSb pellets was nearly doubled by annealing at 300°C [149, 152]. At high temperature, Zn atoms become more mobile to migrate from their initial site to an interstitial one easily which benefit the thermal conductivity at the expense of the material's thermal stability [153]. Thermoelectric power factor (PF) was observed to degrade with thermal cycling due to changes in composition, morphology and structure (PF value decreased about 30% after 10 cycles at 300°C) [154]. This reduces TE device reliability. This TE material is a strong candidate for applications that operate at room temperature or slightly higher (say up to 400 K) such as flexible electronics and wearable devices. Moreover, flexible substrates could be easily shaped and processed, minimising the overall waste in the production process [155]. For undoped ZnSb films grown by RF magnetron sputtering on flexible polyimide substrate, a PF of 450 $\mu$W/m.K$^2$ was obtained at room temperature that increased to 2350 $\mu$W/m.K$^2$ at 260°C [156]. Two other publications show the enhancement of TE parameters by titanium [157] and indium [158] doping of ZnSb films grown by multistep co-sputtering technique on flexible polyimide substrates, but no mechanical or bend testing was presented to validate the stability of the films under bending stresses. Lee et al. [159] showed the suitability of screen-printed ZnSb films for flexible TE modules by obtaining 0.22 mW/cm$^2$ from p-type material only. But the film's resistance and Seebeck coefficient showed different dependence on the bending

radius of curvature when put under test.

In this chapter, ZnSb films have been grown on glass and Kapton flexible substrates by LP-PVD with varying Zn/Sb flux ratios and with or without In doping. Electrical and optical properties have been measured before and after $10^4$ bending cycles of push-to-flex treatment. The thermoelectric power factor of the flexible films was also determined as a function of the temperature below 400 K and In-doping.

## 5.1 Sample preparation

### 5.1.1 Substrate preparation

ZnSb thin films were grown on different insulating substrates, namely glass and flexible Kapton, a commercial polyimide film. Commercial glass slides were cleaned by micro-90 in an ultrasonic bath and then washed with DI water. After that, they were treated chemically with a diluted solution (0.03 %) of $SnCl_2$ for 15 min, followed by 20 min-200°C-annealing in the air to form a layer of tin oxide as described by Pejova et al. [64, 65]. The purpose of the SnO layer is to enhance the adhesion of the grown films with the substrate and improve their crystallinity [64, 65]. The prepared slides were then kept under dry nitrogen until used in the deposition. The conductivity of the treated substrate was tested to ensure that it remains insulating and that the SnO layer is not electrically conductive. Kapton film substrates of 0.05 mm thickness were cleaned with IPA and dried with nitrogen.

### 5.1.2 ZnSb films growth optimisation

ZnSb thin films were prepared inside HV system 3 (Mercutio, $P < 10^{-6}$ mbar). The substrates were degassed inside the chamber by an IR lamp for more than 20 minutes, expecting to reach a temperature around 200°C, while Zn and Sb effusion cells were used to provide controlled fluxes of Zn and $Sb_4$. The stoichiometric composition was reached by preparing different samples and comparing their composition using EDX analysis. For indium-doped films, another cell was used to deposit (In) simultaneously. In this study, the term doping refers to the addition of a new element (In) with a small percentage (2-6%), similar to alloying; it does not refer to controlling carrier concentration by incorporation of non-isoelectronic elements. This term is commonly used among researchers to describe adding different dopants to ZnSb thin films and composites with similar percentages [157, 160–162]. All prepared films were silver mirror-like in colour, but a slight change in colour and brightness was observed between different composi-

tions. For example, Zn-rich samples look "rustier" (because of the rough surface they form) and less reflective than Sb-rich samples. All samples were then gently annealed at 150°C to 200°C to turn them crystalline, as discussed later. In this study, films were grown on glass (squares with around 0.9 cm side) and/or Kapton (strips $\approx$ 2.7 cm $\times$ 0.8 cm) substrates with five ZnSb and five ZnSbIn compositions as listed in Table 5.1. Thermoelectric measurements samples are Kapton sheets ($\approx$ 3.5 mm $\times$ 13.7 mm) that were fixed on same-size glass slides using vacuum-compatible sodium silicate solution that was cured by 10-min annealing at 120°C. This glue was suitable to be used in the vacuum system, but it soon failed to hold the samples for the measurements so it was replaced by a double-sided Sellotape. All films were kept under nitrogen, except when being flexed or measured.

The as-prepared films have very high resistance (of an order of 1 M$\Omega$), and the electrical measurements were not stable. Using gentle annealing at 150°C under nitrogen for 1 hour improved the stability of the measurements and reduced the resistance of the initial test sample. Figure 5.1 shows the electrical parameters for a typical non-stoichiometric film. Even after a 1 hour anneal at 150°C, the conductivity became of the order 200 $\Omega^{-1}$ cm$^{-1}$ at room temperature (resistance of order of k$\Omega$). Some samples required higher temperatures or longer anneal to achieve the high conductivity state, depending on their composition. Usually, samples with a Zn/Sb ratio near one require more annealing. To investigate the effect of different heat treatments, the electrical parameters were measured at 77 K and 300 K, while increasing the treatment time and temperature (see Figure 5.1). It is obvious also that after 300°C annealing, the conductivity of the sample at 77 K became higher than at 300 K as small discoloured patches started to appear on its surface. That could be attributed to Zn evaporation and a phase transition, as annealing at 300°C was reported to decompose ZnSb powder and evaporate Zn [163]. 400°C-annealing for 30 min was also reported to increase the carrier concentration and conductivity by more than three multiples because of the Zn vacancy formation [163]. But electrical parameters were very stable as a function of annealing time below 250°C and when stored for 6 months (Figure 5.1). These films were initially non-crystalline, which makes the mobility of the charge carriers very low, with unstable measurements. The annealing improved the crystallinity which increased the mobility and stabilized the measurements. Figure 5.2 shows the GIXRD pattern of another typical sample ($Zn_{54}Sb_{46}$). (a) shows the non-crystallinity of the as-prepared sample and (b) shows a great improvement in its crystallinity after annealing at 150°C under nitrogen for 1 hour. All samples used in this chapter were annealed at temperatures 150°C and 200°C with different time periods until reaching the high conductivity state with stable

electrical parameters.

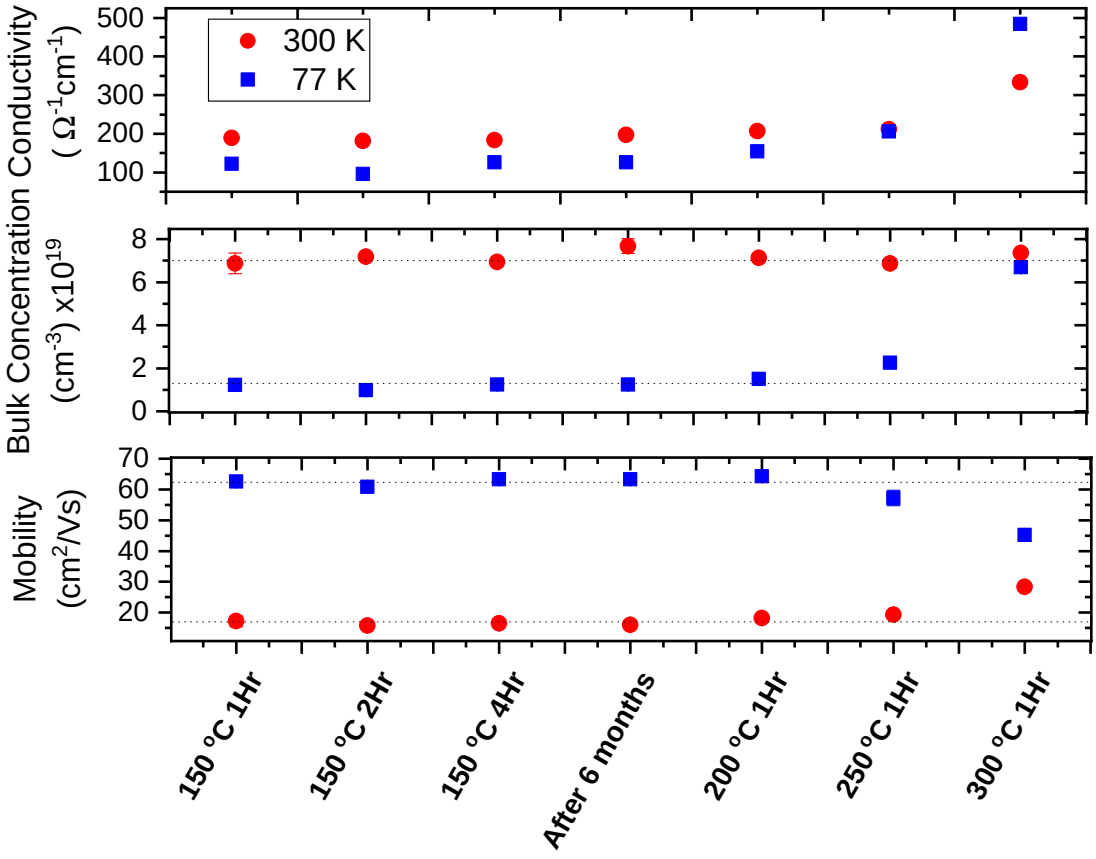


Figure 5.1: Conductivity, carrier concentration and mobility for $Zn_{65}Sb_{35}$ films at different annealing stages.

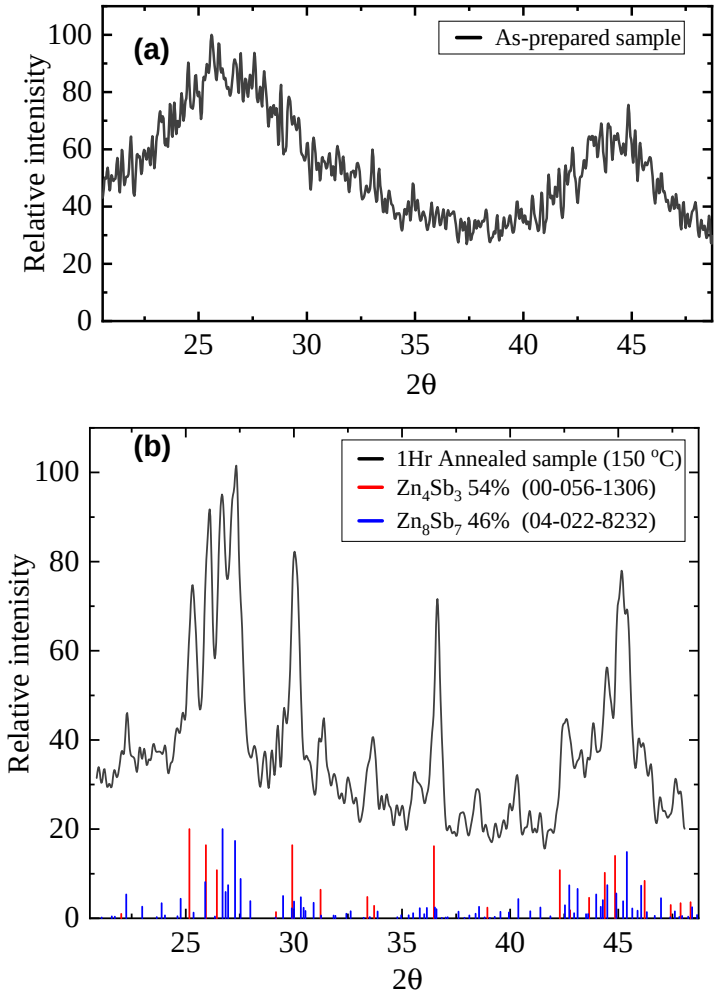


Figure 5.2: GIXRD of an as-prepared ZnSb thin film sample (a), and after being annealed at 150 C for 1 hour. Panel (b) shows the effect of gentle annealing on the crystallinity of the sample. Two crystalline phases ($Zn_4Sb_3$ and $Zn_8Sb_7$) were observed in the annealed sample.

Table 5.1: Summary of ZnSb film samples. The composition is determined from EDX, and the thickness is determined using AFM.

| Sample | Composition (at%) | | | Thickness (nm) | | Substrate | | |
|---|---|---|---|---|---|---|---|---|
| | Zn | Sb | In | value | error | Glass | Kapton | TE |
| **IZS51** | 23.2 | 76.8 | 0.0 | 227 | 5 | x | x | |
| **IZS52** | 64.3 | 35.7 | 0.0 | 115 | 5 | x | x | |
| **IZS53** | 48.1 | 51.9 | 0.0 | 169 | 4 | x | x | x |
| **IZS55** | 51.1 | 46.5 | 2.4 | 222 | 3 | x | x | x |
| **IZS56** | 47.5 | 47.2 | 5.3 | 320 | 4 | x | x | x |
| **IZS57** | 47.3 | 49.3 | 3.4 | 320 | 4 | x | x | x |
| **IZS58** | 54.2 | 41.5 | 4.3 | 298 | 3 | | x | x |
| **IZS59** | 51.6 | 41.6 | 6.8 | 252 | 4 | | x | |
| **IZS61** | 52.5 | 47.5 | 0.0 | 135 | 3 | x | | |
| **IZS64** | 56.4 | 43.6 | 0.0 | 186 | 6 | x | | |

## 5.2 ZnSb on Glass

### 5.2.1 GIXRD

After annealing, the films were assessed by the GIXRD technique to identify their phases. Figure 5.3 shows the diffraction pattern of the undoped ZnSb films ordered from low to high Zn percentage. The sample with overall 23% Zn (lowest panel, IZS51) contains about 46% of Sb and 54% of $\beta-Zn_8Sb_7$. The three middle patterns are from nearly stoichiometric ZnSb films (within 6-4 %). It is clear that changes in the overall Zn:Sb ratio of just a few % have a strong influence on the phase composition near stoichiometry. Pure ZnSb phase occurs in the film with 48% Zn (IZS53), with excess Sb crystallites separately. With a small excess of Zn (52.5 %, IZS61), ZnSb is still dominant, with $Zn_4Sb_3$ appearing. Phase-pure $Zn_4Sb_3$ appears when the overall stoichiometry is close to 4:3 (56.4 % Zn, IZS64). At a still higher Zn-to-Sb flux ratio, more Zn then precipitates on the surface to form solid bulbs and increases the roughness (see AFM of IZS52, Figure 5.6). The low-angle hump observed in the IZS52 diffractogram probably results from that roughness. Table 5.2 gathers the phase quantification data, showing good agreement between the compositional analysis done by EDX and compositions calculated from the phase quantification. PDF 04-014-2869 card was used for ZnSb phase, while $Zn_4Sb_3$ phases were obtained from $\alpha$-$Zn_{13}Sb_{10}$ PDF 04-015-9195, and $\beta$-$Zn_4Sb_3$ PDF 01-073-6841. For $\beta-Zn_8Sb_7$, PDF 04-022-8232 was used. For elements, PDF 01-078-7023 was used for Zn, PDF 04-016-8006 and 04-003-6952 for Sb, and PDF 01-077-2710 for In. For InSb, PDF 04-006-2627 was used and PDF 01-085-2725 for $In_2O_3$

Table 5.2: Phase quantification from GIXRD patterns of annealed ZnSb films on glass and overall compositions from XRD phase compositions, together with overall composition obtained from EDX.

| Sample code | XRD (%) | | | EDX (at%) | | | Phase Quantification (%) | | | | | | | |
|---|---|---|---|---|---|---|---|---|---|---|---|---|---|---|
| | Zn | Sb | In | Zn | Sb | In | ZnSb | $\alpha/\beta$-$Zn_4Sb_3$ | $Zn_8Sb_7$ | Zn | Sb | In | InSb | $In_2O_3$ |
| **IZS51** | 29.0 | 71.0 | | 23.2 | 76.8 | | | | 54 | | 46 | | | |
| **IZS52** | 64.0 | 36.0 | | 64.3 | 35.7 | | | 82 | | 18 | | | | |
| **IZS53** | 45.5 | 54.5 | | 48.1 | 51.9 | | 91 | | | | 9 | | | |
| **IZS55** | 52.0 | 43.0 | 2.6 | 51.1 | 46.5 | 2.4 | 27 | 68 | | | | 1 | | 4 |
| **IZS56** | 52.0 | 44.0 | 4.0 | 47.5 | 47.2 | 5.3 | 29 | 66 | | | | 3 | 2 | |
| **IZS57** | 46.0 | 48.0 | 4.5 | 47.3 | 49.3 | 3.4 | 55 | 33 | | | 5 | 3 | 3 | |
| **IZS61** | 51.5 | 48.5 | | 52.5 | 47.5 | | 85 | 15 | | | | | | |
| **IZS64** | 57.0 | 43.0 | | 56.4 | 43.6 | | | 100 | | | | | | |

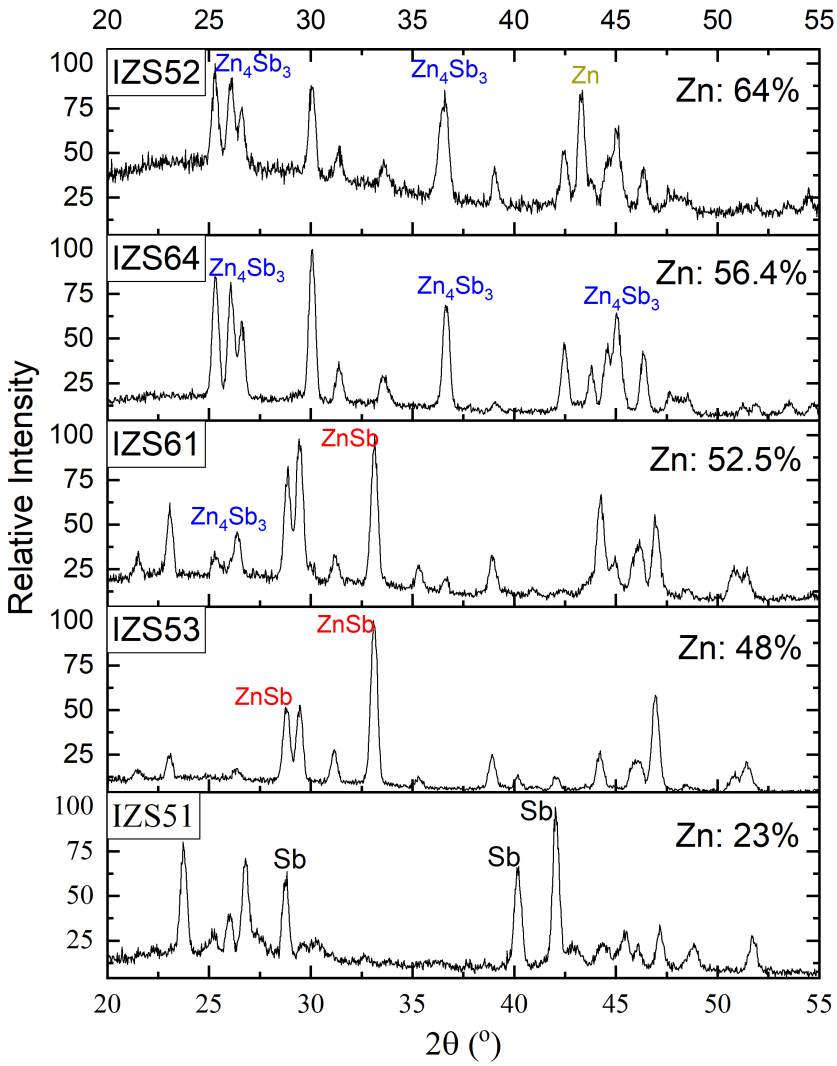


Figure 5.3: GIXRD diffraction patterns of undoped ZnSb films after annealing. The patterns are ordered from low Zn content at the bottom to higher Zn percentage at the top. The sample code of each sample is written on the top left of each pattern, while some distinguished peaks are marked with their phase. Zn percentage at the right is determined from EDX.

The effect of In on the phase composition of ZnSb was studied by growing a set of samples with nominally identical Zn:Sb ratio and increasing In content. However, it is more challenging to identify the effects of In on phase composition owing to the high

sensitivity of phase composition to the precise Zn:Sb ratio in the absence of In doping (Figure 5.4), i.e. effects ascribed to In could be related to unintentional changes in Zn:Sb ratio from changes of flux ratio in LP-PVD. No trend is obvious from Figure 5.4, but all samples within 27-55% ZnSb and 33-68 % $Zn_4Sb_3$.

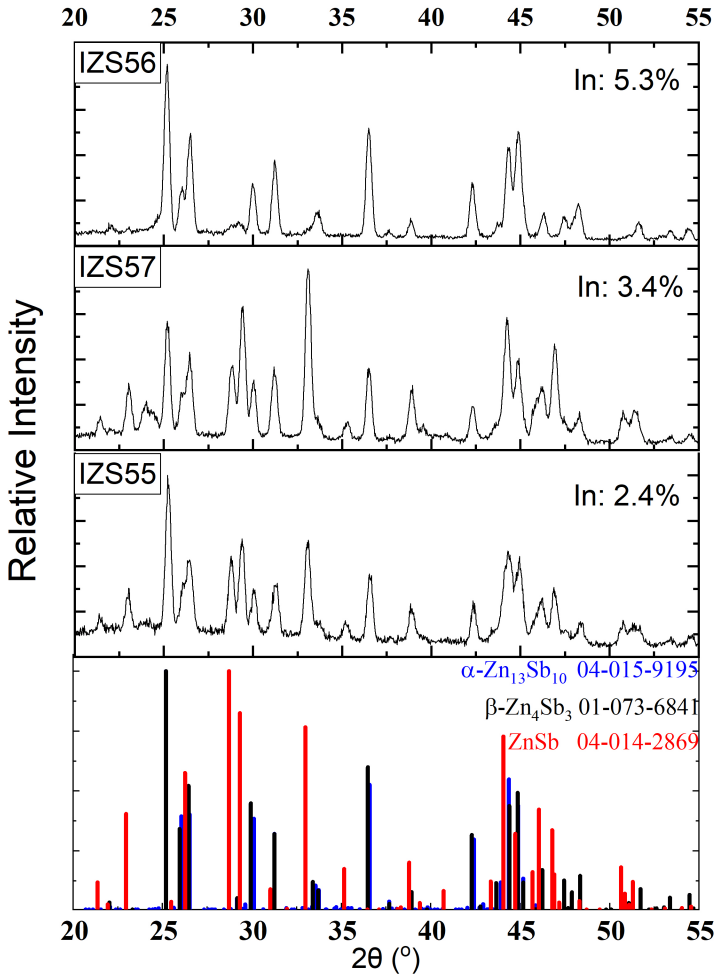


Figure 5.4: GIXRD patterns of In doped ZnSb films. Lower panel: the stick patterns of three ZnSb phases used in the quantification, PDF 04-014-2869 for ZnSb phase, $\alpha$-$Zn_{13}Sb_{10}$ PDF 04-015-9195, and PDF 01-073-6841 [82] for $\beta$-$Zn_4Sb_3$.

### 5.2.2 AFM

The AFM was used to determine the thickness of the films by scanning over their edges as explained in Chapter 2. Figure 5.5 shows the line profiles of the studied samples, varying

from 135 nm to 320 nm as tabulated in Table 5.1. Figure 5.6 shows the topography of the ZnSb on glass samples. In the middle row, ZnSb samples near-stoichiometry (IZS53 and IZS61) show well-defined particles, which are less clear in IZS64. The top row shows the most off-stoichiometric samples. Very Sb-rich IZS51 shows a mottled surface topography, smoother than the Zn-rich IZS52 which has large Zn agglomerates. In the latter case, the underlying ZnSb granular film features can be seen. This structure is most obvious for the near-stoichiometric samples IZS53 and IZS61 (middle row). The moderately Zn-rich IZS64 appears smoother, as do the In-doped samples (bottom row), though in the latter case, there appear to be In clusters decorating the surface. The overall appearance of In-doped films was less homogeneous than the undoped films.

Figure 5.7 (a,b) shows the size distribution of the surface particles in IZS53 and IZS61 from AFM images. Mean particle diameters are 104 nm and 72 nm respectively. Williamson-Hall plots are shown for IZS53 and IZS64 samples in panels (c,d). For the predominantly single-phase samples IZS53 (ZnSb) and IZS64 ($Zn_4Sb_3$), clear WH fits are obtained ($R^2 \geq 0.70$). For, IZS53, the WH grain size is 23 $\pm$ 1.1 nm, smaller than both the AFM mean particle size and the film thickness. This trend is maintained for other samples, e.g. for IZS61, the AFM particle size is 72 nm, smaller than the film thickness 135$\pm$ 3 nm, while the WH grain size for IZS64 is 23 $\pm$ 1 nm, much smaller than the film thickness of 186 $\pm$ 6 nm. Strains determined for WH analysis are small in all cases, $\leq$ 0.1%. So the overall picture is of granular polycrystalline films, where individual particles are not themselves single crystals.

### 5.2.3 Electrical measurements

In general, all In-doped and undoped films have a positive sign for the carrier concentration, reflecting their p-type nature. For the undoped ZnSb thin films, Hall measurements show great dependence on the ZnSb composition. Figure 5.8 shows the carrier concentration and mobility dependence on the Zn percentage in the studied films. In general, the very Sb-rich sample (Zn:23%) has the highest bulk carrier concentration and mobility values. By increasing the Zn content in the rest of the samples, the bulk concentration increases from $6.2\times10^{18}$ $cm^{-3}$ at (Zn:48 %) to $4.9\times10^{19}$ $cm^{-3}$ at (Zn:56 and 64 %) and the mobility falls from 126 $cm^2/Vs$ at (Zn:48 %) to 23 $cm^2/Vs$ at (Zn: 64 %) at 300 K. This could be dependent on the ZnSb/$Zn_4Sb_3$ phases' ratio. Zhang et al. studied ZnSb samples with Zn varying from 50 to 70% [164] and Jang et al. with Zn vary from 53 to 57% [165]. Their samples contain a mixture of ZnSb and $Zn_4Sb_3$ phases and have very close values for carrier concentrations and mobility at 300 K as shown in Figure 5.9.

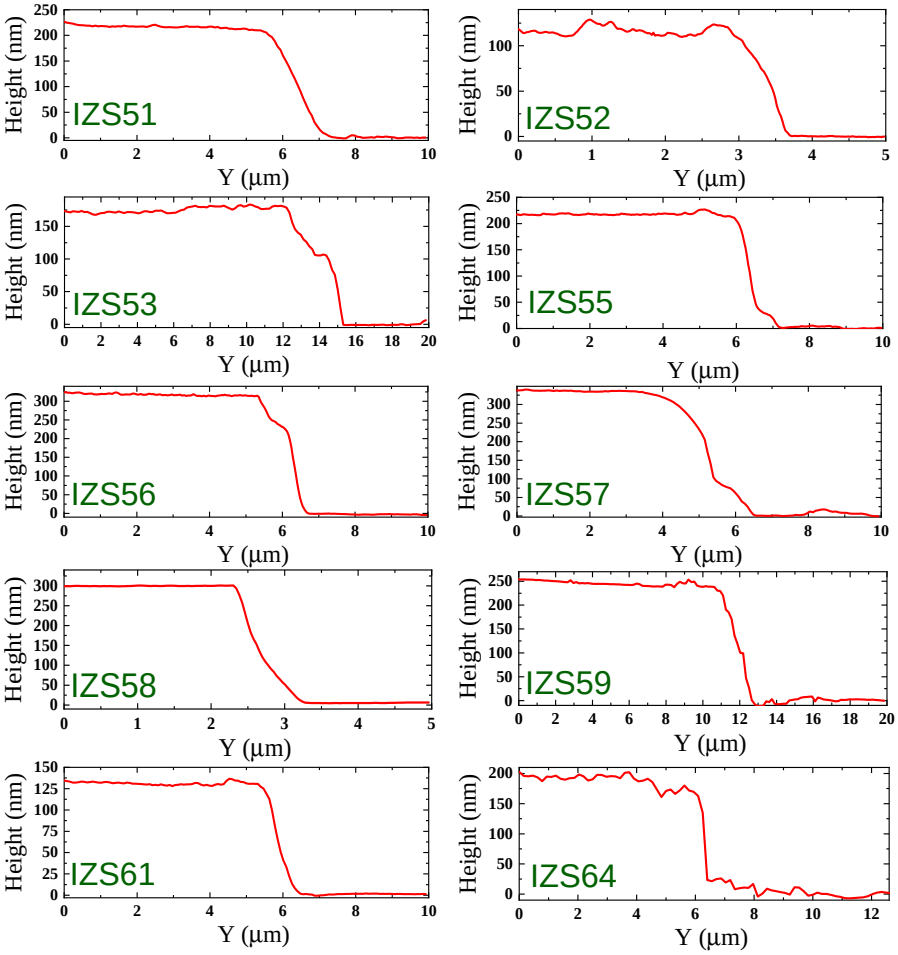


Figure 5.5: AFM line profiles over film edges, as described in the text. Averaged values of the step heights are reported in Table 5.1 as film thicknesses.

The mobility of the charge carriers is obviously falling as Zn % increases (more $Zn_4Sb_3$ replacing ZnSb). In contrast, the carrier concentration increases sharply above a Zn fraction of 54%, with a possible peak at 57% corresponding to exact $Zn_4Sb_3$ stoichiometry. It is noteworthy that the samples in Figure 5.9 from several studies were grown and annealed under varied conditions that might have affected their electrical properties. For instance, the carrier concentration and mobility values were reported to be affected by the annealing temperature [156].

The second observation, from Figure 5.8, is that the electrical parameters of the two Zn-rich samples (Zn $>$ 55%) are more temperature-dependent than the stoichiometric ones. Bulk concentration rises by a factor of 2.5-5 from 77 K to 300 K for the Zn-rich

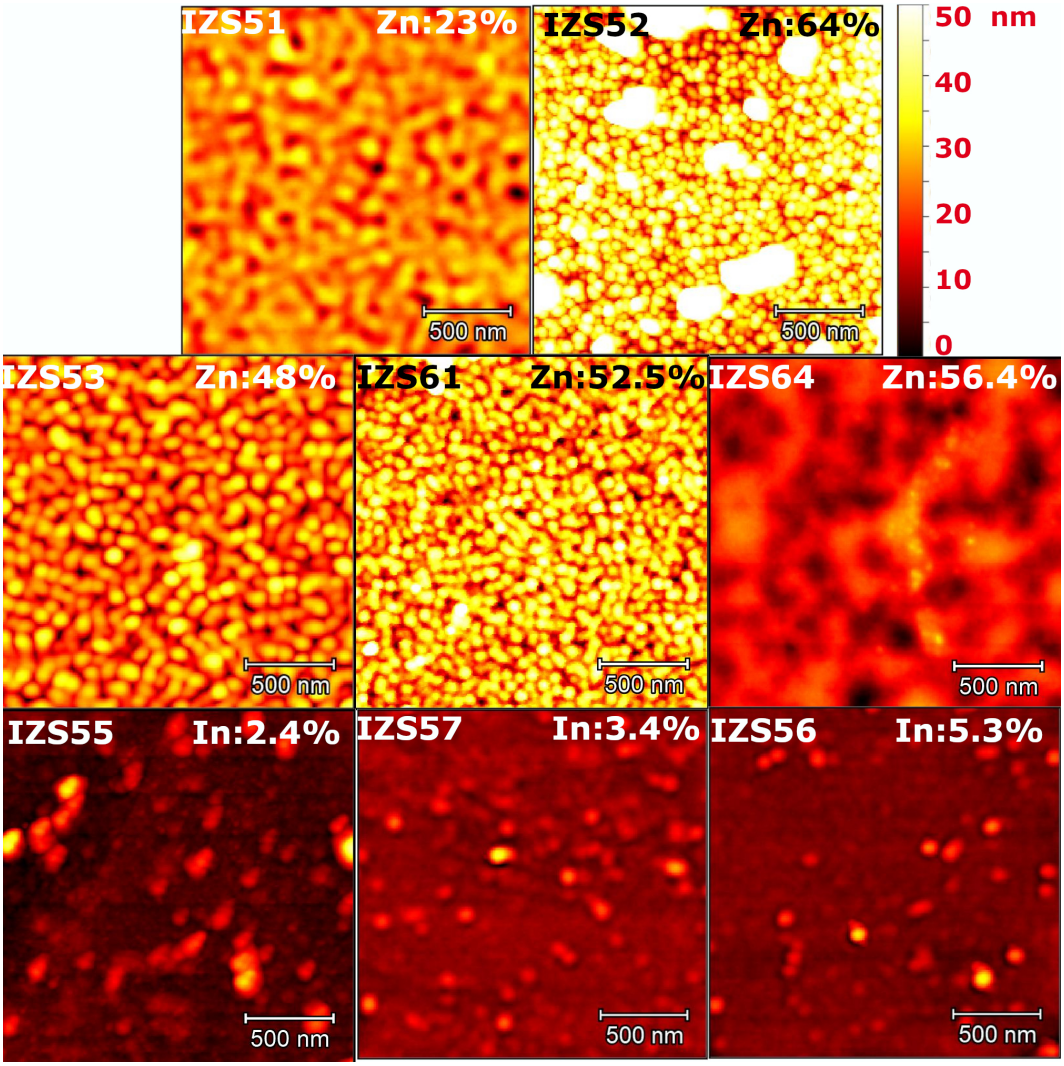


Figure 5.6: AFM topographs surface scaled to the same vertical and horizontal dimensions. The images are $2\mu$m $\times$ $2\mu$m, and the brightness level was adjusted to be from 0 to 50 nm. The first row contains the Zn and Sb-rich samples, the middle row shows the three films near stoichiometry, and the last row contains In-doped samples.

samples, but hardly changes for nearly stoichiometric samples. Mobility decreases at 300 K for off-stoichiometric samples but changes little for nearly stoichiometric ones. In semiconductors, the carrier concentration depends on $\triangle E$ according to the Arrhenius equation $n = n_o e^{-\triangle E/K_B T}$, where $n_o$ is constant. If $\triangle E$ is small, more carriers will be excited when the temperature increases, and $n$ will be more dependent on the temperature. This is likely the case in our off-stoichiometric samples, they have smaller $\triangle E$ in the

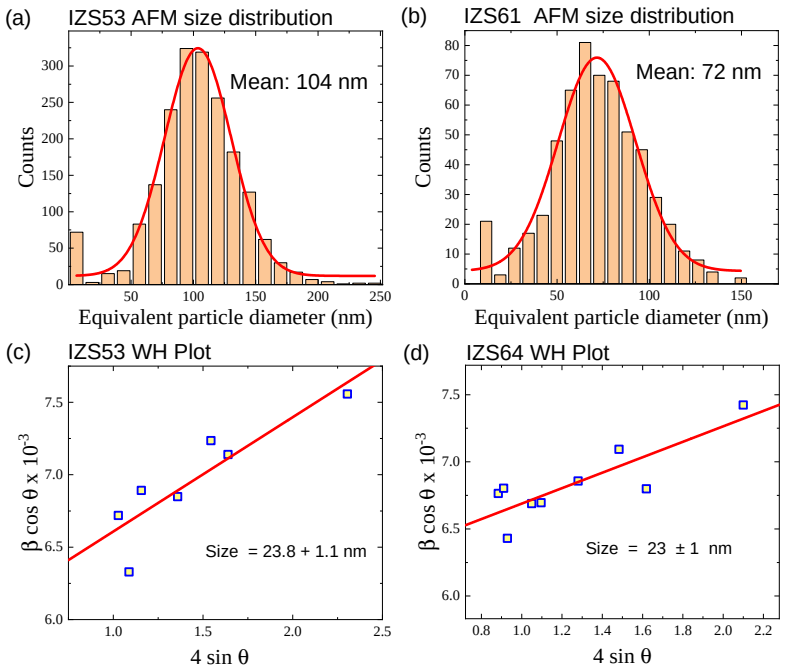


Figure 5.7: Particle diameter histograms for near-stoichiometric ZnSb films(a, b) from AFM topographs. Panels (c, d) show Williamson-Hall plots. Panels (a,c) are from the same single-phase ZnSb sample. Panels (b) and (d) are for mixed-phase and single-phase $Zn_4Sb_3$ samples respectively.

temperature range from 77 to 300 K. This might be attributed to the presence of more gap states in the off-stoichiometric samples, in which the carrier transition dominates. This dominance may have arisen because thermal energy in that temperature range (order of 10 meV) is much less than the optical band gap that represents band-to-band transition ( 0.3-1.1 eV, Section 5.2.4).

### 5.2.4 Optical band gap

For ZnSb samples grown on glass, absorption from the FTIR spectrum was acquired, and Tauc plots are presented in Figure 5.10. The optical transitions were quoted from both direct and indirect plots. In most cases, the transitions could be seen in both plots in the same area giving very close values. All indirect gaps obtained from a spectrum that strongly interfered with the direct transition's onset (most of them do) were omitted as discussed in Chapter 2.

Figure 5.11 gathers the reliable optical transitions seen from the FTIR spectrum of ZnSb films on glass (Figure 5.10). Undoped ZnSb films have two optical transition ranges,

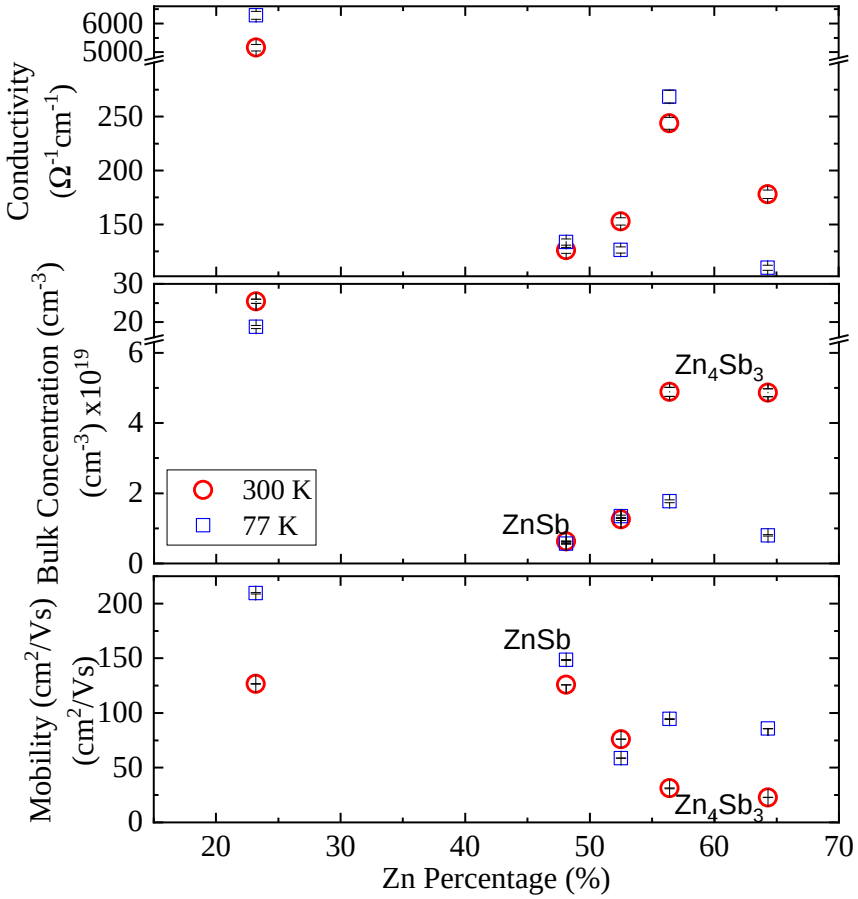


Figure 5.8: Electrical parameters (carrier concentration, mobility and conductivity) of ZnSb films on the glass as a function of their EDX composition. Measurements were taken at 300 K (red circles) and 77 K (blue squares). Scale breaks are applied to show the Sb-rich sample's data in the conductivity and concentration panels.

the low energy one (around the purple dashed line at 0.3 eV) and the fundamental one (around the green dashed line). The fundamental transition values could be correlated to the phases in each sample. Overall, these values increase by increasing the Zn percentage until they reach values around 1.07 eV for $Zn_4Sb_3$ films. Very Sb-rich sample (IZS51) has a direct gap around 0.69 eV, which could be attributed to the $\beta-Zn_8Sb_7$ phase dominant in this sample. This value is somewhat greater than the theoretically calculated direct band gap value (0.61 eV) based on the generalized gradient approximation (GGA) and the modified Becke Johnson (MBJ) potential [166], probably the 46% excess Sb that cause that deviation. It is worth noting that the theoretical calculations use some boundary conditions and ideal parameters that might affect their outputs such as assuming that

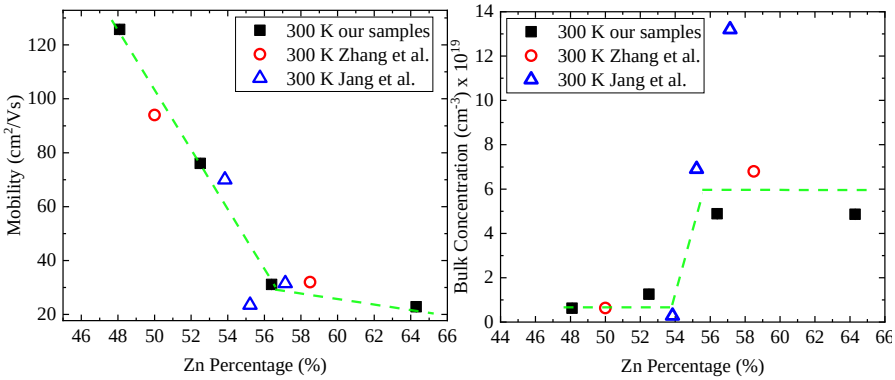


Figure 5.9: Electric parameters of ZnSb films grown on glass compared to Zhang et al. [164] and Jang et al. [165]. Green dashed lines are guides to the eye.

the temperature is 0 K. The direct gap of the ZnSb phase (0.9 eV, IZS53) is very close to the theoretically calculated direct band gap value (0.88 eV) [166]. For other samples containing either nominally pure $Zn_4Sb_3$ phase or a mixture with other phases, the optical gap lies around 1.07 eV (from 1.03 eV to 1.14 eV). These values are close to 1-1.2 eV reported for $\beta$ $Zn_4Sb_3$ [167–169].

The low energy transitions (0.26-0.36 eV) in undoped samples may be related to ZnSb polycrystalline compounds [149]; it is usually reported from the temperature-dependent electrical data. For example, this range of energies was observed for the ZnSb sample (0.35 eV) and $Zn_4Sb_3$/ZnSb mixed samples [164]. Those transitions are not seen in the In-doped films, but new transitions (0.49-0.66 eV) appeared instead, as do the Zn-rich sample (IZS52). Samples with 3.4-5.3 % In (IZS57 and IZS56) have transitions at 0.87 and 0.85 eV (marked with blue edges), are 0.03-0.05 eV less than nominal ZnSb phase sample's gap (0.9 eV, IZS53), though originated from the In gap states in that phase.

Another possible interpretation for In-doped samples plots (panels f-h) is that their oscillatory feature resulted from thin film interference, not from different phases. In thin films, incident light rays may get reflected from both sides of the film and interfere forming constructive and destructive fringes [1] that overlap with transmission and reflection spectra. This is more likely to occur when photons are not absorbed by the film when their energy is below or near the band gap. The film's roughness is another factor as smooth surfaces and interfaces reflect the light better, while rough ones decrease the thin film interference effect [170]. This is probably the case with our In-doped films. Assuming that this effect is dominant in those films, the band gap could be determined by extrapolating the high-energy fitting line to the energy axis. In this case, the band

gap values would be around 0.04-0.06 eV less than those mentioned earlier.

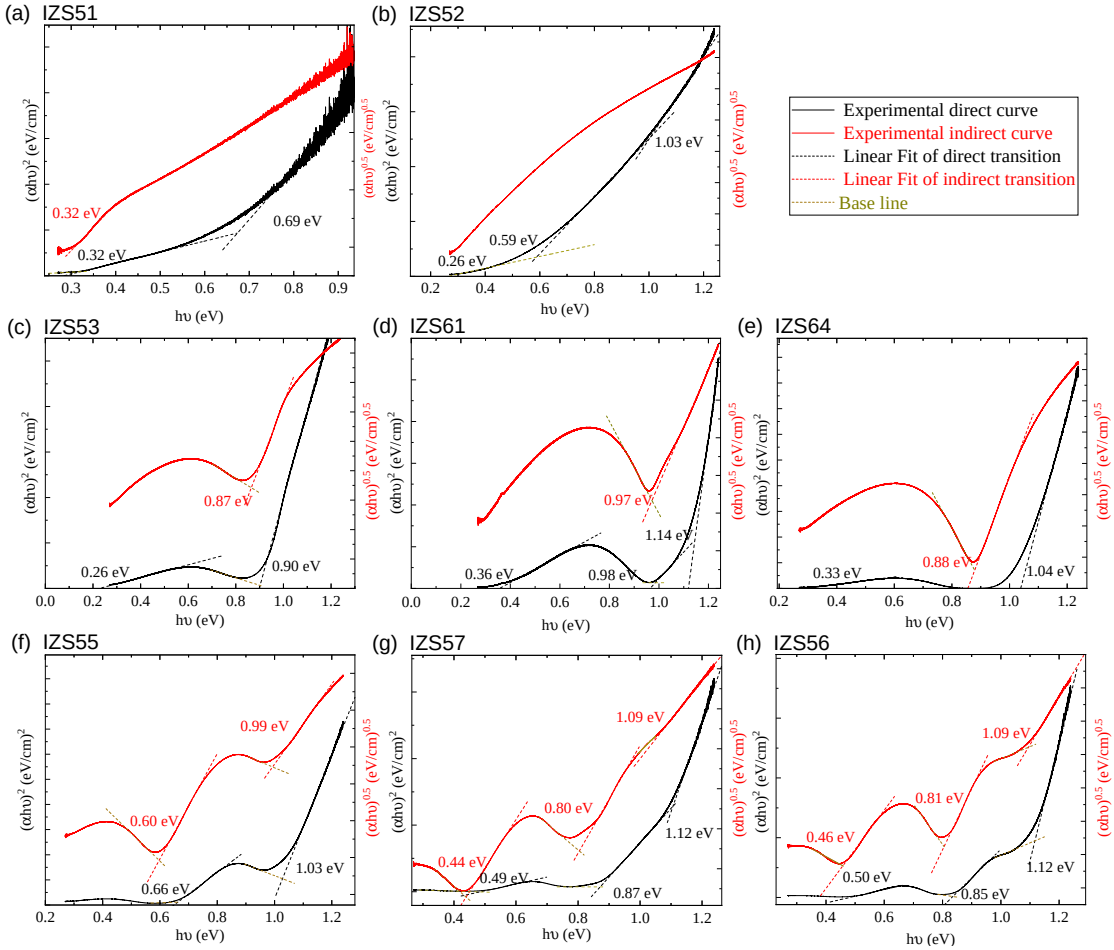


Figure 5.10: FTIR spectrum of ZnSb films on glass. Tauc plots for direct (in black) and indirect (in red) optical transitions were obtained using the absorption data.

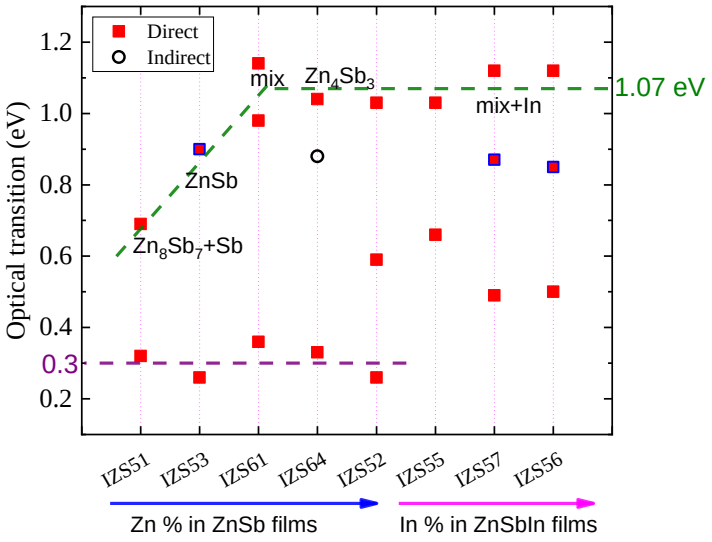


Figure 5.11: Map of the direct and indirect optical transitions from FTIR spectrum of ZnSb films on glass samples, extracted from Figure 5.10. Pure ZnSb films are ordered according to Zn % content, while In-doped films are ordered with their In percentage. The green dashed line is an eye guide to the fundamental transitions in the samples and the purple one is at 0.3 eV.

## 5.3 Film flexibility test

The durability of ZnSb films grown on Kapton was examined by testing their electrical and optical properties before and after bending them for $10^4$ cycles. A linear actuator controlled by LabView was set up to repeatedly bend batches of films on Kapton, as shown in Figure 5.12. As it is free bending, and no constant radius of curvature is maintained, the minimum radius of curvature $r$ was estimated graphically to be around 13.6 mm [Figure 5.12 (c)]. Using this value with 0.05 mm as the Kapton substrate thickness $h$, the maximum bending-induced surface strain $\varepsilon_b(r)$ could be calculated [171]:

$$\varepsilon_b(r) = \frac{h}{2r + h} \approx 0.18\%$$

### 5.3.1 Hall measurements of flexible films

Hall parameters of ZnSb films on Kapton were measured before and after $10^4$ bending cycles. IZS53 was tested after $10^5$ cycles additionally. The values of carrier concentration

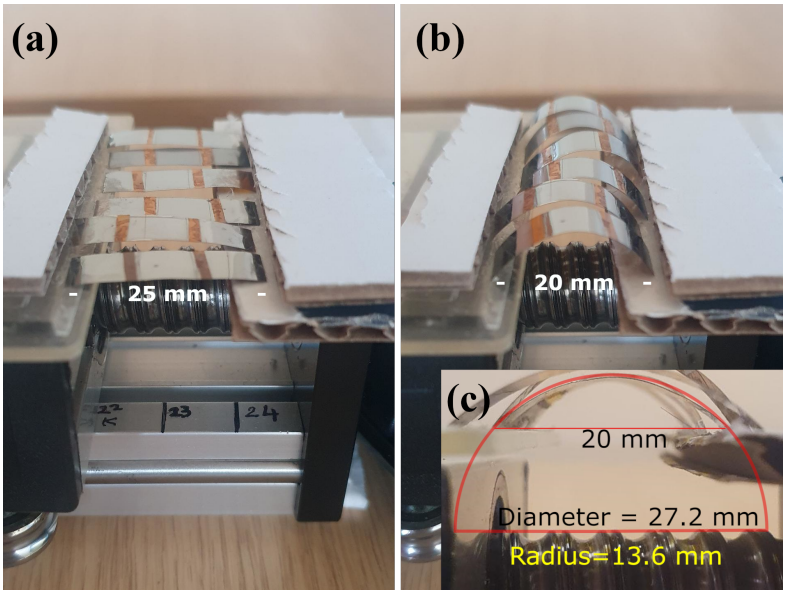


Figure 5.12: Kapton samples during the flexibility test, moving from (a) relaxed position to (b) bent position. (c) illustrates the maximum compression and resultant radius of curvature.

and mobility of the flexible films lie in the same range as those grown on glass. Figure 5.13 (a) shows the values of the bulk carrier concentration of the undoped (left) and In-doped (right) ZnSb flexible films labelled by their EDX compositions. One can notice also that, after applying $10^4$ bending cycles, these values stay very close to their original values. For the most highly doped sample (6.8% In) it was possible to obtain Hall mobility and conductance before bending but not after. This indicates that repeated flexing has altered the behaviour of the In within the polycrystalline structure. We speculate that this is caused by the mobility of excess In at grain boundaries, but further study is needed to explore this effect and its origin. Figure 5.13 (b) shows the carrier concentration and mobility dependence on the In percentage. As the In concentration increases, the mobility falls monotonically to reach about one-tenth of its value by 4% In. In general, the carrier concentration increases by increasing the indium percentage (but the Zn-to-Sb ratio can affect this value as in sample IZS58, which has a higher value than IZS56). To highlight the effect of bending alone, the electrical parameters of the bent samples were normalized to their original values before bending. Figure 5.14 shows that, after bending, the electrical parameters stayed very stable, within 7 % of the original values (the change could be from the repeated measurements, not from the bending). This reflects the suitability of the undoped ZnSb and up to 5 % In-doped films

for the flexible device application. In addition, the stability of the electrical parameters after flexing these films (radius of curvature, $r$ is down to 1.36 cm ) advantages the LP-PVD in fabricating flexible ZnSb films with 0.1-0.3 $\mu$m thickness over the screen-printing technique. In the latter, the resistance of 26 $\mu$m thick module rose sharply when bent below a 7-cm radius of curvature [159].

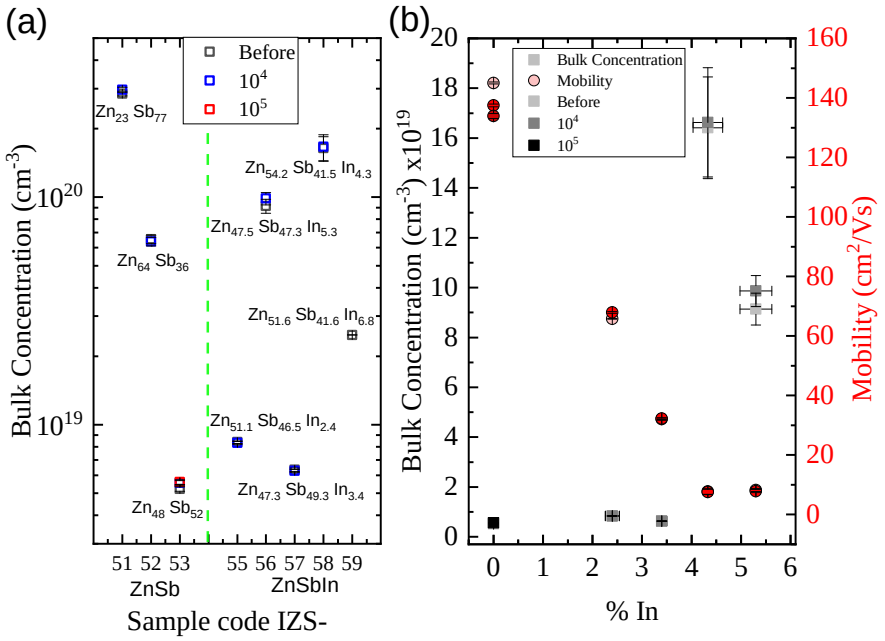


Figure 5.13: Electrical parameters dependence on Kapton films' composition before and after bending cycles.

It is important to highlight that the above-mentioned stability is observed by regular controlled bending only; twisting these films manually has a detrimental impact on their conductivity. In a separate experiment, the undoped ZnSb sample (IZS53) and the In-doped (IZS55) were tested under torsional stress, which is much harsher. Figure 5.15(a) shows the progressive degradation in samples' conductivity when being twisted manually (panels b and c). The conductivity in both films decreased by twisting, quicker in the In-doped sample than in the undoped one. This is likely from the disorder accompanied by In-doping. In conclusion, ZnSb films can endure gentle bending, even with $10^4$ cycles, but degrade very quickly with tens of manual twisting cycles.

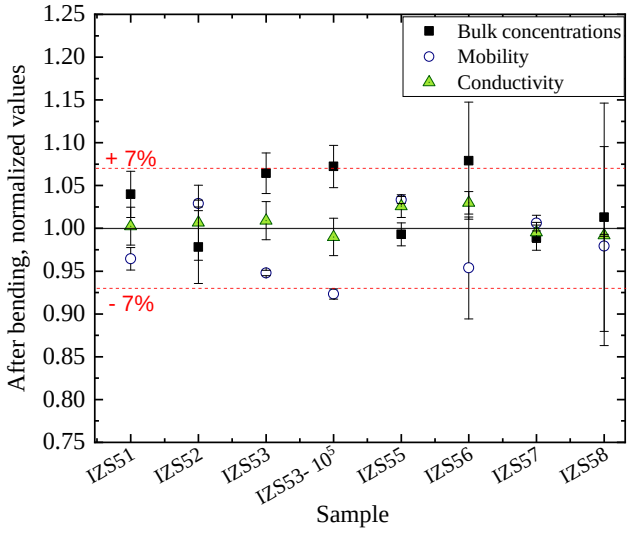


Figure 5.14: Electrical parameters of the flexed samples, normalized to their values before bending. The horizontal lines are ±7% from unity.

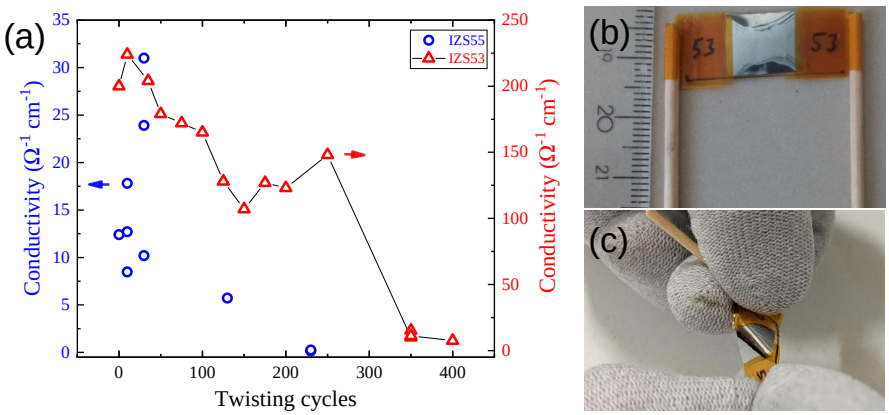


Figure 5.15: The conductivity of two ZnSb samples grown on Kapton under multiple manual twisting cycles. Panel (a) shows the undoped IZS53 sample in red triangles with the right scale and the In-doped IZS55 sample in blue circles with the left scale. Panels (b-c) show one sample before and during the twisting, courtesy of Dr Gavin Bell [104].

### 5.3.2 Band gap of flexible films

Direct and indirect Tauc plots were compared for all the films before and after bending. The Kapton sheets caused strong interference fringes that overlap with the absorption spectrum in the NIR range. The data were smoothed using a fast Fourier transform filter

which easily removes the interference fringes without producing spectral artefacts. Figure 5.16 shows the smoothed direct and indirect Tauc plots of the flexible films before and after bending. The plots show clearly the matching between the data obtained before and after flexing the films. The determined gap values of the bent films fall within 0.02 eV their values before bending. Moreover, these values are very close to the gap values of the same films grown on the glass as illustrated in Figure 5.10. That suggests that using different substrates (glass and Kapton) does not have much impact on the optical properties of the grown films. Overall, growing ZnSb films on a flexible substrate such as Kapton gives the same optical properties as it does when grown on glass, even after flexing them for $10^4$ cycles.

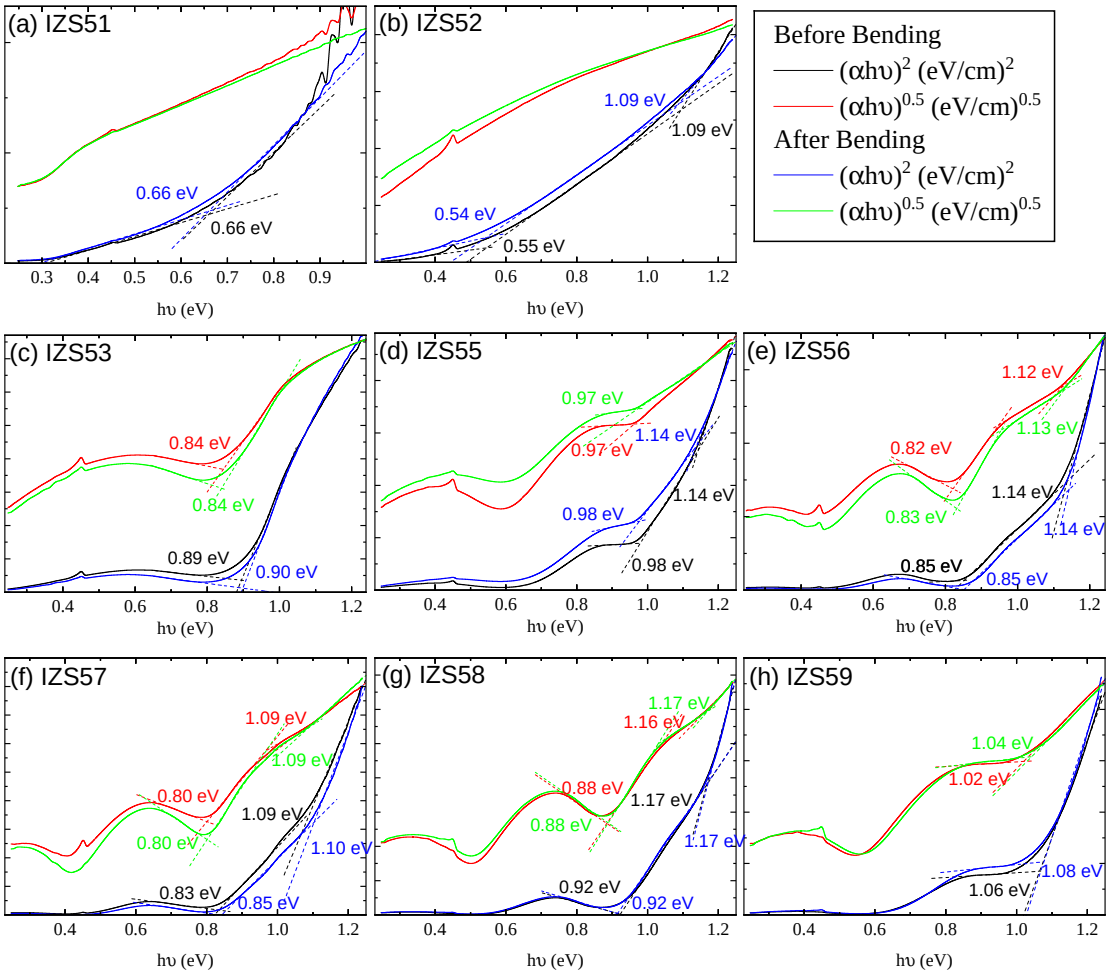


Figure 5.16: Tauc plots of ZnSb films on Kapton before and after bending. The data was obtained by smoothing the original absorbance data with an FFT filter. The y-axes are scaled differently. The solid lines represent direct and indirect Tauc plots and are coloured differently as explained in the legends, while dashed lines represent the linear fittings of the data segments of the same colour. The small peak at 0.45 eV comes from the instrumental setup, not from the films.

## 5.4 Thermoelectric measurements

The thermoelectric power factor of the ZnSb films grown on Kapton was determined using the Seebeck coefficient/ electric resistance measurement system ZEM-3. The power factor was measured up to 400 K to avoid altering the composition or the structure of the films, and it is the expected working temperature range for flexible TE devices.

The thermoelectric parameters of the flexible ZnSb films showed great dependence on its In doping percentage. Figure 5.17 shows the dependence of (a) the Seebeck coefficient, (b) electrical conductivity, and (c) the power factor of the investigated films on the temperature while heating and cooling the samples from 35°C to 123°C. In general, the dependence on the samples' composition is more dominant than the operating temperature in that range. The undoped ZnSb film (IZS53) showed the highest PF value at the studied temperature range as it has high Seebeck coefficient and conductivity values, while sample IZS58 (4.3 %In) has the lowest values. This could be attributed to the decrease in conductivity as the mobility decreases with more In doping (Figure 5.13). However, the In-rich sample, IZS56 (5.3 %In) has the highest conductivity, probably owing to its highest carrier concentration value (refer to Figure 5.13) as Zn/Sb ratio is different. Turning now to the stability of the samples, most samples give close electrical conductivity values during the heating and cooling cycles, but moderately In-doped (2.4-3.4 %In) samples, IZS55 and IZS57 showed conductivity dependence on their thermal history. When heated, the conductivity decreases gradually by about 20% of its value, it then remains constant during the following cooling cycle. The reason is not known as all the samples have been annealed at 150-200 $^{o}$C during the preparation to turn them crystalline as explained earlier, the Seebeck coefficient did not change though. This trend is believed to be from the conductive paste applied in the measurements, not from a phase transition. However, these two In-doped samples have high PF values reaching 836 $\mu$W/m.K$^2$ at 123 $^{o}$C (i.e. below 400 K). Panel (d) in Figure 5.17 shows the PF values as first measured at 37 $^{o}$C (in black) and the maximum value in our temperature range (in red), with those obtained by Zheng et al. [160]. Overall, the undoped sample has the highest PF value 1049 $\mu$W/m.K$^2$. By introducing the In doping, a steep decline occurs in the PF to become 836 $\mu$W/m.K$^2$ (between 2.4 and 3.4%In). Those $2.4-3.4\%$ In-doped samples are very close in their maximum PF values to those prepared by Zheng et al. [160] by co-sputtering ZnSb on a precursor In layer followed by annealing to obtain same In percentage ($2.3-3.7\%$). Our undoped ZnSb sample has a higher PF value than Zheng et al.'s; this is probably related to the Zn/Sb ratio. But both show a similar drop in the PF values after 4% In, the PF in our samples drops to less than 200 $\mu$W/m.K$^2$.

Table 5.3 highlights the PF values of our undoped and $2.4-3.4\%$ In-doped ZnSb films with the recent values reported in the literature. The table includes bulk and thin film samples prepared by various methods. What stands out in the table is that our undoped ZnSb sample (IZS53) has the highest PF for all undoped polycrystalline thin films (1049 $\mu$W/m.K$^2$). The RF sputtered ZnSb film on Polyimide that was studied in 2014 by Fan et al. [156] has a very close PF value (970 $\mu$W/m.K$^2$). It is also not far from bulk samples' values (1213-1238 $\mu$W/m.K$^2$) [165, 172]. In short, the polycrystalline ZnSb films with a 48/52 Zn-to-Sb ratio grown on Polyimide (or Kapton) are very promising for thermoelectric applications due to their high PF values. However, In doping is negatively impacting the PF values especially if it is higher than 4%. In this study, we were not able to measure the thermal conductivity of the studied films although it would be valuable to observe if low In doping (below 4%) suppresses the thermal conductivity of the films, resulting in higher ZT values. On the other hand, some other dopant like Ti could be a better choice as it has the highest ZT and PF values below 400 K [172].

Table 5.3: Thermoelectric parameters of various doped and undoped Zn-Sb bulk and film samples from the literature as compared to our samples. Samples are ordered from the highest PF values (below 400 K) to the lowest. The thermoelectric figure of merit (ZT) values under 400 K and the maximum reported power factor beyond that range are also included. the PF units values in $\mu$Wm$^{-1}$K$^{-2}$. The reference column includes the surname of the first author with the date of publication as follows: Xiong 2013 [172], Zheng 2017 E [157], Sun 2012 [173], Jang 2007 [165], Fan 2014 [156], Zheng 2017 H [160], Moghaddam 2019 [161], Zhang 2003 [164], Hsu 2021 [174], Wang 2020 [162] and Lee 2011 [159].

| Reference | Sample form/ preparation technique | Doping | $PF_{T<400\ K}$ | $PF_{Maximum}$ | $ZT_{T<400\ K}$ | Composition |
|---|---|---|---|---|---|---|
| **Xiong 2013** | Bulk hot-pressed samples | Ag | 2100 | 2544 (470 K) | 0.65 | $Zn_{0.998}Ag_{0.002}Sb$ |
| **Zheng 2017 E** | Co-sputtered film on flexible Kapton | Ti | 1704 | 3590 (523 k) | - | ZnSb-Ti(2.4%) |
| **Sun 2012** | Textured cosputtered film on fused glass | - | 1350 | 1700 (550 K) | 0.5 | ZnSb (211) |
| **Jang 2007** | Bulk vacuum melting ingot | - | 1238 | | 0.55 | $Zn_{4-x}Sb_3$ with x=0 |
| **Xiong 2013** | Bulk hot-pressed samples | - | 1213 | 1363 (470 K) | 0.35 | ZnSb |
| **This study (IZS53)** | Film by LP-PVD on flexible a Kapton | - | 1049 | | - | $Zn_{48}\ Sb_{52}$ |
| **Fan 2014** | RF sputtered film on Polyimide | - | 970 | 2350 (500 K) | - | $Zn_{48}\ Sb_{52}$ |
| **Zheng 2017 H** | Co-sputtered ZnSb film on In layer on glass | In | 930 | 1150 (590) | - | ZnSb-In (2.3-3.7%) |
| **Moghaddam 2019** | Compressed ball-milled composites | Ge | 870 | 1680 (600K) | 0.35 | $Zn_{1.1-x}Ge_xSb$ |
| **This study (IZS55, 57)** | Film by LP-PVD on flexible Kapton | In | 836 | | - | ZnSb-In (2.4-3.4%) |
| **Zhang 2003** | Bulk hot-pressed samples | - | 660 | 1016 (675 K) | 0.26 | $\beta$-$Zn_4Sb_3$ |
| **Zheng 2017 H** | Co-sputtered ZnSb film on glass | - | 593 | 797 (590 K) | - | ZnSb |
| **Hsu 2021** | Film by electron beam evaporation | - | 314 | 1280 (550 K) | - | $Zn_4Sb_3$ + ZnSb |
| **Wang 2020** | Cosputtered films on quartz and $SiO_2$/Si | Bi | - | 3500 ( 793 K) | - | Bi-doped $Zn_2Sb_3$ |
| **Lee 2011** | Screen-printed film on flexible $SiO_2$/Si | - | - | 1060 (850 K) | - | ZnSb |

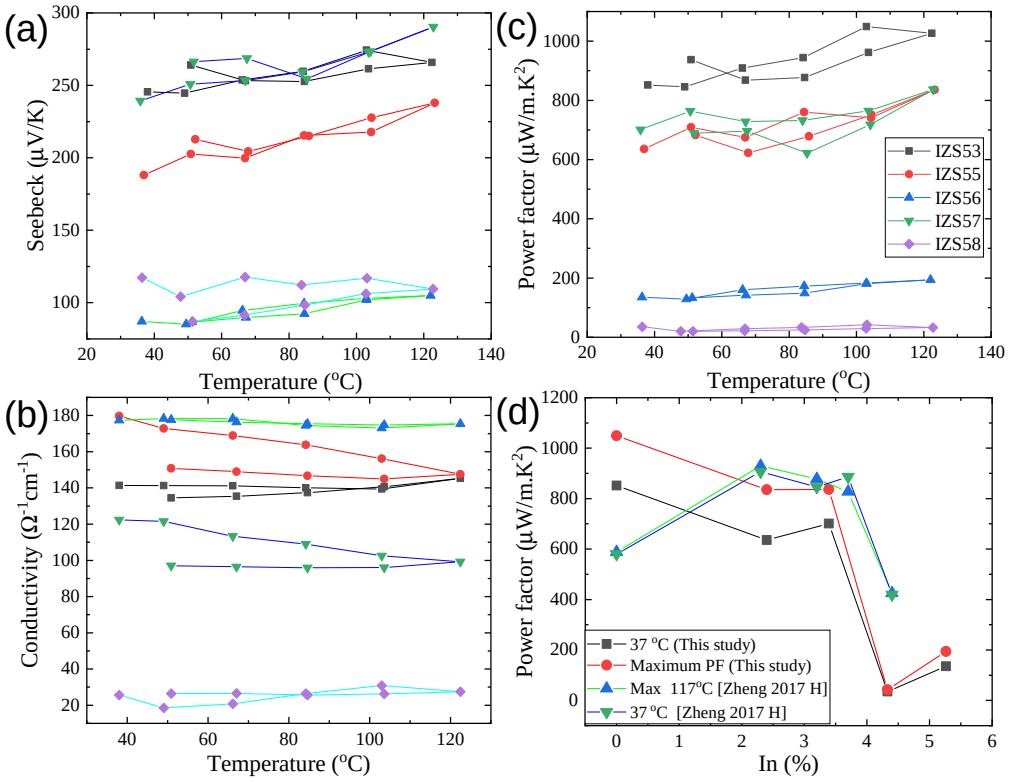


Figure 5.17: The thermoelectric parameters of the films grown on Kapton as a function of the operating temperature, (a) Seebeck coefficient, (b) electrical conductivity and (c) power factor. Panel (d) is the power factor of our films with reference [160] as a function of their In percentage when they were first measured around 37°C and the maximum PF value measured up to 123°C.

## 5.5 Conclusion

ZnSb thin films were grown on glass and Kapton substrates using the LP-PVD technique. Structural, electrical and optical data were discussed for undoped and In-doped films. New experimental optical band gaps were determined for ZnSb and In-doped ZnSb thin films, which was consistent with the published experimental values and theoretical calculations. ZnSb films grown on Kapton have similar electrical and optical parameters as those deposited on glass in the same experiment. This means that films that were grown on flexible Kapton behave as those grown on a solid substrate like glass. In addition, those flexible films were electrically and optically stable after $10^4$ bending cycles. This suggests the feasibility of ZnSb thin films for flexible electronics and wearable device applications. However, ZnSb films degraded when it was twisted manually for tens of

cycles. The thermoelectric power factor of the ZnSb film was high when compared to other undoped polycrystalline thin films below 400 K. In-doping does not improve the PF as other doping elements in the literature.

# Chapter 6

# Sb Thin Films

Films of a few layers of Sb and monolayer (antimonene) attracted a lot of attention recently because of their strong spin-orbit coupling behaviour [175]. In addition, the Sb flux or layers can play important roles during the growth of other compounds. For example, during the growth of InAs nanowires, it might be used as a surfactant to accelerate lateral growth while limiting axial growth [176]. It might also be used for Bi-based devices as a buffer layer to increase their mechanical resilience and electrical and magnetic performance [177]. As a template layer, Sb yields better quality GaSb epitaxial films on Si(111) substrates with better morphology and fewer stacking faults [178, 179]. Therefore, investigating pure Sb films on various surfaces and with different thicknesses is important to employ it effectively. Among these surfaces, InAs(111) allows direct growth with no need for a buffer layer as it has a small lattice mismatch with Sb(111) [180]. In this recent article from our group, the structure of ultra-thin films of Sb on InAs(111)B (up to 7nm) was investigated using in situ surface X-ray diffraction (SXRD) showing coherently strained Sb layers with atomic intermixing around the interface [180].

On the other hand, the measurement of the work function can serve as a new technological approach toward material analysis and design [181]. Different material properties (e.g. mechanical properties) could be easily related to the work function as these properties are more or less correlated to the atomic bond strength [181, 182]. Studying the work function of Sb could be important in different cases. For example, Sb could serve as a novel low-resistance contact interface for advanced 2D devices because of its thermal stability over other semimetals such as Bi and Sn [183]. Or, it could be also used as a dopant to enhance or extend the functionality of the $TiO_2$ for photocatalytic and photoelectrochemical cells applications [184–186].

In the present work, Sb films were grown on InAs(111)B and chemically treated

glass. The structure, morphology, electrical, optical properties and work function of these films were investigated as outlined in Table 6.1.

Table 6.1: Sb samples and the techniques used to characterise them

| Sample | Substrate | Structure | Morphology | Thickness | Composition | Electrical | Work function | Optical |
|---|---|---|---|---|---|---|---|---|
| **S663** | InAs(111)B | RHEED | AFM | Calibration | XPS | ... | KP | ... |
| **S685** | Glass | GIXRD | AFM | AFM | ... | Van der Pauw | KP | FTIR |

## 6.1 Epitaxial Sb film on InAs (111)B

In this section, Sb thin films were grown epitaxially on InAs (111) B wafer. Samples in the thickness range of 3-50 nm were grown at a fixed growth rate (see Appendix B). The analysis focused on one of these samples (S663), will be compared with another Sb film grown on glass (Section 6.2), as listed in Table 6.1.

### 6.1.1 Growth

Sb films were grown inside vacuum system 1(Madge). The epitaxial film was grown on InAs (111)B substrate. Prior to the deposition, the substrate was degassed at 300 °C for more than one hour. Its surface was then sputtered by 40 mA 0.5-kV-accelerated $Ar^+$ ions for 16 mins to remove contaminants and the oxide layer. This was followed by one-hour annealing at 430 °C to relax the surface after sputtering. To ensure a high-quality surface (atomically clean), RHEED was observed after the annealing process. Figure 6.1 shows RHEED pattern of the prepared InAs(111)B surface in two directions, $[1\bar{1}0]$ (a) and $[1\bar{2}1]$ (b). The streaky well-defined lines feature indicates the flat crystallographically ordered surface of the substrate with no 3D islands, while Kikuchi lines illustrate the high crystal quality of the near-surface region. The (1×1) surface shows that there is no reconstruction on the InAs (111)B surface, which agrees with [180]. The substrate temperature was kept at 200 °C during the growth to obtain epitaxial single crystal Sb film, as room-temperature depositions did not show any RHEED patterns in our initial experiments. Similar to what Mousley et al. have concluded [180], epitaxial highly crystalline films that emerged after annealing at 210 °C in the vacuum cannot be produced by room temperature deposition. The Sb film was grown on that clean surface for 30 mins with $2.1\times10^{-7}$ mbar flux pressure (equivalent to 1.4 nm/min) to reach nominally 43 nm thickness as shown in the calibration curve Figure B.1 (Appendix B). After deposition, similar RHEED patterns were observed at the same substrate

angles reflecting the epitaxial growth of the Sb single-phase film (Figure 6.1 (c), (d)). Each streak in panel (d) is split into two streaks with a small angle ($\approx 6^\circ \pm 2^\circ$). This reflects that the Sb surface is not completely flat and facets are present. These facets produce two diffraction lines, one from each side, with an angle $2\theta$ between them, where $\theta$ is the angle between the facet and the substrate's plane ($\approx 3^\circ \pm 1^\circ$).

The in-plane spacing of each direction ($a$) was calculated from the equation, $a = \frac{2\pi L}{Ks}$ (see Methodology) using the streaks displacement ($s$) in each RHEED pattern (for the substrate and the grown Sb film). These values were compared to the experimental values of bulk Sb and InAs as illustrated in Figure 6.2. Panel (a) represents InAs (111)B surface and its in-plane distance for $[1\bar{1}0]$ (green) and $[1\bar{2}1]$ (black) directions in the top and side views (space group: F$\bar{4}$3m, PDF 00-015-0869 [82]). Panel (b) shows a similar illustration for the Sb (001) surface and its corresponding in-plane distance for [010] (green) and $[\bar{1}10]$ (black) directions (space group: R$\bar{3}$m, PDF 00-005-0562 [82]). The crystallographic notation Sb(001) in our analysis is shortened from the hexagonal Sb(0001), which is equivalent to the cubic Sb(111) notation found in the literature [180]. Panel (c) is a table comparing between ($a$) values as determined from RHEED patterns (Figure 6.1) and the .cif models illustrated in (a,b) Figure 6.2. Note, the ($a$) value from InAs .cif model for the $[1\bar{1}0]$ direction was used to calibrate the camera length ($L$) in the equation. For the Sb grown film, the determined ($a$) values from RHEED match with the bulk ($a$) values of the .cif model within 0.1% difference as tabulated in panel(c). This suggests that the 43-nm-thick Sb film's surface is fully relaxed. This agrees with the calculated Matthews-Blakeslee critical thickness (18 nm) of Sb to form an edge dislocation when grown on InAs(111) substrate [180].

### 6.1.2 AFM

Figure 6.3 (a) is the AFM topograph of Sb on the InAs sample (S663). The surface has well-defined pyramids with 1.6 nm roughness (RMS). Each pyramid is formed of stacked equilateral triangular facets with sides ranging in length from 150 nm to 550 nm. In addition, the pyramids are all directed in the same direction showing 3-fold rotational symmetry instead of 6-fold rotational symmetry. In reference [180], a small degree of twining (rotational twin domains) was found in ultra-thin films, but in thicker films three-fold symmetry was observed by AFM, agreeing with the results shown here. Panel (c) shows the line profile of six arbitrary pyramids, with heights *(h)* around 4-5 nm and 300-500 nm bases. The thickness of the film (43 nm) is much bigger than the pyramids' heights suggesting that the substrate is fully covered by a uniform-thickness film that

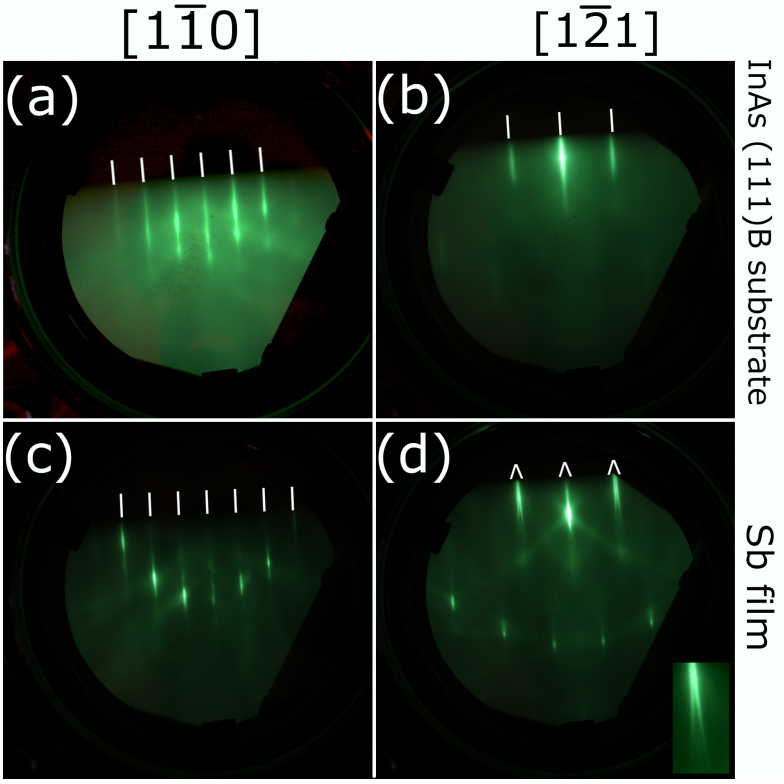


Figure 6.1: RHEED patterns of Sb on InAs(111)B (S663). Panels (a,b) are of the InAs (111)B ready-substrate along [1$\bar{1}$0] and [1$\bar{2}$1] directions respectively. Panels (c,d) are the Sb film along the same substrate's directions. The inset in panel (d) shows one magnified streak.

has dense shallow pyramids on its surface. The pyramids' facets make different angles ($\theta$) with the substrate's plane, where ($\theta = tan^{-1}(h/x)$) and $x$ is the length demonstrated in the figure. Those angles vary from 0.6° (i.e. profile 1) to 3.8° (i.e. profile 4), those values agree with ($\theta$) values determined from RHEED patterns ($\theta \approx 3° \pm 1°$ ).

After annealing the sample at 200 °C in nitrogen, some spotty patches started to appear in the AFM scans. Panel (b) shows the AFM topograph after 3-hour annealing with some spots marked by dotted circles. To understand the origin of these spots, the film was scanned by XPS. The analysis reveals the presence of In peaks and absence of As peaks (Figure C.1(a) in Appendix C) meaning that In atoms were segregated to the surface during the annealing process. As the In melting point is less than 200 °C (156.6 °C), these In atoms in their liquid phase accumulated to form such agglomerations on the surface driven by its surface tension force. The quantitative analysis of Sb and In components shows 18.6 % In and 81.4 % Sb. Kojima et al. reported the diffusion of Cu

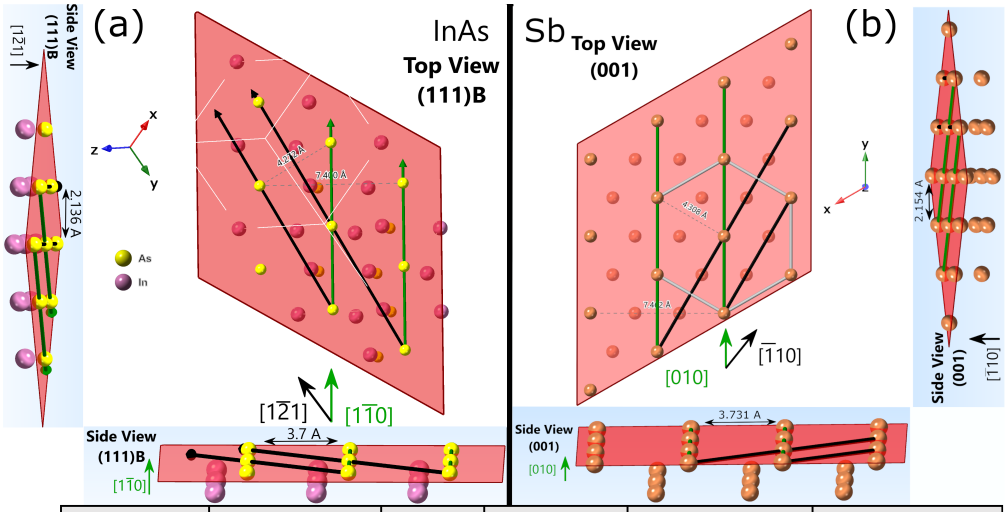


(c)

| Surface Plane | RHEED direction | $s$ (mm) | $a$ (A) (RHEED) | $a$ (A) (.cif model) | Reference |
|---|---|---|---|---|---|
| InAs (111)B | [1$\bar{1}$0] | 6.95 | -- | 3.7 | PDF 00-015-0869 |
| | [1$\bar{2}$1] | 12.04 | 2.137 | 2.136 | |
| Sb (001) | [010] | 6.89 | 3.735 | 3.731 | PDF 00-005-0562 |
| | [$\bar{1}$10] | 11.94 | 2.156 | 2.154 | |

Figure 6.2: Illustration of the in-plane spacing $a$ along RHEED symmetry directions in (a) InAs(111)B and (b) Sb (001) surfaces using their experimental PDF.cif files [82] as tabulated in panel (c). $s$ is the streaks displacement in RHEED patterns, Figure 6.1. The illustration was done by CrystalMaker software.

atoms between (111) Sb film layers when heated at 300°C for one hour in a vacuum to grow $Cu_2Sb$ single crystals [187].

### 6.1.3 Work function

The In segregation to the surface affected the work function of the Sb films when annealed. Section 6.2.5 discusses the change in the work function with annealing as compared with another crystalline film grown on glass.

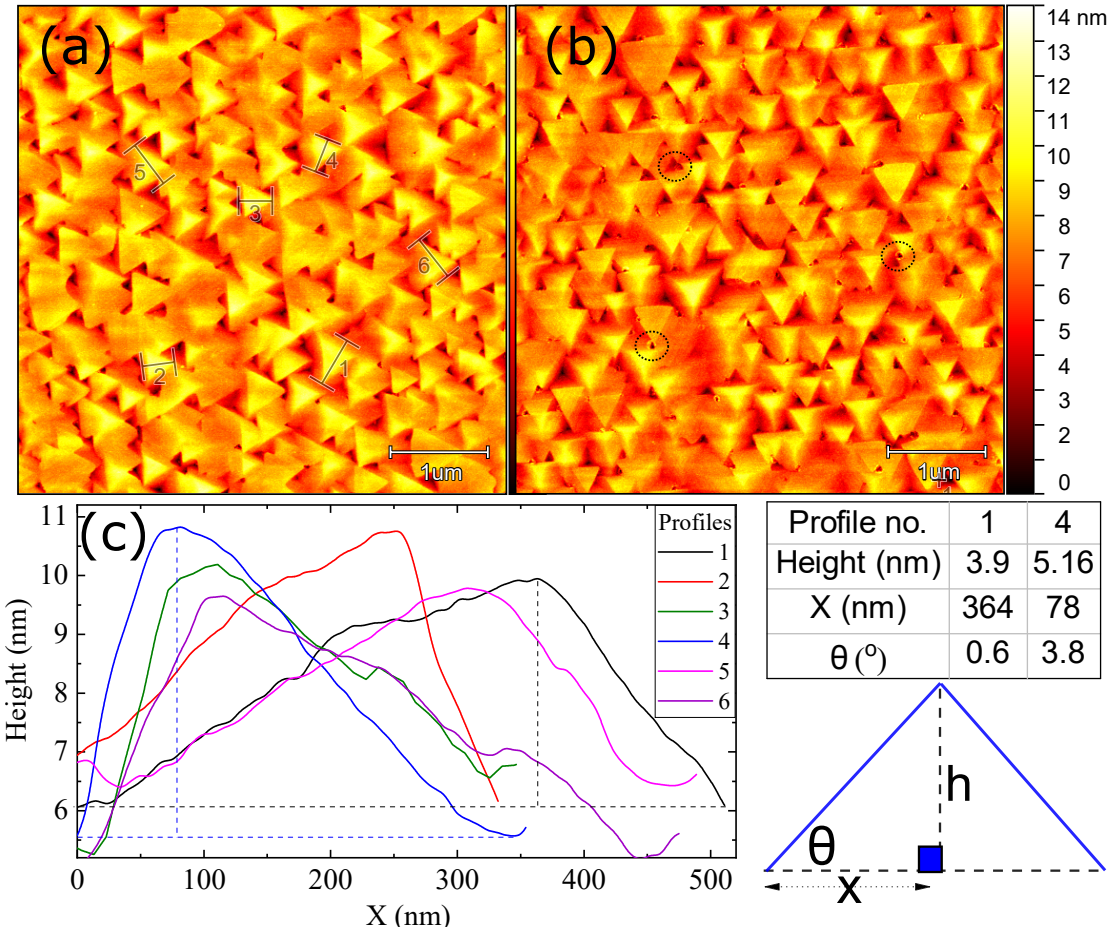


Figure 6.3: AFM topograph surface of sample S663 (Sb on InAs (111)B): (a) as prepared, (b) annealed at 200°C for 3 hours. Panel (c) is a line profile analysis of 6 arbitrary pyramids as marked in panel (a).

## 6.2 Sb film grown on glass

The sample was prepared by depositing Sb film on a chemically treated glass substrate. The chemical treatment is done by rinsing a glass slide in (0.03 %) diluted $SnCl_2$ solution for 15 min, followed by annealing in the air for 20 min at 200 °C to form tin oxide layer as described by Pejova et al. [64, 65]. The tin oxide layer is believed to improve the adhesion of the film to the glass surface and the nucleation in some chemical reactions [64, 65]. The treated substrate was moved to vacuum system 1(the same used with S663) and exposed to $7.3 \times 10^{-8}$ mbar of Sb flux at room temperature for 3 hours. After the deposition, the prepared film (S685) was kept in a nitrogen storage box for further analysis.

### 6.2.1 GIXRD

Figure 6.4 shows the GIXRD pattern of the as-prepared sample (S685). The presence of the diffraction peaks shows that the film is crystalline. Comparing the diffraction pattern peaks to a standard Sb card (PDF 04-007-7310) [82], only a few peaks appear (e.g. 003 at 23.7°), while the three strongest peaks (012, 104 and 110) can not be observed. This means that the sample has a strong preferred orientation in the 003 direction. This demonstrates the growth of crystalline Sb film with strong texture on glass at room temperature (after chemical treatment and with applying low Sb flux).

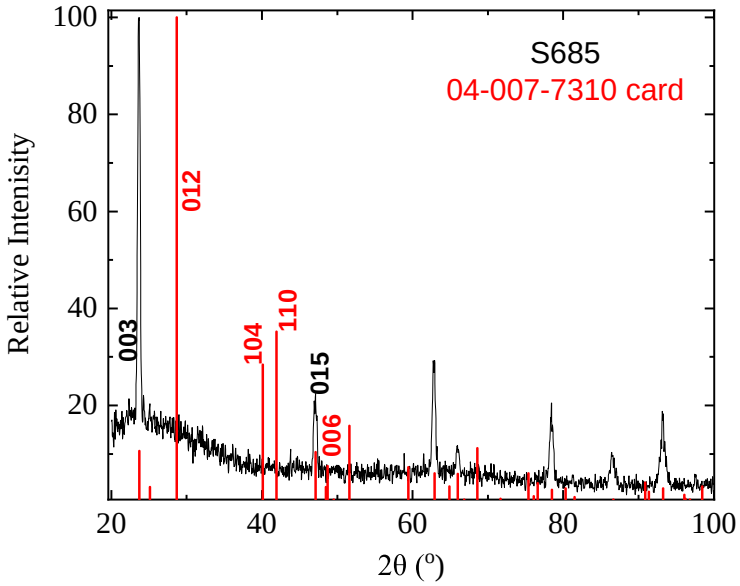


Figure 6.4: GIXRD of sample S685 (Sb film on glass). The red lines are from PDF 04-007-7310 card [82].

### 6.2.2 AFM

Figure 6.5 shows the surface topography of sample S685. The surface has a different topography than sample S663 (Figure 6.3), but we can identify some pyramids on the surface (in red circles). But, it does not have the 3-fold rotational symmetry observed in the Sb grown on InAs(111)B sample. There are also some areas where all the particles are aligned in the same direction (marked by arrows), while other areas are random. The surface roughness (RMS) is 2.9 nm, nearly double that of S663. After annealing,

no change in morphology was observed as that emerged from In segregation in the S663 sample. The thickness of the film was determined to be 150 ±7nm (Figure 6.6), much bigger than its roughness. The overall picture is a film with uniform thickness, and its surface is less ordered and rougher than that of the film grown on the InAs(111) substrate.

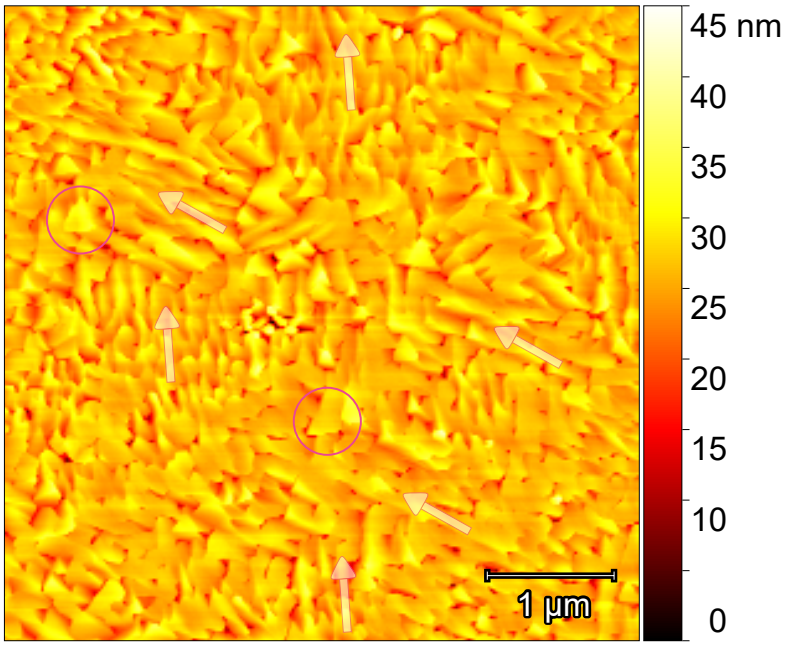


Figure 6.5: AFM topographs surface of sample S685 (Sb on glass). Arrows refer to the particles' orientation in some aligned areas. Red circles highlight some pyramids on the surface.

### 6.2.3 Hall measurements

The electrical parameters of the Sb film grown on glass are tabulated in Table 6.2. The as-prepared sample has high carrier concentration and high mobility that gives a high conductivity value at room temperature ($7.1 \times 10^3$ $\Omega^{-1}$ cm $^{-1}$), the conductivity value is higher than the 50 nm-thick Sb (111) films grown on GaAs (001) substrates ($< 1 \times 10^3$ $\Omega^{-1}$ cm $^{-1}$) [188]. The carrier concentration value of our thin film ($2.9 \times 10^{20}$ cm$^{-3}$) is higher than the reported value in the literature ($\approx 5.5 \times 10^{19}$ cm$^{-3}$ for both electrons and holes) [2, 189]. The reported value is measured using the de Haas−van Alphen effect for a crystalline Sb sample. It is known that carrier concentration and mobility values differ for narrow gap semiconductor and semimetal thin films than bulk crystals in their dependence on factors such as thickness, structure and substrate type [190]. As our carrier concentration value has been measured for a textured thin film on glass, this

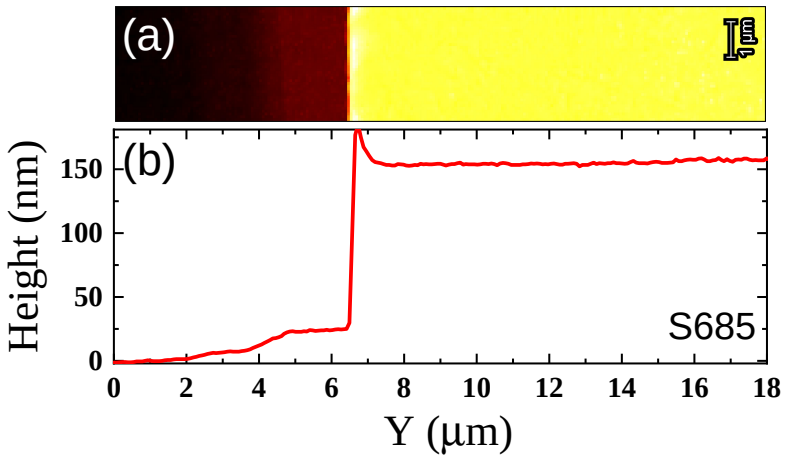


Figure 6.6: AFM thickness measurements of S685 (Sb on glass) film. (a) image of the scanned film edge using the light microscope attached to the AFM equipment and (b) the AFM line profile over that edge.

difference in value is justified. At 77 K, the conductivity increased due to higher carrier mobility. This indicates that the film's conducting behaviour is more metallic than a semiconductor in contrast to those grown on GaAs (001) substrates [188]. By annealing the film at 200 °C, the electrical parameters remain constant, which reflects the stability of the film at that temperature.

Table 6.2: Electrical parameters of sample S685 (Sb on glass) at room temperature (RT), 77 K, and at RT after being annealed at 200 °C for 1 and 3 hours.

| Sample (S685) | $N_B$ (x $10^{20}$ $cm^{-3}$) | $\mu$ ($cm^2$/VS) | $N_S$ (x $10^{15}$ $cm^{-2}$) | $\sigma$ (x $10^3$ $\Omega^{-1}cm^{-1}$) |
|---|---|---|---|---|
| As prepared (RT) | 2.9 | 156 | 4.3 | 7.1 |
| As prepared (77 K) | 3.0 | 246 | 4.5 | 11.7 |
| Annealed 1Hr, 200 °C (RT) | 2.8 | 141 | 4.2 | 6.3 |
| Annealed 3Hr, 200 °C (RT) | 2.9 | 136 | 4.3 | 6.2 |

### 6.2.4 FTIR

Antimony (like bismuth) is one of the semimetals with a negative indirect band gap and a finite direct band gap [191]. Here we try to experimentally determine this direct gap using the Tauc plot from the absorption data of the Sb film grown on glass (Sample S685). Figure 6.7 shows the direct Tauc plot of the sample, the inset magnifies the squared region. The data shows a curve of two linear segments that could be fitted by two intersecting straight lines. The first low-energy one intersects with the x-axis at

228 meV which represents the smallest direct optical transition in the samples (direct band gap). The second line intersects with it at 342 meV representing the value of the second smallest direct transition in the films. To understand these values, we look at the band structure of the bulk Sb to relate them to different proposed transitions. The band structure of the antimony has been studied using different models since 1966 [192–194]. The developed tight-binding model calculations done by Liu and Allen [4] considering a third neighbour and including spin-orbit coupling are very close to the experimental XPS data [195]. These calculations (Figure 6.8) are in agreement with consistent facts obtained from earlier theoretical and experimental studies such as the conduction band crosses the Fermi level at L points (marked 5) and the valence band does at H near T point (marked 3) [4, 193]. The smallest direct gap at the H point (from 3 to 4 in Figure 6.8) is estimated (using ImageJ software) to be 240±10 meV which is close to our smallest optical direct transition 228 meV. While the second smallest direct gap at points 1 and 2 (Figure 6.8) is 327±10 meV close to our optical direct transition value (342 meV). To the best of our knowledge, this is the first optical experimental data to determine these values.

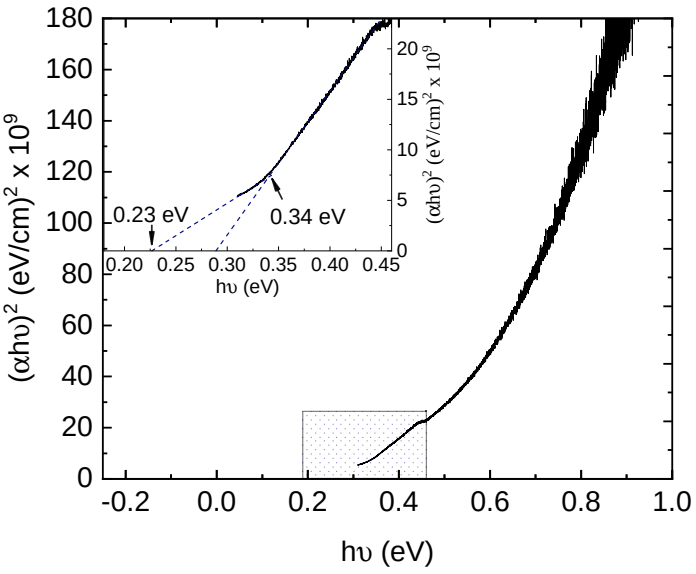


Figure 6.7: Tauc plot for the direct (black) and indirect (red) transitions in the S685 (Sb on glass) sample. The inset is a magnification of the dotted area in the direct plot.

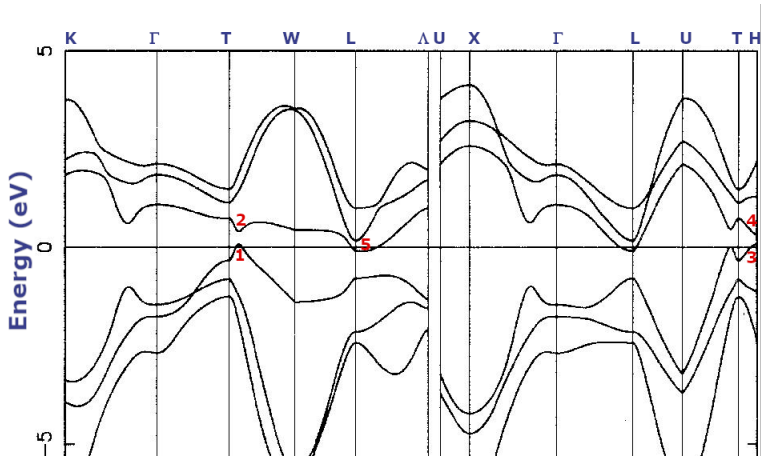


Figure 6.8: The calculated near-Fermi level band structure of Sb. The numbers on the graph refer to the valence band maxima and conduction band minima of our interests. Reprinted with permission from American Physical Society (1995) [4].

### 6.2.5 Work function

Figure 6.9 shows the CPD values (refers to the change in work function) of two Sb films, grown on glass and InAs (111)B substrates after different annealing periods at 200 °C. The least-square fitting y-intercept values of these vertical lines are plotted in Figure 6.10. The CPD of the Sb on the glass sample (blue dashed line) has a nearly constant value with annealing time (around -523±18 mV). Adding this value to the gold tip's work function (4.67±0.08 eV), the absolute work function of the Sb film grown on glass could be determined to be 4.15±0.18 eV. In the literature, the reported values of the Sb work function vary from 4.0 eV to around 4.7 eV [183, 185, 196–205]. Our Sb film lies in the bottom of that range, given that it is 150-nm thick (003) oriented on the glass; it was exposed to the ambient atmosphere during different analysis, which likely had formed an oxide layer on its surface. As explained earlier (Chapters 1 and 2), the work function value depends on the band structure, surface orientation, cleanliness, etc. And, the band structure is dependent on different factors, including the crystallography and the size of the material. The literature values are of samples of different crystallographic order (e.g. amorphous, polycrystalline and single crystal), and measured using different techniques, from photoelectric effect in 1937 [201] to ultraviolet photoelectron spectroscopy (UPS) of very thin films in the last couple of years [183, 185]. Moreover, ultra-thin Sb films on single crystal substrates could be strained (stretched or compressed), which adds another factor. These factors explain the spread of the work function reported values, adding to this, the different calibration methods used in each technique and its development over

the decades.

On the other hand, the sample that was grown on InAs(111)B (Figure 6.10) shows a continuous rise in the CPD value with annealing up to 3 hours (-200 mV) and then a slight drop at 5 hours annealing. This is probably related to the In segregation from the substrate to the Sb film's surface. The fact that the initial CPD value for the as-prepared Sb on the InAs sample is about 80 mV higher than that grown on glass could be attributed to small In residuals from the growth, as the growth occurred at 200 °C substrate temperature. With more annealing, the In percentage increased until reaching saturation after three hours. We speculate that In segregating to the surface is highly mobile and able to form In-Sb bonds with the outer atomic layer of Sb. This might have generated an additional negative surface dipole which increases the work function. The formation of an InSb-like surface termination halts when the surface is saturated with In, leading to agglomerations or droplets of In, consistent with the AFM observations of Figure 6.3 (b). This halts a further increase in work function. The above explanation could be further tested with XPS and UPS experiments. The decrease after that may be attributed to the indium dynamics (movements) on the surface. The In segregation and its consequences on the surface morphology and work function require critical attention for Sb film growth on In-containing substrates. This applies to thin and thick films, and future investigations on other substrates are recommended.

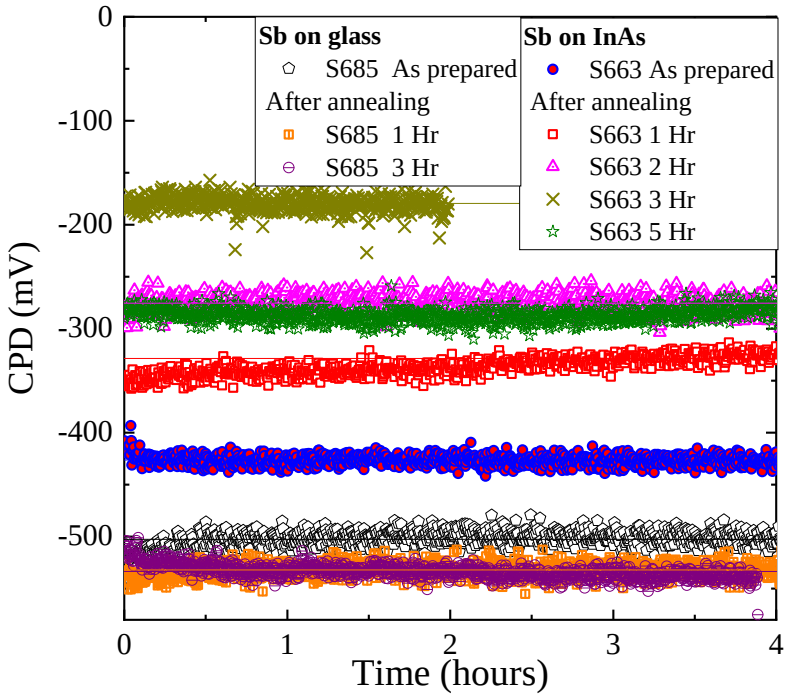


Figure 6.9: CPD values of Sb films S663 and S685 measured at room temperature over time. Y-axis is the measuring time; the annealed samples have different symbols as indicated. Vertical lines are linear least square fittings with zero slope.

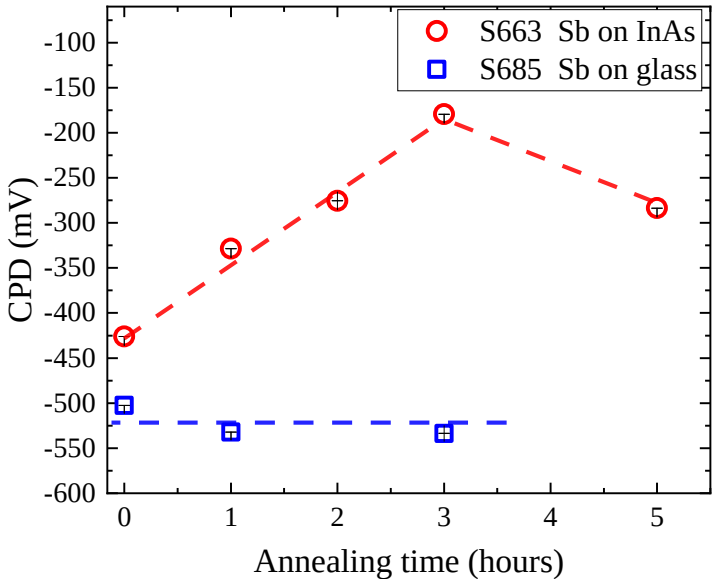


Figure 6.10: CPD dependence on the annealing time of S663 and S685 samples. Dashed lines are guides to the eye.

## 6.3 Conclusion

High-quality epitaxial Sb film was grown on InAs(111)B substrate with 3-fold rotational symmetry and a fully relaxed surface. The structure, morphology and work function were discussed for the as-prepared and annealed samples. With gentle annealing at 200 °C, the In segregated from the substrate to the surface of the Sb film and formed small agglomerations, which were observable by AFM and XPS analysis. The segregated In increased the surface work function of the film as discussed. Future surface-sensitive experiments need careful observation of such phenomena.

The room-temperature growth of Sb film on a chemically-treated glass substrate was also discussed. The film grown on glass has a strong (003) texture, and its electrical conductivity is very high, behaving as a metal more than a semiconductor. We were able to determine the positive direct band gap optically for the first time. The value was consistent with the calculated band structure of antimony. The work function of the Sb film on glass was constant during the annealing (4.15±0.18 eV), which lies at the low end of the previously reported values for Sb samples.

# Chapter 7

# Conclusion and Future Work

In this thesis, Sb, BiSb and ZnSb thin films prepared by the PVD technique were investigated. Different material science and surface science techniques were used in this study as explained in the following sections.

## 7.1 BiSb

BiSb is a topological insulator and a thermoelectric material. In the thesis, thin films of BiSb were grown on InP patterned substrates to increase the surface-to-volume ratio. This is preferred for enhancing the thermoelectric figure of merit by increasing the surface electrical conduction and suppressing the bulk thermal conduction. The InP substrates were successfully patterned by $Ar^+$ ion bombardment. The patterning was preserved during thermal annealing cycles for temperatures up to 400°C, which was set as an upper limit temperature. BiSb films were deposited on the patterned substrates and compared with those deposited on flat ones inside a UHV system. SEM and EDX confirmed the homogeneity of all samples with compositions near $Bi_{77}Sb_{23}$. The AFM topographs provided SR value, a parameter that was used to determine the increment in surface area due to patterning, and hence, correctly estimate the average thickness and the electrical parameters of the films. The structural analysis using XRD and RHEED techniques confirmed that films grown on patterned substrates were around 90% (012) oriented with some polycrystalline and (003) oriented portions. While films grown on flat substrates were 98-99% (003) oriented. This is believed to occur as the naturally expected (012) orientated BiSb film, with Sb $>$ 9% at room temperature, could not reorder to be (003) at high temperature because of the patterning. This change in texture impacted the electrical conduction of the films. To understand the impact of patterning

the substrate on the films, we used two approaches. The first one compares electrical Hall measurements for four samples with different thicknesses at 300 K and 77 K. From the first approach, it was concluded that (a) at room temperature, all films behave as n-type semiconductors with dominant bulk conduction. (b) (003) oriented films on flat substrates have more carrier concentration ($\approx$7.8 $\times 10^{19}$ cm$^{-3}$) than (012) oriented films on patterned substrates ($\approx$2.8 $\times 10^{19}$ cm$^{-3}$). (c) At 77K, conduction from the surface metallic states was dominant in both types. (d) The conductivity of the films increased with their "corrected" average thickness. (e) The film on a patterned substrate has the same conductivity as the film on the flat substrate with the same corrected thickness, but with a smaller number of carriers with higher mobility; this might be the surface carriers in the patterned samples, which are smaller in number and more mobile than the bulk carriers in the flat (003) oriented samples.

In the second approach, the resistance and Seebeck coefficient of six films, deposited in the same growth on substrates with different patterning, were compared. These samples were made as devices by lithography and using different HV systems; the optimisation process was discussed with the major challenges. The films exhibit a texture dependency on the substrate patterning as observed from the first series. To assess the contribution of the surface states in the conduction, the conductance in one flat sample and one patterned sample was studied for a wide range of temperatures (10 K to 300 K). The temperature-dependent conductance data was fitted according to different assumptions: (1) there is no surface conduction (2) the surface conduction is constant with temperature (3) the surface conduction changes with the temperature. It was found that both samples have a bulk conduction and a surface conduction which could be described as constant. The surface contribution to the total conductance was found higher in the patterned sample because it has more surface area. However, the total conductance was higher in the flat sample as it has a thicker film with a different orientation and a uniform thickness. The values of the Seebeck coefficient in the patterned samples increased with the temperature while showing a peak at 250 K for the flat sample. No trend was observed with the sputtering time, but mostly, the patterning reduces Seebeck coefficients.

The power factor of the flat sample was found to be 6 mW/mK$^2$, maximum at 250 K. The figure of merit of the flat sample was estimated to reach 0.67 at the same temperature.

**Future work** The patterning affected both the electrical conductivity and the Seebeck coefficient of the samples negatively, but its impact on the thermal conductivity is un-

known. Measuring the thermal conductivity for both flat and patterned samples would confirm the applicability of this approach (i.e. patterning the substrate) for thermoelectric devices. But there are some challenges to determine its value. For example, applying a steady temperature gradient through the sample during the measurements will transfer most of the heat through its substrate. Alternatively, using a thermal imaging technique [206] could be used. However, it is very challenging to be used with the patterned samples because of their rough surfaces. We failed to obtain reliable data using InGaP substrates and thermally imaging the samples due to this problem. Other approaches may be used such as separating the BiSb film from the substrate by using a thermal release tape, taking advantage of the weak adhesion with some substrates such as Si(111) [131].

## 7.2 ZnSb

ZnSb is a well-known thermoelectric material. In this project, the applicability of using ZnSb films, using the LP-PVD technique, for flexible electronics was studied. ZnSb films of different compositions were grown on glass and Kapton inside an HV system. The as-prepared films were non-crystalline, but with gentle annealing at 150-200°C, they turned crystalline with high conductivity. The films remain stable over time and with further annealing up to 250°C. The increase in Zn composition near stoichiometry changes the dominant phase from ZnSb to $Zn_4Sb_3$ as detected by XRD. This affects the electrical and optical properties of the studied films. The electrical properties of off-stoichiometric samples are more temperature-dependent, probably due to the conduction through the gap states in these samples. The optical band gaps of the samples were studied using Tauc analysis of the absorption data. The direct gaps were determined to be 0.9 eV for the ZnSb phase, and fluctuating around 1.07 for $Zn_4Sb_3$ and mixed phases samples, consistent with the literature values. In-doping was discussed as well, but the uncontrolled ratio between ZnSb to $Zn_4Sb_3$ phases had an impact on the studied films.

The most sounding result is that films on flexible Kapton have shown similar electrical and optical properties to those grown on glass. Moreover, the electrical and optical properties of the flexible films remain stable after $10^4$ bending cycles, around 7% of their original values before bending. The conductivity was degraded only after harsh manual twisting tens to hundreds of cycles. This suggests that our films, grown using the PVD technique, exhibit superior stability compared to those produced by screen-printing methods, which did not withstand even static bending [159]. This finding is particularly significant considering the increasing favour of the PVD technique for flexible thermoelectric applications due to its high-throughput capabilities [207].

The thermoelectric power factor of the ZnSb film on Kapton reached a very high value among other undoped polycrystalline thin films in the literature (1049 $\mu$W/m.K$^2$), under 400 K. While ZnSb-In films were around 836 $\mu$W/m.K$^2$ (for 2.4- 3.4%In).

**Future work** It would be helpful to measure the thermal conductivity of all films to know the impact of In-doping on the thermal conductivity of ZnSb films. Some aspects could be further explored with the films such as the impact of the flexing on devices containing ZnSb legs. This could be studied by fabricating a TE module from ZnSb as a p-type leg with another n-type leg and assessing its performance under flexing conditions. Other types of flexible biodegradable substrates could be very interesting to be explored such as fungal mycelium skins [208]."

## 7.3 Sb

Antimony is an interesting semimetal that is involved in many electronic applications. Understanding the impact of the preparation conditions (e.g. substrate type and temperature and post-annealing) on the film's properties (e.g. structure and electronic properties) is of great interest. In this project, Sb thin films were grown in InAs(111)B and glass substrates inside an MBE UHV system. These films were studied before and after being annealed using different techniques as follows. The first film (43 nm) was grown on the InAs substrate epitaxially with a high-quality fully relaxed surface as confirmed by RHEED analysis. The AFM shows smooth film with facets and 3-fold rotational symmetry features. After gentle annealing at 200 °C, small agglomeration started to appear on the surface. These are believed to be formed by In segregation from the substrate to the surface of the Sb film, as concluded from XPS analysis. The work function changed by this effect, probably due to the creation of an additional negative surface dipole (e.g. InSb) and indium movement after saturation to form agglomerations.

On the other hand, the 150 nm Sb film grown on glass at room temperature was more stable. The film showed a strong (003) texture and different morphology from the epitaxial film. The electrical conductivity of the film was high at room temperature ($7.1\times 10^3$ $\Omega^{-1}$ cm $^{-1}$), with more metallic behaviour than semiconducting (i.e. conductivity decreases with temperature). Tauc plot of the optical absorbance determines the direct band to be 228 meV, consistent with the calculated band structure of Sb. The work function of the film was stable during the annealing process and was determined to be 4.15±0.18 eV, which lies at the low end of the Sb values in the literature.

**Future work** The problem of In segregation through Sb films is likely to appear with other elements, especially if the Sb layer is ultra-thin. Further studies could help understand the working temperature limit for the Sb-containing devices. Additionally, studying indium surface segregation in other compounds is of great importance, as such behaviour was observed in different other compounds [209, 210]. This study could be done using surface analysis techniques (e.g. AFM and XPS) during or after the growth and thermal treatments. One possible usage of the Sb films on glass is to calibrate KP tips, as the work function stayed stable under annealing conditions. More analysis could be required to test the durability of such a standard sample under different wear and tear conditions.

# Appendix A

# Materials' electronic configuration and structure

Antimony is a semimetal element with atomic number 51. Its electronic configuration is [Kr] $5s^2 4d^{10} 5p^3$, meaning it has 3 valence electrons in $5p$ orbitals, each one is in a separate orbital. It has different phases, the most common stable one is a rhombohedral lattice structure with space group R$\bar{3}$m (also called A7 structure [189]). Its reduced cell dimensions are a:4.307 Å, b: 4.307 Å and c: 4.506 Å and angels $\alpha : 61.45$, $\beta : 61.45$ and $\gamma : 60.00°$ (PDF 00-005-0562) [82]. Similarly, bismuth is located in the same group (15) as antimony, with atomic number 83. Its electronic configuration is [Xe] $6s^2 4f^{14} 5d^{10} 6p^3$. Despite having 5 valence electrons, in either Bi or Sb crystal lattice, atoms typically associate in pairs to form a unit cell of two ions with 10 electrons [189]. They can have different oxidation states (+3 and +5) when bonded with other elements [211].

When both elements bond together to form BiSb, they tend to have the same rhombohedral phase, with R$\bar{3}$m space group. But it has slightly bigger cell (for $Bi_{0.8}Sb_{0.2}$, a:4.519 Å, b: 4.519 Å and c: 4.720 Å and angles $\alpha : 61.40$, $\beta : 61.40$ and $\gamma : 60.00°$ for (PDF 04-023-9518) [82]). In other words, BiSb forms a continuous solid solution [212]. However, the electronic structure varies between direct and indirect semiconducting and semimetallic depending on their percentage, the film thickness and growth orientation [213], which makes them very interesting.

On the other hand, zinc is a metal in group 12, with atomic number 30. The electronic configuration is [Ar] $3d^{10}$ $4s^2$. It has 2 valence 4s electrons which can lose and become +2. With antimony, Zn-Sb compounds can present in various phases, other than $\alpha$-$Zn_3Sb_2$, depending on factors such as composition and temperature (see Zn-Sb phase diagram [153]). Samples can have multiple phases and phases may transform from

one to another by thermal annealing [153, 154]. The most common ones, in the stoichiometric region at room temperature, are the orthorhombic ZnSb (space group Pbca) (PDF 040224699) and the rhombohedral $\beta$-$Zn_4Sb_3$ (space group $R\bar{3}C$) (PDF 000561306) [82, 165, 214]. The later is also considered to be $Zn_{13}Sb_{10}$, as Zn has partial occupancy in some sites [215, 216].

# Appendix B

# Thickness calibration of Sb films on InAs(111)B

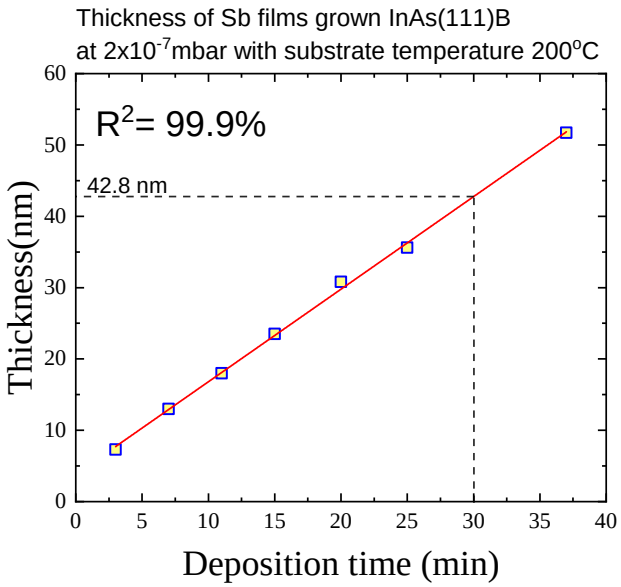


Figure B.1: Thickness of Sb films grown InAs(111)B at $2x10^{-7}$ mbar with substrate temperature 200°C. The red solid line is a linear fitting of the data, and the black dotted line refers to thickness after 30 min deposition as for Sample S663. The thickness of the films in this series was determined by X-ray fluorescence (XRF). The calibration of the XRF thickness was done by three other samples with known thickness by X-ray reflectometry (XRR)

# Appendix C

# XPS of Sb film

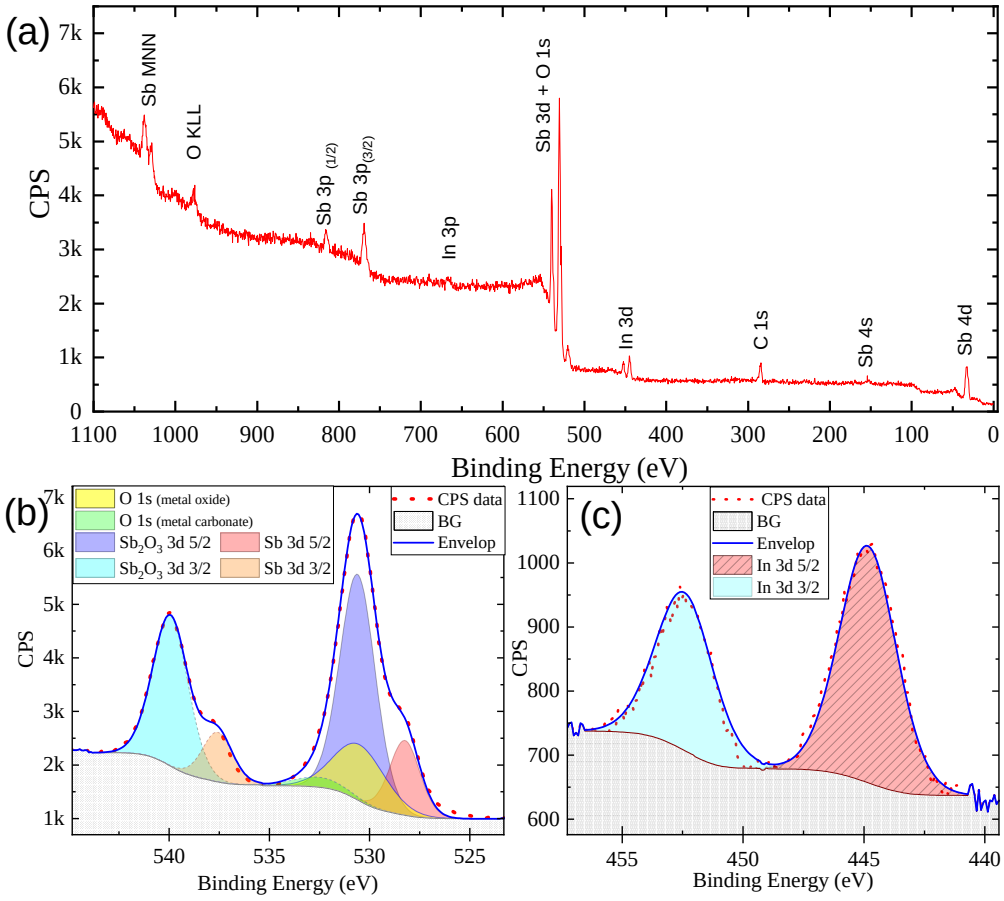


Figure C.1: XPS analysis of 5-hours 200°C-annealed Sb on InAs (111)B sample (S663). (a) Survey scan, (b) Sb 3d region and (c) In 3d region.

# Bibliography


[1] HD Young, RA Freedman, TR Sandin, and A Lewis Ford. *University physics. 11.* Pearson, San Francisco, CA, 2004.

[2] Charles Kittel and Paul McEuen. *Introduction to solid state physics*, volume 8. John Wiley and Sons Inc New York, 2005.

[3] Electronic band structure - Wikipedia. `https://en.wikipedia.org/wiki/Electronic_band_structure/`, march 2017. [The SVG file is made available under the Creative Commons CC0 1.0 Universal Public Domain Dedication (i.e. No copyrights); it could be used, modified and distributed without asking for permission. Accessed on 10 Febreuary 2023.].

[4] Yi Liu and Roland E Allen. Electronic structure of the semimetals Bi and Sb. *Physical Review B*, 52(3):1566, 1995.

[5] Nevill Francis Mott and Edward A Davis. *Electronic processes in non-crystalline materials.* Oxford university press, 2012.

[6] EA Davis and NFf Mott. Conduction in non-crystalline systems v. conductivity, optical absorption and photoconductivity in amorphous semiconductors. *Philosophical magazine*, 22(179):0903–0922, 1970.

[7] Marius Grundmann. *Surfaces*, pages 385–397. Springer International Publishing, Cham, 2016.

[8] Ning Xu, Yong Xu, and Jia Zhu. Topological insulators for thermoelectrics. *npj Quantum Materials*, 2(1):51, 2017.

[9] David Hsieh, Dong Qian, Lewis Wray, Yiman Xia, Yew San Hor, Robert Joseph Cava, and M Zahid Hasan. A topological Dirac insulator in a quantum spin Hall phase. *Nature*, 452(7190):970–974, 2008.

[10] Joel E Moore. The birth of topological insulators. *Nature*, 464(7286):194–198, 2010.

[11] Judy J Cha, Kristie J Koski, and Yi Cui. Topological insulator nanostructures. *physica status solidi (RRL)–Rapid Research Letters*, 7(1-2):15–25, 2013.

[12] Ryuji Takahashi and Shuichi Murakami. Thermoelectric transport in topological insulators. *Semiconductor Science and Technology*, 27(12):124005, dec 2012.

[13] Liang He, Xufeng Kou, and Kang L. Wang. Review of 3D topological insulator thin-film growth by molecular beam epitaxy and potential applications. *physica status solidi (RRL) - Rapid Research Letters*, 7(1-2):50–63, feb 2013.

[14] Theresa P Ginley, Yong Wang, and Stephanie Law. Topological insulator film growth by molecular beam epitaxy: A review. *Crystals*, 6(11):154, 2016.

[15] Lukas Müchler, Binghai Yan, Frederick Casper, Stanislav Chadov, and Claudia Felser. *Topological Insulators*, pages 123–139. Springer Berlin Heidelberg, Berlin, Heidelberg, 2013.

[16] L. D. Hicks and M. S. Dresselhaus. Thermoelectric figure of merit of a one-dimensional conductor. *Phys. Rev. B*, 47:16631–16634, Jun 1993.

[17] L. D. Hicks and M. S. Dresselhaus. Effect of quantum-well structures on the thermoelectric figure of merit. *Phys. Rev. B*, 47:12727–12731, May 1993.

[18] H Julian Goldsmid. *Introduction to thermoelectricity*, volume 121. Springer, 2016.

[19] X F Zheng, C X Liu, Y Y Yan, and Q Wang. A review of thermoelectrics research – Recent developments and potentials for sustainable and renewable energy applications. *Renewable and Sustainable Energy Reviews*, 32:486–503, 2014.

[20] H Julian Goldsmid. *Electronic refrigeration, London, U.K.* Pion, 1986.

[21] HJ Goldsmid. Basic principles. *Thermoelectric Refrigeration*, pages 1–11, 1964.

[22] Aldo Vieira da Rosa and Juan Carlos Ordóñez. Chapter 5 - thermoelectricity. In Aldo Vieira da Rosa and Juan Carlos Ordóñez, editors, *Fundamentals of Renewable Energy Processes (Fourth Edition)*, pages 187–247. Academic Press, Oxford, fourth edition edition, 2022.

[23] HJ Goldsmid and JW Sharp. Estimation of the thermal band gap of a semiconductor from seebeck measurements. *Journal of electronic materials*, 28:869–872, 1999.

[24] T. Borca-Tasciuc and G. Chen. *Experimental Techniques for Thin-Film Thermal Conductivity Characterization*, pages 205–237. Springer US, Boston, MA, 2004.

[25] Chris Dames. Measuring the thermal conductivity of thin films: 3 omega and related electrothermal methods. *Annual Review of Heat Transfer*, 16, 2013.

[26] Alex Zevalkink, David M Smiadak, Jeff L Blackburn, Andrew J Ferguson, Michael L Chabinyc, Olivier Delaire, Jian Wang, Kirill Kovnir, Joshua Martin, Laura T Schelhas, et al. A practical field guide to thermoelectrics: Fundamentals, synthesis, and characterization. *Applied Physics Reviews*, 5(2):021303, 2018.

[27] Hilaal Alam and Seeram Ramakrishna. A review on the enhancement of figure of merit from bulk to nano-thermoelectric materials. *Nano Energy*, 2(2):190–212, 2013.

[28] Rolf Landauer. Spatial variation of currents and fields due to localized scatterers in metallic conduction. *IBM Journal of research and development*, 1(3):223–231, 1957.

[29] Jesse Maassen and Mark Lundstrom. The landauer approach to electron and phonon transport. *ECS Transactions*, 69(9):23, 2015.

[30] Supriyo Datta. *Lessons from Nanoelectronics: A New Perspective on Transport—Part B: Quantum Transport*. World Scientific, 2018.

[31] Raseong Kim, Supriyo Datta, and Mark S Lundstrom. Influence of dimensionality on thermoelectric device performance. *Journal of Applied Physics*, 105(3):034506, 2009.

[32] Changwook Jeong, Supriyo Datta, and Mark Lundstrom. Thermal conductivity of bulk and thin-film silicon: A landauer approach. *Journal of Applied Physics*, 111 (9):093708, 2012.

[33] Jaeho Lee. *Heat Transfer in Semiconductor Nanostructures*, pages 1453–1462. Springer Netherlands, Dordrecht, 2016.

[34] Cheng Chang and Li-Dong Zhao. Anharmoncity and low thermal conductivity in thermoelectrics. *Materials Today Physics*, 4:50–57, mar 2018.

[35] Eric J. Skoug and Donald T. Morelli. Role of Lone-Pair Electrons in Producing Minimum Thermal Conductivity in Nitrogen-Group Chalcogenide Compounds. *Physical Review Letters*, 107(23):235901, nov 2011.

[36] D. T. Morelli, V. Jovovic, and J. P. Heremans. Intrinsically Minimal Thermal Conductivity in Cubic I-V -$VI_2$ Semiconductors. *Physical Review Letters*, 101(3): 035901, jul 2008.

[37] Baoli Du, Ruizhi Zhang, Kan Chen, Amit Mahajan, and Mike J. Reece. The impact of lone-pair electrons on the lattice thermal conductivity of the thermoelectric compound $CuSbS_2$. *Journal of Materials Chemistry A*, 5(7):3249–3259, feb 2017.

[38] Shanyu Wang, Yongxing Sun, Jiong Yang, Bo Duan, Lihua Wu, Wenqing Zhang, and Jihui Yang. High thermoelectric performance in Te-free $(Bi,Sb)_2$ $Se_3$ via structural transition induced band convergence and chemical bond softening. *Energy & Environmental Science*, 9(11):3436–3447, nov 2016.

[39] Robert L. González-Romero, Alex Antonelli, Anderson S. Chaves, and Juan J. Meléndez. Ultralow and anisotropic thermal conductivity in semiconductor $As_2Se_3$. *Physical Chemistry Chemical Physics*, 20(3):1809–1816, 2018.

[40] O. Delaire, J. Ma, K. Marty, A. F. May, M. A. McGuire, M-H. Du, D. J. Singh, A. Podlesnyak, G. Ehlers, M. D. Lumsden, and B. C. Sales. Giant anharmonic phonon scattering in PbTe. *Nature Materials*, 10(8):614–619, aug 2011.

[41] G. Lucovsky and R. M. White. Effects of Resonance Bonding on the Properties of Crystalline and Amorphous Semiconductors. *Physical Review B*, 8(2):660–667, jul 1973.

[42] B. C. Sales, D. Mandrus, and R. K. Williams. Filled Skutterudite Antimonides: A New Class of Thermoelectric Materials. *Science*, 272(5266):1325–1328, may 1996.

[43] G. S. Nolas, G. A. Slack, D. T. Morelli, T. M. Tritt, and A. C. Ehrlich. The effect of rare-earth filling on the lattice thermal conductivity of skutterudites. *Journal of Applied Physics*, 79(8):4002, aug 1996.

[44] Toshiro Takabatake, Koichiro Suekuni, Tsuneyoshi Nakayama, and Eiji Kaneshita. Phonon-glass electron-crystal thermoelectric clathrates: Experiments and theory. *Reviews of Modern Physics*, 86(2):669–716, jun 2014.

[45] Jiazhen Wu, Jingtao Xu, Dwi Prananto, Hidekazu Shimotani, Yoichi Tanabe, Satoshi Heguri, and Katsumi Tanigaki. Systematic studies on anharmonicity of rattling phonons in type-I clathrates by low-temperature heat capacity measurements. *Physical Review B*, 89(21):214301, jun 2014.

[46] Manoj K. Jana, Koushik Pal, Umesh V. Waghmare, and Kanishka Biswas. The Origin of Ultralow Thermal Conductivity in InTe: Lone-Pair-Induced Anharmonic Rattling. *Angewandte Chemie International Edition*, 55(27):7792–7796, jun 2016.

[47] Manoj K. Jana, Koushik Pal, Avinash Warankar, Pankaj Mandal, Umesh V. Waghmare, and Kanishka Biswas. Intrinsic Rattler-Induced Low Thermal Conductivity in Zintl Type $TlInTe_2$. *Journal of the American Chemical Society*, 139(12):4350–4353, mar 2017.

[48] Yixuan Wu, Bo Gao, Siqi Lin, Binqiang Zhou, Wen Li, Yanzhong Pei, Zhiwei Chen, Xinyue Zhang, Alireza Faghaninia, Juan Li, and Anubhav Jain. Promising thermoelectric performance in van der Waals layered $SnSe_2$. *Materials Today Physics*, 3:127–136, 2017.

[49] D. Krishna Bhat and U. Sandhya Shenoy. Enhanced thermoelectric performance of bulk tin telluride: Synergistic effect of calcium and indium co-doping. *Materials Today Physics*, 4:12–18, 2018.

[50] Andreas Fischer, E-W Scheidt, Wolfgang Scherer, DE Benson, Yang Wu, Daniel Eklöf, and Ulrich Häussermann. Thermal and vibrational properties of thermoelectric ZnSb: Exploring the origin of low thermal conductivity. *Physical Review B*, 91(22):224309, 2015.

[51] Terry M. Tritt. *Thermal conductivity : theory, properties, and applications*. Kluwer Academic/Plenum Publishers, 2004.

[52] R. Berman and Paul G. Klemens. Thermal Conduction in Solids. *Physics Today*, 31(4):56–57, apr 1978.

[53] D G Cahill and R O Pohl. Lattice Vibrations and Heat Transport in Crystals and Glasses. *Annual Review of Physical Chemistry*, 39(1):93–121, oct 1988.

[54] Arash Mehdizadeh Dehkordi, Mona Zebarjadi, Jian He, and Terry M Tritt. Thermoelectric power factor: Enhancement mechanisms and strategies for higher performance thermoelectric materials. *Materials Science and Engineering: R: Reports*, 97:1–22, 2015.

[55] Daniel Magnfält. *Fundamental processes in thin film growth: The origin of compressive stress and the dynamics of the early growth stages.* PhD thesis, Linköping University Electronic Press, 2014.

[56] K Reichelt and X Jiang. The preparation of thin films by physical vapour deposition methods. *Thin Solid Films*, 191(1):91–126, 1990.

[57] C Ratsch and JA Venables. Nucleation theory and the early stages of thin film growth. *Journal of Vacuum Science & Technology A: Vacuum, Surfaces, and Films*, 21(5):S96–S109, 2003.

[58] Carl V Thompson. Structure evolution during processing of polycrystalline films. *Annual review of materials science*, 30(1):159–190, 2000.

[59] PB Barna and M Adamik. Fundamental structure forming phenomena of polycrystalline films and the structure zone models. *Thin solid films*, 317(1-2):27–33, 1998.

[60] Harald Brune. Microscopic view of epitaxial metal growth: nucleation and aggregation. *Surface Science Reports*, 31(4-6):125–229, 1998.

[61] Uwe Köster. Crystallization and decomposition of amorphous semiconductors. *Advances in Colloid and Interface Science*, 10(1):129–172, 1979.

[62] R. Michel, J. Gastaldi, C. Allasia, C. Jourdan, and J. Derrien. Initial interaction of oxygen with aluminium single crystal faces: A leed, aes and work function study. *Surface Science*, 95(1):309–320, 1980.

[63] N Feldberg, JD Aldous, PA Stampe, RJ Kennedy, TD Veal, and SM Durbin. Growth of $ZnSnN_2$ by molecular beam epitaxy. *Journal of electronic materials*, 43 (4):884–888, 2014.

[64] Biljana Pejova and Ivan Grozdanov. Chemical deposition and characterization of $Cu_3Se_2$ and CuSe thin films. *Journal of Solid State Chemistry*, 158(1):49–54, 2001.

[65] Biljana Pejova, Atanas Tanuševski, and Ivan Grozdanov. Semiconducting thin films of zinc selenide quantum dots. *Journal of Solid State Chemistry*, 177(12): 4785–4799, 2004.

[66] Phil Woodruff. *Modern Techniques of Surface Science*. Cambridge University Press, Cambridge, 2016.

[67] Thomas Kuech. *Handbook of Crystal Growth: Thin Films and Epitaxy*. Elsevier, 2014.

[68] Sagnik Middya, Gabriele S. Kaminski Schierle, George G. Malliaras, and Vincenzo F. Curto. Chapter 8 - lithography and electrodes. In Soumen Das and Sandip Dhara, editors, *Chemical Solution Synthesis for Materials Design and Thin Film Device Applications*, pages 277–307. Elsevier, 2021.

[69] Shuji Hasegawa. Reflection high-energy electron diffraction. *Characterization of Materials*, 97:1925–1938, 2012.

[70] Ayahiko Ichimiya and Philip I Cohen. *Reflection high-energy electron diffraction*. Cambridge University Press, 2004.

[71] Christopher W Burrows. *Growth and Characterisation of MnSb Thin Films and Interfaces*. PhD thesis, University of Warwick, 2012.

[72] Weilie Zhou, Robert Apkarian, Zhong Lin Wang, and David Joy. *Fundamentals of Scanning Electron Microscopy (SEM)*, pages 1–40. Springer New York, New York, NY, 2007.

[73] Joseph I Goldstein, Dale E Newbury, Joseph R l, Nicholas WM Ritchie, John Henry J Scott, and David C Joy. *Scanning electron microscopy and X-ray microanalysis*. Springer, 2017.

[74] M Abd Mutalib, MA Rahman, MHD Othman, AF Ismail, and J Jaafar. Scanning electron microscopy (SEM) and energy-dispersive X-ray (EDX) spectroscopy. In *Membrane characterization*, pages 161–179. Elsevier, 2017.

[75] Oliver D Payton, Loren Picco, and Thomas Bligh Scott. High-speed atomic force microscopy for materials science. *International Materials Reviews*, 61(8):473–494, 2016.

[76] David Nečas and Petr Klapetek. Gwyddion: an open-source software for SPM data analysis. *Central European Journal of Physics*, 10:181–188, 2012.

[77] Gwyddion – Free SPM (AFM, SNOM/NSOM, STM, MFM, ...) data analysis software. `http://gwyddion.net/`. [Online; accessed 15/11/2021].

[78] David Nečas and Petr Klapetek. One-dimensional autocorrelation and power spectrum density functions of irregular regions. *Ultramicroscopy*, 124:13–19, 2013.

[79] David Nečas, Petr Klapetek, and Miroslav Valtr. Estimation of roughness measurement bias originating from background subtraction. *Measurement Science and Technology*, 31(9):094010, 2020.

[80] Akhilesh Pandey, Sandeep Dalal, Shankar Dutta, and Ambesh Dixit. Structural characterization of polycrystalline thin films by x-ray diffraction techniques. *Journal of Materials Science: Materials in Electronics*, 32(2):1341–1368, 2021.

[81] William Henry Bragg and William Lawrence Bragg. The reflection of X-rays by crystals. *Proceedings of the Royal Society of London. Series A, Containing Papers of a Mathematical and Physical Character*, 88(605):428–438, 1913.

[82] Stacy Gates-Rector and Thomas Blanton. The powder diffraction file: a quality materials characterization database. *Powder Diffraction*, 34:352–360, 12 2019.

[83] Cameron F. Holder and Raymond E. Schaak. Tutorial on powder x-ray diffraction for characterizing nanoscale materials. *ACS Nano*, 13(7):7359–7365, 2019. PMID: 31336433.

[84] P Scherrer. Nachr ges wiss goettingen. *Math. Phys.*, 2:98–100, 1918.

[85] Uwe Holzwarth and Neil Gibson. The Scherrer equation versus the'Debye-Scherrer equation'. *Nature nanotechnology*, 6(9):534–534, 2011.

[86] GK Williamson and WH Hall. X-ray line broadening from filed aluminium and wolfram. *Acta metallurgica*, 1(1):22–31, 1953.

[87] Thomas Degen, Mustapha Sadki, Egbert Bron, Uwe König, and Gwilherm Nénert. The highscore suite. *Powder diffraction*, 29(S2):S13–S18, 2014.

[88] G.B. Harris. X. Quantitative measurement of preferred orientation in rolled uranium bars. *The London, Edinburgh, and Dublin Philosophical Magazine and Journal of Science*, 43(336):113–123, jan 1952.

[89] Akhilesh Pandey, Sandeep Dalal, Shankar Dutta, and Ambesh Dixit. Structural characterization of polycrystalline thin films by X-ray diffraction techniques, jan 2021.

[90] August Beer. Bestimmung der absorption des rothen lichts in farbigen flussigkeiten. *Ann. Physik*, 162:78–88, 1852.

[91] Grundmann Marius. *The Physics of Semiconductors: An Introduction Including Nanophysics and Applications*. Spinger, 2016.

[92] Antonio Ricardo Zanatta. Revisiting the optical bandgap of semiconductors and the proposal of a unified methodology to its determination. *Scientific reports*, 9(1): 1–12, 2019.

[93] J Tauc, Radu Grigorovici, and Anina Vancu. Optical properties and electronic structure of amorphous germanium. *physica status solidi (b)*, 15(2):627–637, 1966.

[94] Brian D Viezbicke, Shane Patel, Benjamin E Davis, and Dunbar P Birnie III. Evaluation of the tauc method for optical absorption edge determination: ZnO thin films as a model system. *physica status solidi (b)*, 252(8):1700–1710, 2015.

[95] Patrycja Makuła, Michał Pacia, and Wojciech Macyk. How To Correctly Determine the Band Gap Energy of Modified Semiconductor Photocatalysts Based on UV-Vis Spectra. *Journal of Physical Chemistry Letters*, 9:6814–6817, 12 2018.

[96] Santosh K Suram, Paul F Newhouse, and John M Gregoire. High throughput light absorber discovery, part 1: an algorithm for automated tauc analysis. *ACS combinatorial science*, 18(11):673–681, 2016.

[97] Nader Ghobadi. Band gap determination using absorption spectrum fitting procedure. *International Nano Letters*, 3(1):1–4, 2013.

[98] Resistivity and Hall Measurements | NIST. URL https://www.nist.gov/pml/nanoscale-device-characterization-division/popular-links/hall-effect/resistivity-and-hall[Accessed on 15-11-2021].

[99] Leo J van der Pauw. A method of measuring the resistivity and hall coefficient on lamellae of arbitrary shape. *Philips technical review*, 20:220–224, 1958.

[100] Leo J van der Pauw. A method of measuring specific resistivity and hall effect of discs of arbitrary shape. *Philips Research Reports*, 13(1):1–9, 1958.

[101] Antoine Kahn. Fermi level, work function and vacuum level. *Materials Horizons*, 3(1):7–10, 2016.

[102] John Bardeen. Theory of the work function. ii. the surface double layer. *Physical Review*, 49(9):653, 1936.

[103] EP Wigner and J Bardeen. Theory of the work functions of monovalent metals. In *Part I: Physical Chemistry. Part II: Solid State Physics*, pages 398–401. Springer, 1997.

[104] Dr Gavin Bell. Private communication, University of Warwick, 2023.

[105] Manuel Nonnenmacher, MP O'Boyle, and H Kumar Wickramasinghe. Kelvin probe force microscopy. *Applied physics letters*, 58(25):2921–2923, 1991.

[106] Gerhard Ertl, Jürgen Küppers, and Jürgen Küppers. Low energy electrons and surface chemistry; monographs in modern chemistry, 1974.

[107] Paul P Craig and Veljko Radeka. Stress dependence of contact potential: The ac kelvin method. *Review of Scientific Instruments*, 41(2):258–264, 1970.

[108] Gregory N Derry, Megan E Kern, and Eli H Worth. Recommended values of clean metal surface work functions. *Journal of Vacuum Science & Technology A: Vacuum, Surfaces, and Films*, 33(6):060801, 2015.

[109] Barton L Houseman and Barbara E Marzocchi. The influence of substrate temperature on the sticking coefficient of zinc on glass. Technical report, GOUCHER COLL BALTIMORE MD, 1968.

[110] Gowrish K Rao, Kasturi V Bangera, and GK Shivakumar. The effect of substrate temperature on the structural, optical and electrical properties of vacuum deposited ZnTe thin films. *Vacuum*, 83(12):1485–1488, 2009.

[111] Aristotelis Trapalis. *Development of zinc nitride materials for semiconductor applications*. PhD thesis, University of Sheffield, 2018.

[112] Oliver LI Brown. The clausius-clapeyron equation. *Journal of Chemical Education*, 28(8):428, 1951.

[113] Yiming Zhang, Julian RG Evans, and Shoufeng Yang. Corrected values for boiling points and enthalpies of vaporization of elements in handbooks. *Journal of Chemical & Engineering Data*, 56(2):328–337, 2011.

[114] Rafat Saleh, Maximilian Barth, Wolfgang Eberhardt, and André Zimmermann. Bending setups for reliability investigation of flexible electronics. *Micromachines*, 12(1):78, 2021.

[115] Haoyu U Li and Thomas N Jackson. Flexibility testing strategies and apparatus for flexible electronics. *IEEE Transactions on Electron Devices*, 63(5):1934–1939, 2016.

[116] Daniel Nilsen Wright, Astrid-Sofie B Vardøy, Branson D Belle, Maaike M Visser Taklo, Olle Hagel, Li Xie, Magnus Danestig, and Torbjörn Eriksson. Bending machine for testing reliability of flexible electronics. In *2017 IMAPS Nordic Conference on Microelectronics Packaging (NordPac)*, pages 47–52. IEEE, 2017.

[117] Mohammad M Hamasha, Khalid Alzoubi, James C Switzer, Susan Lu, Mark D Poliks, and Charles R Westgate. Reliability of sputtered aluminum thin film on flexible substrate under high cyclic bending fatigue conditions. *IEEE Transactions on Components, Packaging and Manufacturing Technology*, 2(12):2007–2016, 2012.

[118] Varun V Soman, Yasser Khan, Madina Zabran, Mark Schadt, Paul Hart, Michael Shay, Frank D Egitto, Konstantinos I Papathomas, Natasha AD Yamamoto, Donggeon Han, et al. Reliability challenges in fabrication of flexible hybrid electronics for human performance monitors: A system-level study. *IEEE Transactions on Components, Packaging and Manufacturing Technology*, 9(9):1872–1887, 2019.

[119] Wenchao Tian, Wenbo Yu, Jing Shi, and Yongkun Wang. The property, preparation and application of topological insulators: A review. *Materials*, 2017.

[120] Haim Beidenkopf, Pedram Roushan, Jungpil Seo, Lindsay Gorman, Ilya Drozdov, Yew San Hor, R. J. Cava, and Ali Yazdani. Spatial fluctuations of helical Dirac fermions on the surface of topological insulators. *Nature Physics*, 7(12):939–943, dec 2011.

[121] Parsa Bonderson, Chetan Nayak, and Xiao-Liang Qi. A time-reversal invariant topological phase at the surface of a 3D topological insulator. *Journal of Statistical Mechanics: Theory and Experiment*, 2013(09):P09016, sep 2013.

[122] Ning Xu, Yong Xu, and Jia Zhu. Topological insulators for thermoelectrics, 2017.

[123] T Hirahara, Y Sakamoto, Y Saisyu, H Miyazaki, S Kimura, T Okuda, I Matsuda, S Murakami, and S Hasegawa. Topological metal at the surface of an ultrathin $Bi_{1-x}$ $Sb_x$ alloy film. *Physical Review B*, 81(16):165422, 2010.

[124] Yugo Ueda, Nguyen Huynh Duy Khang, Kenichiro Yao, and Pham Nam Hai. Epitaxial growth and characterization of $Bi_{1-x}$ $Sb_x$ spin Hall thin films on GaAs (111) A substrates. *Applied Physics Letters*, 110(6):062401, 2017.

[125] Ekrem Güneş, Bernadette Landschreiber, Gert Homm, Christoph Wiegand, Petr Tomeš, Christian Will, Matthias T Elm, Silke Paschen, Peter J Klar, Sabine Schlecht, et al. Structure and Thermoelectric Properties of Nanostructured $Bi_{1-x}Sb_x$ Alloys Synthesized by Mechanical Alloying. *Journal of Electronic Materials*, 47(10):6007–6015, 2018.

[126] Oleg A Tretiakov, Ar Abanov, and Jairo Sinova. Holey topological thermoelectrics. *Applied Physics Letters*, 99(11):113110, 2011.

[127] Vinay Venugopal, T Basu, S Garg, JK Tripathi, S Chandramohan, P Das, TK Chini, SR Bhattacharyya, D Kanjilal, and T Som. Ion erosion induced nanostructured semiconductor surfaces. *International journal of nanotechnology*, 9(10): 1007, 2012.

[128] T Bobek, S Facsko, T Dekorsy, and H Kurz. Ordered quantum dot formation on GaSb surfaces during ion sputtering. *Nuclear Instruments and Methods in Physics Research Section B: Beam Interactions with Materials and Atoms*, 178(1-4):101–104, 2001.

[129] MP Seah, SJ Spencer, PJ Cumpson, and JE Johnstone. Sputter-induced cone and filament formation on inp and afm tip shape determination. *Surface and Interface Analysis: An International Journal devoted to the development and application of techniques for the analysis of surfaces, interfaces and thin films*, 29(11):782–790, 2000.

[130] F Frost and B Rauschenbach. Nanostructuring of solid surfaces by ion-beam erosion. *Applied Physics A*, 77(1):1–9, 2003.

[131] Emily S Walker, Sarah Muschinske, Christopher J Brennan, Seung Ryul Na, Tanuj Trivedi, Stephen D March, Yukun Sun, Tianhao Yang, Alice Yau, Daehwan Jung, et al. Composition-dependent structural transition in epitaxial $Bi_{1-x}Sb_x$ thin films on Si(111). *Physical Review Materials*, 3(6):064201, 2019.

[132] Zhendong Chi, Yong-Chang Lau, Xiandong Xu, Tadakatsu Ohkubo, Kazuhiro Hono, and Masamitsu Hayashi. The spin hall effect of Bi-Sb alloys driven by thermally excited Dirac-like electrons. *Science advances*, 6(10):eaay2324, 2020.

[133] MP Siegal, AL Lima-Sharma, PA Sharma, and C Rochford. Correlating thermoelectric properties with microstructure in $Bi_{0.8}Sb_{0.2}$ thin films. *Applied Physics Letters*, 110(14):141905, 2017.

[134] Shunhao Xiao, Dahai Wei, and Xiaofeng Jin. Bi(111) thin film with insulating interior but metallic surfaces. *Physical Review Letters*, 109(16):1–5, 2012.

[135] Tuo Fan, Mustafa Tobah, Takanori Shirokura, Nguyen Huynh Duy Khang, Nguyen Huynh Duy Khang, Pham Nam Hai, Pham Nam Hai, and Pham Nam Hai. Crystal growth and characterization of topological insulator BiSb thin films by sputtering deposition on sapphire substrates. *Japanese Journal of Applied Physics*, 59(6), 2020.

[136] K Ueda, Y Hadate, K Suzuki, and H Asano. Fabrication of high-quality epitaxial $bi_{1-x}sb_x$ films by two-step growth using molecular beam epitaxy. *Thin Solid Films*, 713:138361, 2020.

[137] Giri Joshi. *Study of thermoelectric properties of nanostructured p-type Silicon-Germanium, Bismuth-Tellurium, Bismuth-Antimony, and halfheusler bulk materials*. PhD thesis, Boston College, 2010.

[138] Jun Mao, Zihang Liu, and Zhifeng Ren. Size effect in thermoelectric materials. *npj Quantum Materials*, 1(1):1–9, 2016.

[139] Shunhao Xiao, Dahai Wei, and Xiaofeng Jin. Bi (111) thin film with insulating interior but metallic surfaces. *Physical review letters*, 109(16):166805, 2012.

[140] HO Yadav. Relation between the thermal activation energy of conduction and the first excited singlet state energy—a case of photo-conducting organic materials. *Thin solid films*, 477(1-2):222–226, 2005.

[141] Anubhav Jain, Shyue Ping Ong, Geoffroy Hautier, Wei Chen, William Davidson Richards, Stephen Dacek, Shreyas Cholia, Dan Gunter, David Skinner, Gerbrand Ceder, and Kristin A. Persson. Commentary: The materials project: A materials genome approach to accelerating materials innovation. *APL Materials*, 1(1):011002, 2013. [Data retrieved from the Materials Project for $Bi_3Sb$ (mp-1227319) from database version v2022.10.28.].

[142] B Lenoir, M Cassart, J-P Michenaud, H Scherrer, and S Scherrer. Transport properties of Bi-rich Bi-Sb alloys. *Journal of Physics and Chemistry of Solids*, 57 (1):89–99, 1996.

[143] Sarah E Muschinske. Transport behavior and weak adhesion of quantum confined epitaxial Bi and $Bi_{1-x}Sb_x$ films. Master's thesis, The University of Texas at Austin, 2018. [Section 3.3].

[144] Jeffrey CY Teo, Liang Fu, and CL Kane. Surface states and topological invariants in three-dimensional topological insulators: Application to $Bi_{1-x}Sb_x$. *Physical Review B*, 78(4):045426, 2008.

[145] Sunglae Cho, Antonio DiVenere, Yunki Kim, George K Wong, John B Ketterson, Jerry R Meyer, and Craig A Hoffman. Structural and thermoelectric properties of MBE-grown doped and undoped BiSb alloy thin films. In *Seventeenth International Conference on Thermoelectrics. Proceedings ICT98 (Cat. No. 98TH8365)*, pages 284–287. IEEE, 1998.

[146] F Völklein and E Kessler. Thermal Conductivity and Thermoelectric Figure of Merit of $Bi_{1-x}Sb_x$ Films With $0< x \leqq 0.3$. *physica status solidi (b)*, 143(1):121–130, 1987.

[147] Sheng Gao, John Gaskins, Xixiao Hu, Kathleen Tomko, Patrick Hopkins, and S Joseph Poon. enhanced figure of merit in bismuth-antimony fine-grained alloys at cryogenic temperatures. *Scientific reports*, 9(1):1–10, 2019.

[148] G Jeffrey Snyder, Mogens Christensen, Eiji Nishibori, Thierry Caillat, and Bo Brummerstedt Iversen. Disordered zinc in $Zn_4Sb_3$ with phonon-glass and electron-crystal thermoelectric properties. *Nature materials*, 3(7):458–463, 2004.

[149] Xin Song and Terje G Finstad. Review of research on the thermoelectric material ZnSb. *Thermoelectrics for Power Generation: A Look at Trends in the Technology*, 2016.

[150] Th Caillat, J-P Fleurial, and A Borshchevsky. Preparation and thermoelectric properties of semiconducting $Zn_4Sb_3$. *Journal of Physics and Chemistry of Solids*, 58(7):1119–1125, 1997.

[151] JH Ahn, MW Oh, BS Kim, SD Park, BK Min, HW Lee, and YJ Shim. Thermoelectric properties of $Zn_4Sb_3$ prepared by hot pressing. *Materials Research Bulletin*, 46(9):1490–1495, 2011.

[152] X Song, K Valset, JS Graff, A Thøgersen, AE Gunnæs, S Luxsacumar, OM Løvvik, GJ Snyder, and TG Finstad. Nanostructuring of undoped ZnSb by cryo-milling. *Journal of Electronic Materials*, 44(8):2578–2584, 2015.

[153] Chun-Wan Timothy Lo, Volodymyr Svitlyk, Dmitry Chernyshov, and Yurij Mozharivskyj. The updated Zn–Sb phase diagram. how to make pure $Zn_{13}Sb_{10}$ ("$Zn_4Sb_3$"). *Dalton Transactions*, 47(33):11512–11520, 2018.

[154] Hyung Cheoul Shim, Chang-Su Woo, and Seungwoo Han. Thermal cycling behavior of zinc antimonide thin films for high temperature thermoelectric power generation applications. *ACS Applied Materials & Interfaces*, 7(32):17866–17873, 2015.

[155] Flexible Electronics Market By Components (Display, Battery, Sensors, Memory), By Application (Consumer Electronics, Automotive, Healthcare, Industrial) And Segment Forecast To 2024. `https://www.grandviewresearch.com/industry-analysis/flexible-electronics-market#`. [Online; accessed 23/06/2022].

[156] Ping Fan, Wei-fang Fan, Zhuang-hao Zheng, Yin Zhang, Jing-ting Luo, Guang-xing Liang, and Dong-ping Zhang. Thermoelectric properties of zinc antimonide thin film deposited on flexible polyimide substrate by RF magnetron sputtering. *Journal of Materials Science: Materials in Electronics*, 25(11):5060–5065, 2014.

[157] Zhuang-hao Zheng, Fu Li, Jing-ting Luo, Guang-xing Liang, Hong-li Ma, Xiang-hua Zhang, and Ping Fan. Enhancement of power factor in zinc antimonide thermoelectric thin film doped with titanium. *Materials Letters*, 209:455–458, 2017.

[158] Zhuang-hao Zheng, Ping Fan, Jing-ting Luo, and Guang-xing Liang. Enhanced thermoelectric properties of in-doped ZnSb thin film with surface nanocrystallization. *Journal of Electronic Materials*, 46(2):1319–1323, 2017.

[159] Heon Bok Lee, Ju Hyung We, Hyun Jeong Yang, Kukjoo Kim, Kyung Cheol Choi, and Byung Jin Cho. Thermoelectric properties of screen-printed ZnSb film. *Thin Solid Films*, 519(16):5441–5443, 2011.

[160] Zhuang-hao Zheng, Ping Fan, Jing-ting Luo, and Guang-xing Liang. Hybridization of electronic band structure and enhancement of thermoelectric properties of ZnSb thin film by In doping. *Journal of Physics and Chemistry of Solids*, 103:82–86, 2017.

[161] Ahmad Ostovari Moghaddam, Ali Shokuhfar, Yu Zhang, Ting Zhang, Doris Cadavid, Jordi Arbiol, and Andreu Cabot. Ge-doped ZnSb/$\beta$-$Zn_4Sb_3$ nanocomposites with high thermoelectric performance. *Advanced Materials Interfaces*, 6(18): 1900467, 2019.

[162] Guoxiang Wang, Haizhou Shi, Andriy Lotnyk, Daotian Shi, and Rongping Wang. Conversion of p–n conduction type by spinodal decomposition in Zn-Sb-Bi phase-change alloys. *NPG asia Materials*, 12(1):1–13, 2020.

[163] Xin Song, Matthias Schrade, Nahum Masó, and Terje G Finstad. Zn vacancy formation, Zn evaporation and decomposition of ZnSb at elevated temperatures: Influence on the microstructure and the electrical properties. *Journal of Alloys and Compounds*, 710:762–770, 2017.

[164] LT Zhang, M Tsutsui, K Ito, and M Yamaguchi. Effects of ZnSb and Zn inclusions on the thermoelectric properties of $\beta$-$Zn_4Sb_3$. *Journal of Alloys and Compounds*, 358(1-2):252–256, 2003.

[165] KW Jang, Il Ho Kim, Jung Il Lee, and Good Sun Choi. Thermoelectric properties of $Zn_{4-x}Sb_3$ with x= 0∼0.5. In *Solid State Phenomena*, volume 124, pages 1019–1022. Trans Tech Publ, 2007.

[166] Xin He, Yuhao Fu, David J Singh, and Lijun Zhang. Stability, electronic structures and thermoelectric properties of binary Zn–Sb materials. *Journal of Materials Chemistry C*, 4(47):11305–11312, 2016.

[167] M Tapiero, S Tarabichi, JG Gies, C Noguet, JP Zielinger, M Joucla, JL Loison, M Robino, and J Herion. Preparation and characterization of $Zn_4Sb_3$. *Solar Energy Materials*, 12(4):257–274, 1985.

[168] Mauricio Schoijet. Possibilities of new materials for solar photovoltaic cells. *Solar Energy Materials*, 1(1-2):43–57, 1979.

[169] Ya A Ugai, EM Averbakh, and VV Lavrov. Some electrical properties of the intermetallic compound beta-zn4sb3. *Soviet Physics-Solid State*, 4(11):2393–2395, 1963. [Original paper was not found online, but the refrence was cited for the information].

[170] Hitoshi Nagata, Atsumi Yamaguchi, and Akira Kawai. Characterization of thin-film interference effect due to surface roughness. *Japanese Journal of Applied Physics*, 34(7R):3754, jul 1995.

[171] Lin Jianhui, Yan Bing, Wu Xiaoming, Ren Tianling, and Liu Litian. Stretchable interconnections for flexible electronic systems. In *2009 Annual International Conference of the IEEE Engineering in Medicine and Biology Society*, pages 4124–4127. IEEE, 2009.

[172] Ding-Bang Xiong, Norihiko L Okamoto, and Haruyuki Inui. Enhanced thermoelectric figure of merit in p-type Ag-doped ZnSb nanostructured with $Ag_3Sb$. *Scripta Materialia*, 69(5):397–400, 2013.

[173] Ye Sun, Mogens Christensen, Simon Johnsen, Ngo V Nong, Yi Ma, Michael Sillassen, Eryun Zhang, Anders EC Palmqvist, Jørgen Bøttiger, and Bo B Iversen. Low-cost high-performance zinc antimonide thin films for thermoelectric applications. *Advanced Materials*, 24(13):1693–1696, 2012.

[174] Shih-Chieh Hsu, Jhen-Yong Hong, Cheng-Lung Chen, Sheng-Chi Chen, Jia-Han Zhen, Wen-Pin Hsieh, Yang-Yuan Chen, and Tung-Han Chuang. The structures and thermoelectric properties of Zn-Sb alloy films fabricated by electron beam evaporation through an ion beam assisted deposition. *Applied Surface Science*, 540:148264, 2021.

[175] Pablo Ares, Sahar Pakdel, Irene Palacio, Wendel S Paz, Maedeh Rassekh, David Rodríguez-San Miguel, Lucía Aballe, Michael Foerster, Nerea Ruiz del Árbol, José Ángel Martín-Gago, et al. Few-layer antimonene electrical properties. *Applied Materials Today*, 24:101132, 2021.

[176] EA Anyebe, Mohana K Rajpalke, Tim D Veal, CJ Jin, ZM Wang, and QD Zhuang. Surfactant effect of antimony addition to the morphology of self-catalyzed $InAs_{1-x}Sb_x$ nanowires. *Nano Research*, 8(4):1309–1319, 2015.

[177] Elena S Makarova, Anastasiia S Tukmakova, Anna V Novotelnova, Vladimir A Komarov, Vasilisa A Gerega, Natallya S Kablukova, and Mikhail K Khodzitsky. Effect of antimony buffer layer on the electric and magnetic properties of 200 and 600 nm thick bismuth films on mica substrate. *Materials*, 13(9):2010, 2020.

[178] H Toyota, A Mikami, T Endoh, Y Jinbo, and N Uchitomi. Effect of Sb template layer on GaSb thin films grown on Si (111) substrate by molecular beam epitaxy. *physica status solidi c*, 8(2):269–271, 2011.

[179] H Toyota, A Okabe, T Endoh, Y Jinbo, and N Uchitomi. Study of Sb template for heteroepitaxial growth of GaSb thin film on Si (111) substrate. *Journal of crystal growth*, 378:129–133, 2013.

[180] Philip J Mousley, Christopher W Burrows, Chris Nicklin, and Gavin R Bell. Structure of strained low-dimensional Sb by in situ surface x-ray diffraction. *physica status solidi (b)*, 259(4):2100432, 2022.

[181] Yuzhuo Luo, Yunqing Tang, Tsai-Fu Chung, Cheng-Ling Tai, Chih-Yuan Chen, Jer-Ren Yang, and DY Li. Electron work function: an indicative parameter towards a novel material design methodology. *Scientific reports*, 11(1):11565, 2021.

[182] ZR Liu and DY Li. The electronic origin of strengthening and ductilizing magnesium by solid solutes. *Acta Materialia*, 89:225–233, 2015.

[183] Ang-Sheng Chou, Tong Wu, Chao-Ching Cheng, Shun-Siang Zhan, I-Chih Ni, Shih-Yun Wang, Yu-Chen Chang, San-Lin Liew, Edward Chen, Wen-Hao Chang, et al. Antimony semimetal contact with enhanced thermal stability for high performance 2d electronics. In *2021 IEEE International Electron Devices Meeting (IEDM)*, pages 7–2. IEEE, 2021.

[184] Jesús Barrio, Carlos Gibaja, Miguel García-Tecedor, Liel Abisdris, Iñigo Torres, Neeta Karjule, Sixto Giménez, Menny Shalom, and Félix Zamora. Electrophoretic deposition of antimonene for photoelectrochemical applications. *Applied Materials Today*, 20:100714, 2020.

[185] Andrea M Lucero Manzano, Esteban D Cantero, Esteban A Sánchez, and Oscar Grizzi. Sb adsorption on $TiO_2$ (1 0 0): Growth, morphology, work function and thermal dependence. *Applied Surface Science*, 602:154326, 2022.

[186] ENK Glover, SG Ellington, G Sankar, and RG Palgrave. The nature and effects of rhodium and antimony dopants on the electronic structure of $TiO_2$: towards design of Z-scheme photocatalysts. *Journal of Materials Chemistry A*, 4(18):6946–6954, 2016.

[187] Satoshi Kojima, Yoshiaki Tanaka Yoshiaki Tanaka, and Ryozi Suganuma Ryozi Suganuma. Single-crystal growth of $Cu_2Sb$ in evaporated Sb fims with Cu specimen grids. *Japanese journal of applied physics*, 30(10R):2558, 1991.

[188] Xinjian Yi, Hongchen Wang, Sihai Chen, Jianjun Lai, Miao He, Shuangfao Wang, and George K Wong. Quantum size effect in antimony thin films and its application. *Infrared physics & technology*, 46(3):263–266, 2005.

[189] Lee R. Windmiller. de haas-van alphen effect and fermi surface in antimony. *Phys. Rev.*, 149:472–484, Sep 1966.

[190] EV Demidov. On the problem of calculating the concentration and mobility of charge carriers in thin bismuth films and a bismuth–antimony solid solution. *Journal of Surface Investigation: X-ray, Synchrotron and Neutron Techniques*, 16(5): 712–719, 2022.

[191] Liang Fu, Charles L Kane, and Eugene J Mele. Topological insulators in three dimensions. *Physical review letters*, 98(10):106803, 2007.

[192] LM Falicov and PJ Lin. Band structure and fermi surface of antimony: pseudopotential approach. *Physical Review*, 141(2):562, 1966.

[193] Antimony (Sb) band structure, energy gap: Datasheet from Landolt-Bornstein - Group III Condensed Matter · Volume 41C: "Non-Tetrahedrally Bonded Elements and Binary Compounds I. Copyright 1998 Springer-Verlag Berlin Heidelberg, Part of SpringerMaterials, accessed 2022-09-28.

[194] JH Xu, EG Wang, CS Ting, and WP Su. Tight-binding theory of the electronic structures for rhombohedral semimetals. *Physical Review B*, 48(23):17271, 1993.

[195] L Ley, RA Pollak, SP Kowalczyk, R McFeely, and DA Shirley. Evidence for covalent bonding in crystalline and amorphous As, Sb, and Bi from valence-band photoelectron spectra. *Physical Review B*, 8(2):641, 1973.

[196] Sergio Trasatti. Work function, electronegativity, and electrochemical behaviour of metals: III. Electrolytic hydrogen evolution in acid solutions. *Journal of Electroanalytical Chemistry and Interfacial Electrochemistry*, 39(1):163–184, 1972.

[197] Sergio Trasatti. Work function, electronegativity, and electrochemical behaviour of metals: II. Potentials of zero charge and "electrochemical" work functions. *Journal of Electroanalytical Chemistry and Interfacial Electrochemistry*, 33(2):351–378, 1971.

[198] S Trasatti. Work function, electronegativity, and electrochemical behaviour of metals. pt. 1. experimental values of work function. *CHIM IND*, 53(6):559–564, 1971. [Original paper was not found online, but the reference was cited for the information].

[199] Herbert B Michaelson. Work functions of the elements. *Journal of Applied Physics*, 21(6):536–540, 1950.

[200] Herbert B Michaelson. The work function of the elements and its periodicity. *Journal of applied physics*, 48(11):4729–4733, 1977.

[201] Viktor Middel. Lichtelektrische messungen an metallischem antimon. *Zeitschrift für Physik*, 105(5-6):358–377, 1937.

[202] Roger Parsons. *Handbook of electrochemical constants*. Butterworths Scientific Publications, 1959.

[203] DA Gorodetsky, Yu P Mel'nik, DP Proskurin, and VA Usenko. Structure and electronic properties of antimony films on the Mo (110) surface. *Physics of the Solid State*, 46:1940–1948, 2004.

[204] DA GORODETSKY and AA YASKO. Structure and work function of Sb films on a W–100– surface. *Sov. phys. solid state*, 13(11):2928–2929, 1972.

[205] AN Frumkin. Zero charge potentials of electrodes. *Svensk Kemisk Tidskrift*, 77 (6-7):300, 1965. [Original paper was not found online, but the reference was cited for the information].

[206] N. Liu, T. Zhu, M.G. Rosul, J. Peters, J.E. Bowers, and M. Zebarjadi. Thermoelectric properties of holey silicon at elevated temperatures. *Materials Today Physics*, 14:100224, 2020.

[207] Katrina A Morgan, Tian Tang, Ioannis Zeimpekis, Andrea Ravagli, Chris Craig, Jin Yao, Zhuo Feng, Dmitry Yarmolich, Clara Barker, Hazel Assender, et al. High-throughput physical vapour deposition flexible thermoelectric generators. *Scientific reports*, 9(1):4393, 2019.

[208] Doris Danninger, Roland Pruckner, Laura Holzinger, Robert Koeppe, and Martin Kaltenbrunner. Myceliotronics: Fungal mycelium skin for sustainable electronics. *Science Advances*, 8(45):eadd7118, 2022.

[209] Huajie Chen, Randall M Feenstra, J Northrup, Jörg Neugebauer, and David W Greve. Indium incorporation and surface segregation during InGaN growth by molecular beam epitaxy: experiment and theory. *MRS Internet Journal of Nitride Semiconductor Research*, 6:1–8, 2001.

[210] Ishan Choudhary and Deepak. Investigation of time-dependent stability and surface defects in sol-gel derived IGZO and IZO thin films. *Journal of Sol-Gel Science and Technology*, 100:132–146, 2021.

[211] Norman Neill Greenwood and Alan Earnshaw. *Chemistry of the Elements*. Elsevier, 2012.

[212] H Okamoto. Bi-sb (bismuth-antimony). *Journal of Phase Equilibria and Diffusion*, 33:493–494, 2012.

[213] Shuang Tang and Mildred S Dresselhaus. Phase diagrams of $Bi_{1-x}$ $Sb_x$ thin films with different growth orientations. *Physical Review B*, 86(7):075436, 2012.

[214] S Malki and L El Farh. Structural and electronic properties of zinc antimonide ZnSb. *Materials Today: Proceedings*, 31:S41–S44, 2020.

[215] AN Qiu, LT Zhang, and JS Wu. Crystal structure, electronic structure, and thermoelectric properties of $\beta$-$Zn_4$ $Sb_3$ from first principles. *Physical Review B*, 81(3): 035203, 2010.

[216] Tianhua Zou, Wenjie Xie, Jian Feng, Xiaoying Qin, and Anke Weidenkaff. Recent developments in $\beta$-$Zn_4Sb_3$ based thermoelectric compounds. *Journal of Nanomaterials*, 2015:642909, Sep 2015.